Measuring Aortic Annulus Size using a Soft Robotic Balloon Catheter

Andrea Palombi

Supervisors: Dr. Helge A Würdemann
Dr. Gaetano Burriesci

Department of Mechanical Engineering
University College London

A thesis submitted for the degree of
Master of Philosophy

October 2022

Declaration

I confirm that the work presented in this thesis is my own. Where information has been derived from other sources, I confirm that this has been indicated in the work.

Andrea Palombi
October 2022

Abstract

Transcatheter aortic valve implantation (TAVI) is a minimally invasive surgical technique to treat aortic heart valve diseases. According to current clinical guidelines, the implanted prosthetic valve replacing the native one is selected based on pre-operative size assessment of the aortic annulus through different imaging techniques. That very often leads to sub-optimal device selection resulting in major complications, such as aortic regurgitation and atrioventricular blocks.

In this work, we propose a new, intra-operative approach to determine the diameter of the aortic annulus exploiting intra-balloon pressure and volume (p-v) data, acquired from a robotised valvuloplasty balloon catheter. This strategy, combined with current imaging-based sizing methods, would allow to obtain more accurate measurements and check whether the implantation region has changed as a consequence of the valvuloplasty procedure. That would improve TAVI device selection, potentially reducing the occurrence of the aforementioned complications.

Two robotic inflation devices, capable of collecting real-time intra-balloon p-v data, were designed and interfaced with a commercially available valvuloplasty balloon catheter. A sizing algorithm that can precisely estimate the annular diameter from acquired p-v data was also implemented. The algorithm relies on a mathematical model of the balloon free inflation and an iterative method based on linear regression. Two different mathematical models of the balloon free inflation, one analytical and one numerical, were developed and compared in terms of sizing accuracy.

In vitro tests were performed on idealised aortic phantoms. Experimental results show that pressure-volume data can be used to determine annular diameters bigger than the unstretched diameter of the balloon catheter. This conclusion applies to both rigid and compliant phantoms characterised by a rigidity greater than 100 kPa/%. For these cases, the proposed approach exhibited good precision (maximum average error $\mathbf{1.972}\%$) and good repeatability (maximum standard deviation $\pm\mathbf{0.263}$ mm).

Table of contents

List of figures

List of tables

Nomenclature

Acronyms / Abbreviations

AR	Aortic Regurgitation
AS	Aortic Stenosis
AVR	Open-heart Surgical Aortic Valve Replacement
BAV	Balloon Aortic Valvuloplasty
CMR	Cardiovascular Magnetic Resonance
CVD	Cardiovascular Disease
ECG	Electrocardiogram
MDCT	Multidetector Computer Tomography
VHD	Valvular Heart Disease
MRI	Magnetic Resonance Imaging
PE	Polyethylene
PET	Polyethylene Terephthalate
PU	Polyurethane
PVC	Polyvinyl Chloride
TAVI	Transcatheter Aortic Valve Implantation
TEE	Transesophageal Echocardiography
TTE	Transthoracic Echocardiography

Chapter 1

Introduction

1.1 Background

Cardiovascular diseases (CVDs) are the leading cause of death in the world, accounting for approximately 31% of global mortality [1, 2]. The majority of CVD burden can be attributed to specific health conditions, such as hypertension, diabetes mellitus and dyslipidaemia, and to behavioural risk factors, like tobacco smoking, alcohol abuse, lack of physical activity and unhealthy dietary habits [1–3]. Valvular heart diseases (VHDs) are a subgroup of CVDs. They are associated with the malfunctioning of one or more of the four valves that regulate the blood flow through the heart and their etiologies can be congenital, rheumatic or degenerative. VHDs account for 10% to 20% of all cardiac surgical procedures in the US [4].

Since the beginning of the seventies, reducing the number of deaths from major vascular diseases, like ischaemic heart disease and stroke, has been one of the primary objectives of public health all over the world. On the other hand, it wasn't until the beginning of 2000s that the substantial burden of VHDs was quantitatively investigated [5]. At the end of the last century, rheumatic fever and syphilis, which were very common causes of VHDs 60-70 years ago, had nearly disappeared in industrialised countries. Residual valvular diseases were mainly degenerative and they were not considered a major public health issue [6, 7]. That has radically changed over the past decade and VHDs are now occupying a central role in cardiovascular medicine. An ageing population increasingly more affected by degenerative diseases, as well as revolutionary innovations in the fields of imaging technology and transcatheter minimally invasive surgery, have catalysed the attention of researchers, clinicians, engineers and investors, transforming the landscape of clinical management [6].

The research work presented in this thesis fits into the broader context of transcatheter aortic valve implantation (TAVI), a minimally invasive surgical technique used to treat aortic heart valve diseases. Before discussing the aim and objectives in detail, key aspects of the human

cardiovascular system, with a specific focus on the aortic valve, and the procedural steps of TAVI will be introduced.

1.1.1 The Cardiovascular System and The Heart

The cardiovascular system is a closed one-way circuit responsible for rapidly transporting materials throughout the human body. It can be divided intro three main components: the blood, the blood vessels and the heart. The blood is a fluid connective tissue that can carry oxygen and other nutrients, as well as metabolic wastes produced by body cells. Blood vessels are the conduits through which blood is delivered to the tissues. The five main types of vessels are arteries, arterioles, capillaries, venules and veins [8]. The mechanical energy required to pump blood to even the smallest vessels of the human extremities is provided by the contraction of the heart, a hollow muscular organ slightly larger than a closed fist [9].

The heart is located in the space between the lungs inside the thoracic cavity and it lies obliquely across the midline of the chest. As shown in Fig.1.1, its walls are characterised by three layers of tissue, called pericardium, myocardium and endocardium [10]. The pericardium is a double-walled membrane that surrounds the heart. The outermost surface of the pericardial sac is made of tough fibrous tissue. Its main function is to anchor the

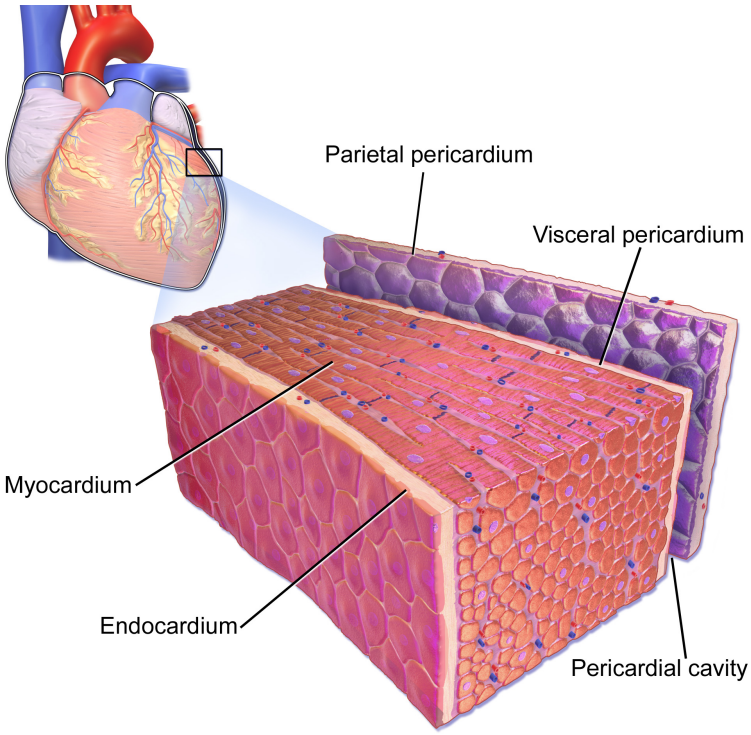

Fig. 1.1 Pericardium, myocardium and endocardium, the layers of the heart walls [11].

heart in the mediastinal space and prevent overdistention during contractions. The serous pericardium is directly below the fibrous pericardium and it can be divided into parietal and visceral pericardium. The parietal pericardium is fused with the fibrous pericardium, while the visceral pericardium adheres to the myocardium. The two layers of the serous pericardium are separated by the pericardial fluid that helps to reduce friction as the heart beats [12]. The myocardium is the middle muscular layer of the heart and it is responsible for its pumping action. Unlike skeletal muscles, the cardiac muscle is not under conscious control [10]. The endocardium is the innermost layer of the heart walls and it lines the heart chambers and valves [10].

The structure of the heart is characterised by four chambers and four valves, which guarantee the unidirectionality of the blood flow throughout the cardiovascular system (Fig.1.2):

- **Right atrium and tricuspid valve:** the right atrium receives low pressure (about 0 mmHg) deoxygenated blood from the two venae cavae. Once the atrium is filled, it contracts pushing the blood down to the right ventricle through the tricuspid valve [13].

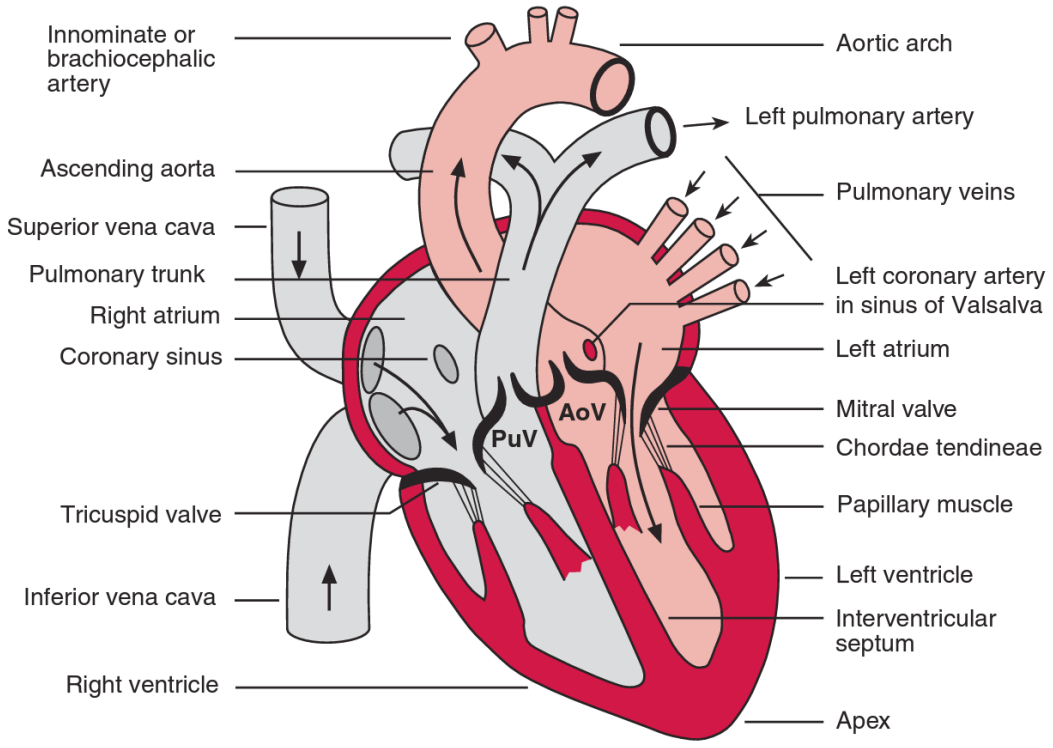

Fig. 1.2 Structure of the heart. The color grey refers to deoxygenated blood, while pink indicates oxygenated blood(AoV Aortic Valve; PuV Pulmonary Valve) [13].

- **Right ventricle and pulmonary valve:** when the right ventricle contracts, blood at a pressure ranging from 20 to 30 mmHg crosses the pulmonary valve, entering the pulmonary artery. The tricuspid valve prevents blood from flowing back into the right atrium. The pulmonary artery leads blood to the lungs for oxygenation [13].

- **Left atrium and mitral valve:** the left atrium is where oxygenated blood from the pulmonary veins reenters the heart at a pressure of approximately 10 mmHg. The contraction of the left atrium pumps the blood to the left ventricle through the mitral valve [13].

- **Left ventricle and aortic valve:** the walls of the left ventricle are roughly three times thicker than the ones of the right ventricle. That is because oxygenated blood in this chamber needs a pressure of 100 to 140 mmHg to flow across the aortic valve, enter the aorta and reach all parts of the body [13]. When the contraction of the left ventricle begins, the raising blood pressure forces the mitral valve to close preventing regurgitation into the left atrium.

For the sake of clarity, the four cardiac chambers were presented as if they worked in a sequential way. However, during the cardiac cycle the two halves of the heart operate like two synchronous pumps. As depicted in Fig.1.3, the cycle starts when all chambers are relaxed (diastole). The mitral and the tricuspid valves are open. Therefore, blood in the atria flows unimpeded into the ventricles. At the beginning of atrial contraction (systole), 70-80 percent of the ventricular volume is already filled with blood. Atrial contraction, which lasts approximately 100 ms, allows to complete the filling [13, 14]. After atrial systole, ventricular systole begins. First the muscles in the ventricular walls contract and blood pressure rapidly increases. When the pressure in the ventricles is high enough to push open the pulmonary and the aortic valves, blood is pumped from the heart into the pulmonary artery and the aorta. Ventricular systole lasts in total 270 ms and it is followed by ventricular relaxation [14]. During ventricular diastole the pressure within the ventricles decreases causing the pulmonary and the aortic valves to close. Pressure continues to drop even further, as the ventricles elastically recoil from their deformed shape. Consequently, the two atrioventricular valves open and the cycle starts over. With a duration of about 430 ms, ventricular diastole is the longest phase of the cardiac cycle, which lasts overall 0.8-0.9 s [13, 14].

In the next subsection, the anatomy of the aortic valve and its most common diseases will be presented in details.

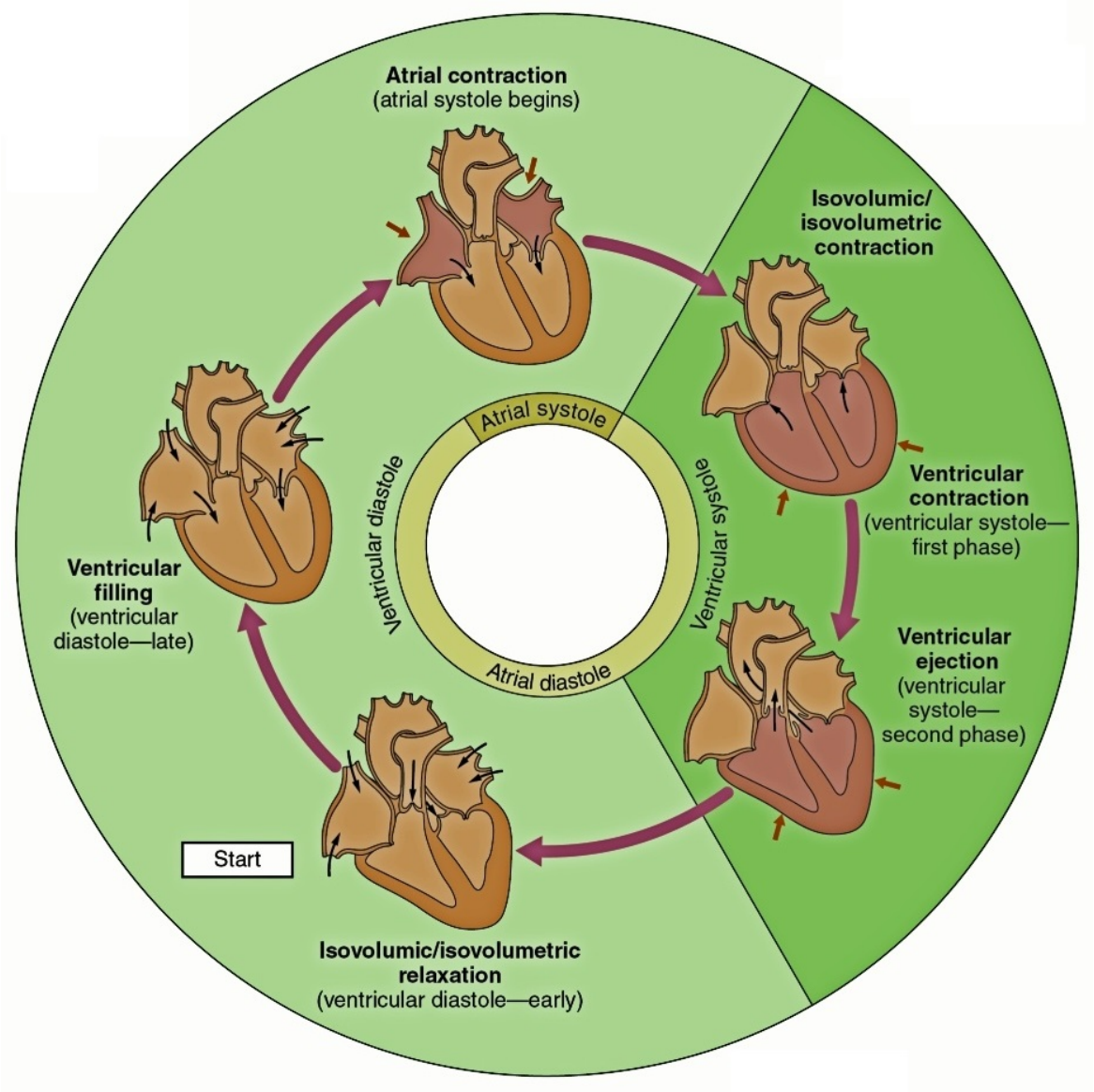

Fig. 1.3 Diagram representing the various phases of the cardiac cycle [14].

1.1.2 The Aortic Valve: Anatomy and Diseases

As described in the previous subsection, the aortic valve opens to allow blood to flow into the aorta and it closes to prevent regurgitation into the left ventricle. This cycle occurs approximately 103000 times each day which means roughly 3.7 billion times in the valve average lifespan [15].

The aortic valve is part of a complex structure, the aortic root, that altogether plays a key role in its proper functioning [16]. The aortic root acts as a bridge between the left ventricular outflow tract and the ascending aorta and it consists of three leaflets, the interleaflet trigones,

the sinuses of Valsalva, the sinotubular junction and the annulus [17] (Fig. 1.4).
Each leaflet is attached to the aortic root through a fibrous structure, shaped like a half-moon. The attachments of adjacent leaflets join at the level of the sinotubular junction, forming the three commissures. When the aortic valve is closed, a portion of each leaflet apposes to the other two leaflets. This coaptation area is called lunula and it is located on the ventricular surface of the leaflet. The cusps of the lunulae are characterised by the presence of a small bulge, called nodule of Arantius. The central region of the leaflet separates the ventricle from the aorta during valve closure and it is capable of withstanding the load of aortic pressure [15–17]. The triangular regions located underneath the commissures are known as the interleaflet trigones. Although they are made of aortic fibro-elastic cells, they belong to the ventricular portion of the aortic root. During surgical valve procedures it is crucial to avoid injuring this area, as damages may cause temporary or permanent conduction abnormalities, potentially leading to a permanent pacemaker implantation [17, 18].
The three bulges surrounding the leaflets are the sinuses of Valsalva. Two of them give rise to the coronary arteries, which supply blood to the heart muscle. The other one has an exclusively arterial wall. The specific function of the sinuses is still unclear. Nevertheless, there is evidence that their presence is critical for the optimisation of the aortic hemodynamics. By reducing the pressure drop across the aortic valve during ventricular systole, they help minimising energy losses [19]. Furthermore, the vortices created in the sinuses by the blood flow, lead to lower stresses on the leaflets and promote the diastolic coronary perfusion

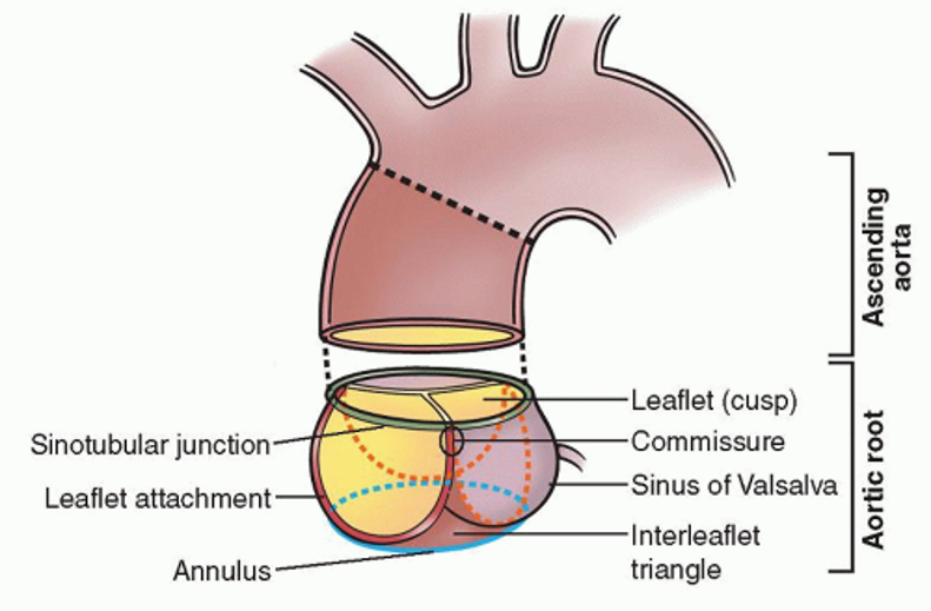

Fig. 1.4 Schematic representation of the aortic root and its components [17].

[17, 20]. The sinuses of Valsalva are separated from the ascending aorta by the sinotubular junction, a tubular structure that comprises the leaflet commissures. In healthy aortic roots the diameter of the sinotubular junction is roughly 75% smaller than the maximal sinus diameter [20].

An area of great interest for aortic valve replacement procedures is the annulus. Although the term implies a ring-shaped region or structure, in the aortic root there are no distinct histological or anatomical entities that fit the description. Due to that, there are still controversies about the exact definition of the aortic annulus [16, 17, 20]. In this work, the definition usually adopted by cardiologists and radiologists, according to which the annulus corresponds to the virtual basal ring, will be followed. The virtual basal ring is the imaginary elliptical line that joins the nadirs of the semilunar leaflet attachments [20]. Its relevance for valve replacement procedures stems from the fact that the annulus corresponds to the smallest cross-sectional area in the aortic root [17]. Therefore it not only determines the size of the prosthesis to be implanted but also its positioning [17, 20].

The two most common disorders associated with the aortic valve are aortic regurgitation (AR) and aortic stenosis (AS) [21, 22]. AR is characterised by the presence of blood backflow into the left ventricle during diastole, due to an incomplete closure of the aortic valve. Although it is mainly related to congenital abnormalities, such as a biscupid aortic valve, AR can also be caused by degenerative changes of the valve leaflets and diseases, like endocarditis and rheumatic fever. Severe forms of this pathology can lead to cardiac failure, as the heart has to do more work to compensate for the blood leakage. Nevertheless, AR is much less prevalent than AS and represents a lesser public health concern [21].
AS is the most common and serious heart valve disease. The condition is characterised by a narrowing of the aortic valve opening (Fig.1.5). The restriction of blood flow from the left ventricle to the aorta, causes a buildup of pressure inside the ventricular chamber,

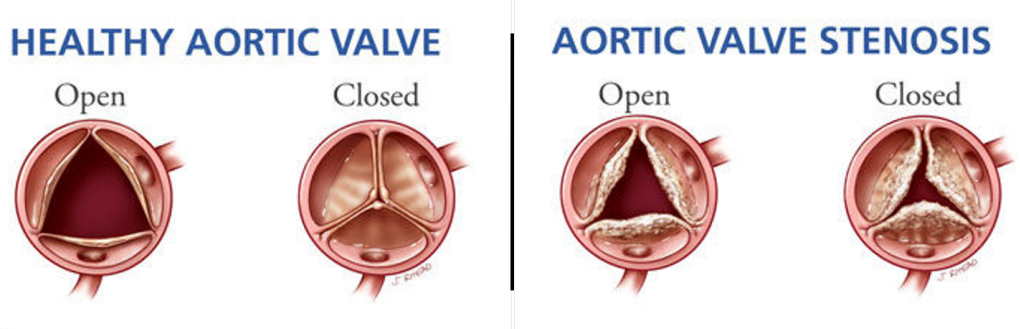

Fig. 1.5 Normal and stenotic aortic valve morphologies [23]

potentially leading to heart failure. Most commonly, AS is induced by age-related progressive calcification of the valvular leaflets, however, it can also be caused by a congenitally bicuspid valve or post-inflammatory valvular disease [21, 22]. It affects 2% of people who are over 65 years of age [24] and, if untreated, it is associated with a 50% rate of death within two years after the appearance of symptoms [25].
According to the guidelines recommended by both the American College of Cardiology/American Heart Association [26] and the European Association of Echocardiography/American Society of Echocardiography [27], the severity of AS can be graded based on parameters that can be measured non-invasively through echocardiography (Tab.1.1). Patients with mild and moderate AS are normally treated with standard evidence-based heart failure therapies, such as angiotensin-converting enzyme inhibitors, beta-blockers, and aldosterone receptor antagonists [24]. On the other hand, surgical aortic valve replacement (AVR) and transcatheter aortic valve implantation (TAVI) are the only effective treatments for severe and very severe AS.

GRADE	**Mild**	**Moderate**	**Severe**	**Very Severe**
Peak Aortic Jet Velocity $[m/s]$	$2.0-2.9$	$3.0-3.9$	$\geqslant 4.0$	$\geqslant 5.0$
Mean Pressure Gradient $[mmHg]$	<20	$20-39$	$\geqslant 40$	$\geqslant 60$
Aortic Valve Area $[cm^2]$	>1.5	$1.0-1.5$	$\leqslant 1.0$	–
Indexed Aortic Valve Area $[cm^2/m^2]$	>0.85	$0.60-0.85$	<0.60	–

Table 1.1 Criteria for grading the severity of aortic stenosis [24].

1.1.3 Transcatheter Aortic Valve Implantation (TAVI)

Open-heart surgical aortic valve replacement (AVR) is the traditional procedure used to treat AS. However, at least 30% of the patients with severe AS cannot undergo surgery due to advanced age, left ventricular dysfunction or multiple coexisting health conditions [24, 25]. Hence, transcatheter aortic valve implantation (TAVI) was introduced in 2002 as a minimally invasive alternative to AVR [28].
The main steps of TAVI can be summarised as follows [29–31]:

1. **Pre-operative Assessments:** according to current guidelines, patients need to be assessed and evaluated by a multidisciplinary heart team. Multimodality imaging is

performed to check the anatomic suitability for the procedure, determine the optimal access route and select the size of the prosthetic valve to be implanted. This step is crucial in order to guarantee positive procedural outcomes.

2. **Access:** the femoral artery is the preferred access route for TAVI. Nonetheless, the transfemoral access is precluded in 25-30% of patients, due to femoro-iliac tortuosity, peripheral artery disease or previously implanted arterial grafts [32]. When that happens, the main alternative access sites reported in the literature are transapical, transaortic, transcarotid, transcaval and transaxyllarian.
   Transfemoral TAVI is performed under fluoroscopic guidance. A pigtail catheter is first advanced inside the femoral artery and the ascending aorta, until the non-coronary cusp of the native valve is reached. A contrast agent is then injected to identify the optimal annular viewing plane under fluoroscopy. Subsequently, the primary access sheath is used to insert an Amplatz left diagnostic catheter over a J-tip guidewire. The wire is then exchanged for a straight-tip guidewire for aortic valve crossing.

3. **Valve Crossing and Balloon Aortic Valvuloplasty:** after crossing the aortic valve, the Amplatz catheter is moved forward into the left ventricle. Afterwards, the guidewire is replaced with an exchange-length J-tip wire, while a pigtail catheter takes the place of the Amplatz catheter. By connecting the two pigtail catheters to pressure transducers, it is possible to measure the pressure gradient across the valve.
   At this stage balloon aortic valvuloplasty (BAV) is performed. During BAV a balloon catheter, designed to reach a specific diameter for a given pressure, is inflated to

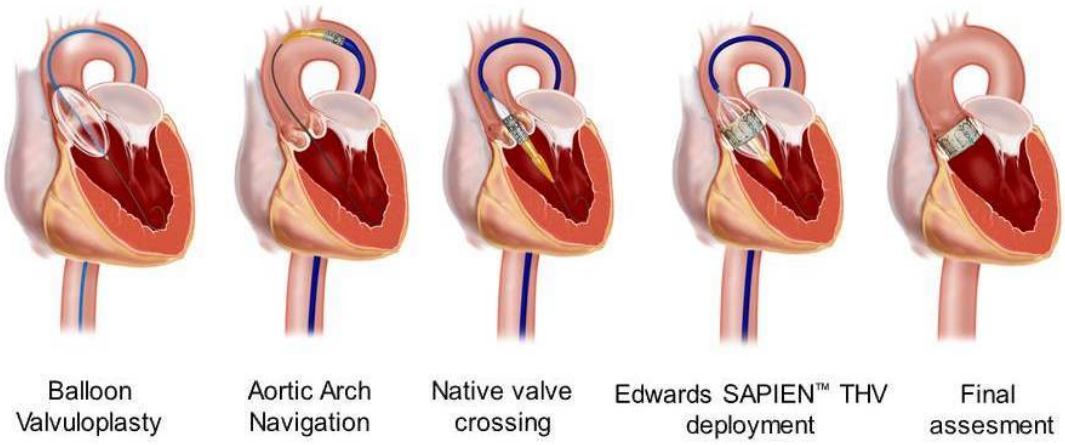

Fig. 1.6 Main procedural steps of transfemoral TAVI.

dilate the native calcified valve. The procedure is performed manually using a syringe equipped with a manometer and filled with saline solution. BAV usually results in a reduction of 40-50% of the original mean transaortic valvular gradient. The balloon size is usually chosen according to imaging-based assessment of the annular diameter. Initially the deflated balloon catheter is positioned across the annulus. The pace of the heart is then increased to 180-220 bpm through either a temporary pacing wire or a pacemaker, if the patient has one. The aim is to reduce the cardiac output in order to guarantee the stability of the balloon catheter during inflation. The balloon inflation only takes a few seconds (typically $\approx$ 3 s) and it is followed by rapid balloon deflation and discontinuation of overdrive pacing. Finally, the catheter is withdrawn, while the guidewire is kept in place [33–35].

4. **Prosthetic Valve Implantation:** the approach used for prosthetic valve implantation varies depending on the selected device. Current commercially available prostheses can be classified according to their expansion mechanism. Balloon-expandable valves, like the Edwards SAPIEN (Edwards Lifesciences, Irvine, CA, US), are usually crimped onto a delivery system, that is essentially a balloon catheter with integrated mechanisms to steer the device inside the aorta and adjust the position of the prosthesis inside the aortic annulus (Fig. 1.7). During implantation they are expanded to a diameter larger than that of the annulus. That causes the stent, which is usually made of steel, to undergo plastic deformation associated with the formation of plastic hinges. The radial forces required to anchor the valve to the annular walls can only be generated if the elastic recoil of the stent, after balloon deflation, is smaller than the one of the annular structure [36, 37].
   On the other hand, self-expandable valves, like the Medtronic CoreValve (Medtronic, Dublin, Ireland), are characterised by stents made of shape-memory alloys (Fig. 1.7). The stent of the CoreValve, for example, is made of Nitinol, a superelastic nickel–titanium alloy. Due to its shape memory ability, a Nitinol stent strives for its expanded memorised shape, which is preset trough a specific thermal treatment [36, 37]. Before deployment, self-expandable valves are cooled and compressed within a delivery catheter. A covering sheath prevents the valve from expanding during endovascular navigation. Once the implantation region is reached, the covering sheath is withdrawn, allowing the prosthesis to expand.

5. **Final Assessments and Retrieval:** once the deployment phase is completed, the delivery system is extracted and TEE is used to check the valve position, the valve shape and the motion of the leaflets. The haemodynamics is also assessed in terms

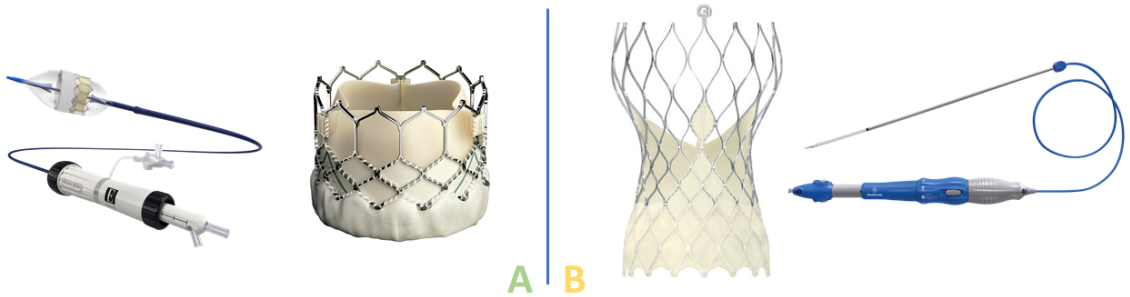

VALVE TYPE	TEE Diameter [mm]	Native Annulus Area/Perimeter	Area-derived Diameter [mm]	VALVE SIZE [mm]
Edwards SAPIEN 3	16-19	273-345 mm^2	18.6-21.0	20
	18-22	338-430 mm^2	20.7-23.4	23
	21-25	430-546 mm^2	23.4-26.4	26
	24-28	540-683 mm^2	26.2-29.5	29
Medtronic CoreValve Evolute R	17-20	56.5-62.8 mm	-	23
	20-23	62.8-72.3 mm	-	26
	23-26	72.3-81.7 mm	-	29
	26-30	81.7-94.2 mm	-	34

Fig. 1.7 a) Edwards SAPIEN 3 valve with Commander delivery system b) Medtronic CoreValve Evolute R with EnVeo R delivery system. Each valve model is associated with a specific sizing chart provided by the manufacturer.

of maximum velocity, mean pressure gradient and effective orifice area. Balloon post-dilation is performed in case the mean pressure gradient or the maximum velocity are too high.

If major complications such as AR, ventricular dysfunction and coronary artery occlusion can be excluded, the wire and the large sheath are removed. The procedure is then finalised by withdrawing the pacing wire and suturing the access point.

1.2 Clinical Motivation

The positive clinical outcomes have allowed TAVI to rapidly develop over the past fifteen years. Improved prostheses and delivery systems, as well as the increased experience of surgeons, favoured the use of this technique even in patients who are at low or intermediate surgical risk [38, 39].
Nevertheless, TAVI is still affected by some major intra-operative complications, such as

prosthetic valve leakages (called aortic regurgitation) and interruption of the cardiac electrical signal (called atrioventricular blocks) [39–43]. Residual mild leaks associated with higher mortalities at two years are reported in up to 61% of patients after TAVI [43, 44]. The main causes of regurgitation are malpositioning or undersizing of the prosthetic device [40–42], an elliptic shape of the aortic annulus or an irregular distribution of calcium depositions within the surrounding tissue [45, 46]. In such cases, the expansion of the prosthetic valve might be incomplete or uneven. On the other hand, an oversized prosthesis is a predictor of future requirement of a permanent pacemaker [39]. Hence, choosing the right valve size is crucial to prevent any of these complications.
According to current clinical guidelines, the prosthetic valve selection is essentially based on pre-operative size assessment of the aortic annulus. This is usually performed either with 2D transesophageal echocardiography (TEE) or transthoracic echocardiography (TTE) [47]. However, it has been demonstrated that bidimensional echocardiographic images are not the best option to assess the complex 3D geometry and the elliptic shape of the aortic annulus, since they lead to underestimation of the annular diameter [47–50]. Moreover, BAV has been hypothesised to directly impact the annular geometry in up to 25% of the patients [51]. By relying on pre-operative geometrical data only, the device selection procedure neglects potential changes in the annular geometry caused by valvuloplasty.
To overcome the limitations of the current approach, different solutions have been proposed in the literature. Some of the them are based on alternative imaging modalities, while others suggest the integration of an intra-operative assessment of the implantation region. A comprehensive review of these methodologies will be presented in Chapter 2.

1.3 Aim and Objectives

The aim of this work was to develop a valvuloplasty robotic balloon catheter, capable of accurately determining the size of the aortic annulus from intra-balloon volume and pressure measurements. To achieve that, the following objectives were identified:

1. To conduct a thorough literature review in order to gain an understanding of existing techniques employed to size the aortic annulus and investigate the associated limitations and challenges;

2. To design a robotised inflation device that can be integrated with standard commercially available valvuloplasty balloon catheters. The system must be capable of precisely controlling the amount of fluid injected in the catheter over time, while simultaneously acquiring intra-balloon pressure data;

3. To explore analytical and numerical models of a standard BAV catheter inflation. A mathematical formulation that relates intra-balloon pressure and volume data to the balloon diameter during the inflation process is required;

4. To implement a sizing algorithm that exploits the mathematical model of the balloon inflation, to estimate the diameter of the annular structure in which the balloon is inflated;

5. To validate the proposed approach through experimental tests on rigid and compliant idealised phantoms of the aortic annulus;

The main contribution of this work is a novel technique for sizing the aortic annulus. The combination of this technique with current imaging-based sizing methods would not only enable to achieve more accurate measurements, but it would also allow to detect potential changes in the annular geometry caused by BAV. That could optimise TAVI device selection, potentially reducing the occurrence of the complications described in the previous section. The proposed approach relies on mechatronic and robotic solutions to extract additional relevant information from a treatment, BAV, that is already part of the standard TAVI procedure. Considering that it can be integrated with standard balloon catheters, already used in routine clinical practice, the level of additional complexity introduced by the proposed method is minimal.

1.4 Publications emerged from this project

Conference papers:

- Palombi, A., Bosi, G. M., Di Giuseppe, S., De Momi, E., Homer-Vanniasinkam, S., Burriesci, G., and Wurdemann, H. A. (2019). "Sizing the aortic annulus with a robotised, commercially available soft balloon catheter: in vitro study on idealised phantoms". In *2019 International Conference on Robotics and Automation (ICRA)*, Montreal, Canada. (pp. 6230-6236). IEEE.

- Palombi, A., Bosi, G., Di Giuseppe, S., De Momi, E., Homer- Vanniasinkam, S., Burriesci, G., Wurdemann, H. (2018). "Transcatheter aortic valve sizing from valvuloplasty sensing data". *8th World Congress of Biomechanics*, Dublin, Ireland. (P2297).

- Palombi, A., Gallarello, A., De Momi, E., Homer-Vanniasinkam, S., Burriesci, G., Wurdemann, H. (2018). "A new patient-specific, modular aortic vascular phantom

with clinically relevant mechanical properties". *8th World Congress of Biomechanics*, Dublin, Ireland. (P4621).

- Palombi, A., Bosi, G. M., Di Giuseppe, S., De Momi, E., Homer-Vanniasinkam, S., Burriesci, G., and Wurdemann, H. A. (2018). "Data mining using a soft robotic balloon catheter: sizing idealised aortic annular phantoms". In *Hamlyn Symposium Proceedings 2018*, London, England. (pp. 115-116).

Journal Papers:

- Gallarello, A., Palombi, A., Annio, G., Homer-Vanniasinkam, S., De Momi, E., Maritati, G., Torii, R., Burriesci, G. and Wurdemann, H.A. (2019). Patient-Specific Aortic Phantom With Tunable Compliance. *Journal of Engineering and Science in Medical Diagnostics and Therapy*, 2(4).

- Annio, G., Franzetti, G., Bonfanti, M., Gallarello, A., Palombi, A., De Momi, E., Homer-Vanniasinkam, S., Wurdemann, H., Tsang, V., Diáz-Zuccarini, V. and Torii, R. (2019). Low Cost Fabrication of PVA Based Personalized Vascular Phantoms for in Vitro Haemodynamic Studies: Three Applications. *Journal of Engineering and Science in Medical Diagnostics and Therapy*.

1.5 Thesis Structure

This thesis is structured as follows:

- Traditional and recently developed procedures for sizing the aortic annulus are reviewed in **Chapter 2 - Measuring Aortic Annulus Size: A Literature Review**. Both pre- and intra-operative approaches are presented highlighting the pros and cons of each technique;

- **Chapter 3 - Materials and Methods** thoroughly describes the development of all the elements that play a key role in the proposed sizing strategy. The two robotic inflation devices designed to acquire intra-balloon pressure and volume data are presented at the beginning of the chapter. Subsequently, the sizing algorithm is introduced. The algorithm can be subdivided into two main components, a mathematical model of the balloon free inflation and an automated routine to identify the point within the acquired dataset where full contact between the balloon and the annular walls is first attained. Two mathematical models of the balloon free inflation, one analytical and one numerical, were implemented for this project. The chapter concludes with a description of the idealised annular phantoms utilised for the tests;

- The experimental activities carried out to validate the proposed sizing methodology, as well as the associated results and observations, are presented in **Chapter 4 - Experimental Protocols, Results and Discussion**. The chapter opens with the tests performed on idealised rigid phantoms using the first prototype of the robotic inflation device. The second section summarises the experiments performed on idealised rigid phantoms with the second prototype of the robotic inflation device. Furthermore, it includes a performance comparison between the two platforms. The tests on idealised compliant phantoms, executed with the second platform, are described in section three. The chapter concludes with a preliminary analysis aimed at assessing the impact of injection speed on pressure-volume data and highlighting potential criticalities that would limit the applicability of the proposed sizing approach;
- **Chapter 5 - Conclusions and Future Work** sums up the main research findings of this work and suggests new directions that could be explored to potentially overcome the limitations of the current solution.

Chapter 2

Measuring Aortic Annulus Size: A Literature Review

The study described in this thesis was inspired by previous research conducted at UCL Mechanical Engineering in the field of transcatheter aortic prosthetic valves and balloon catheters. In particular, the work done by Biffi et al. [35, 52] and Tzamtzis et al. [28, 36] allowed to identify some seminal papers in the context of TAVI [25, 33, 53] and aortic annulus sizing [47, 54]. Such papers played a key role in finding the relevant references and connections that were used to broaden the literature review, investigating traditional and novel methods for assessing the size of the aortic annulus. In this chapter these methods are thoroughly presented and reviewed. For the sake of clarity, they can be classified into two macro groups, non-invasive pre-operative techniques and intra-operative techniques. The former represent the main class and they are essentially based on different imaging modalities. The latter are less common and they are not intended to be used as stand-alone procedures. Rather, their aim is to refine the results obtained from a pre-operative size assessment of the aortic annulus, in order to optimise TAVI device selection.

2.1 Pre-operative Techniques

Pre-operative techniques can be further subcategorised according to the dimensionality of the employed imaging modality. Two-dimensional techniques are essentially based on either transthoracic echocardiography (TTE) or transesophageal echocardiography (TEE). Multidetector computed tomography (MDCT), 3D transesophageal echocardiography (3D-TEE) and cardiovascular magnetic resonance (CMR) constitute the base for three-dimensional approaches.

2.1.1 Transthoracic and Transesophageal Echocardiography

TTE and TEE have been for many years the modalities of choice for TAVI device selection. Echocardiography exploits ultrasound to create moving images of the heart and assess the blood flow within cardiac chambers and vessels. A probe equipped with a piezoelectric crystal is used to generate pulses of high-frequency sound waves (1.5-7 MHz). While the waves travel across the body, the crystal is also used to detect the incident energy reflected by fluids and tissues (echo) [55]. If the propagation velocity of the wave is known, by measuring the delay between the transmission of a pulse and the detection of the associated echoes, it is possible to infer the distance of the tissues in front of the probe. The obtained distances can then be processed to reconstruct images of the scanned area.

TTE is the most common non-invasive type of echocardiography. During a transthoracic echocardiogram, the sonographer applies a gel to the chest of the patient. A probe is then moved around the chest to acquire various images of the heart. No special preparation is required for the patient, who is fully awake during the exam. The main advantages of TTE are simplicity, non-invasiveness and wide availability.
TEE is slightly more complex and invasive than TTE, as the probe has to be inserted inside the patient's esophagus. That introduces some procedural risks, like esophageal perforation and adverse reaction to medication, since sedation or general anaesthesia might be required. Nevertheless, TEE has the advantage of providing clearer images compared to TTE. In TTE ultrasonic waves have to penetrate through skin, soft tissue, ribs and lungs before reaching the heart, which results in a substantial attenuation of the ultrasound return signal. On the other hand, the heart rests directly upon the esophagus, hence the return signal is much stronger in TEE [56].

In both TTE and TEE the diameter of the annulus is measured between the hinge points of the aortic valve leaflets at the end of systole. At that point of the cardiac cycle the aortic root is pressurised and the stretch of the annular diameter is maximised. According to the American Society of Echocardiography [57], the parasternal long-axis view is used to perform the measure during TTE, while the midesophageal long-axis view is employed during TEE (Fig. 2.1). Recent studies have put the general reliability of TTE measurements for aortic annulus sizing into question, as it has been shown that the annular diameter by TTE yields systematically lower values than TEE [58, 59]. In addition, it has been demonstrated that both techniques might lead to a significant underestimation of the annular diameter [47–50, 58, 59], especially in patients with a pronounced elliptic annulus. According to the literature, the diameter measured through TTE and TEE is averagely 1-1.7 mm smaller

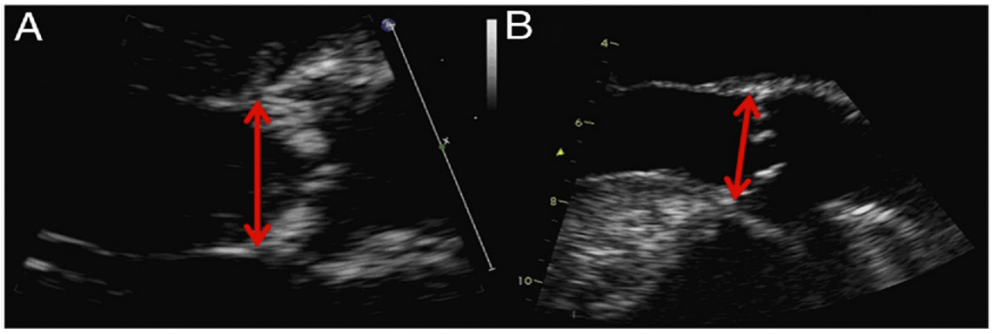

Fig. 2.1 Examples of measurements of the annulus diameter by a) transthoracic echocardiography and b) transesophageal echocardiography [48].

than the true diameter. It has been estimated that in 44% of the cases a bigger device size would have been chosen, if the annular diameter wasn't underestimated [60]. This problem is strictly related to the two-dimensional nature of these modalities. Measurements taken only using the hinges of the leaflets as references may not transect the full diameter of the aortic annulus. Instead, they could be a tangent across the annulus as shown in Fig. 2.2. Due to the

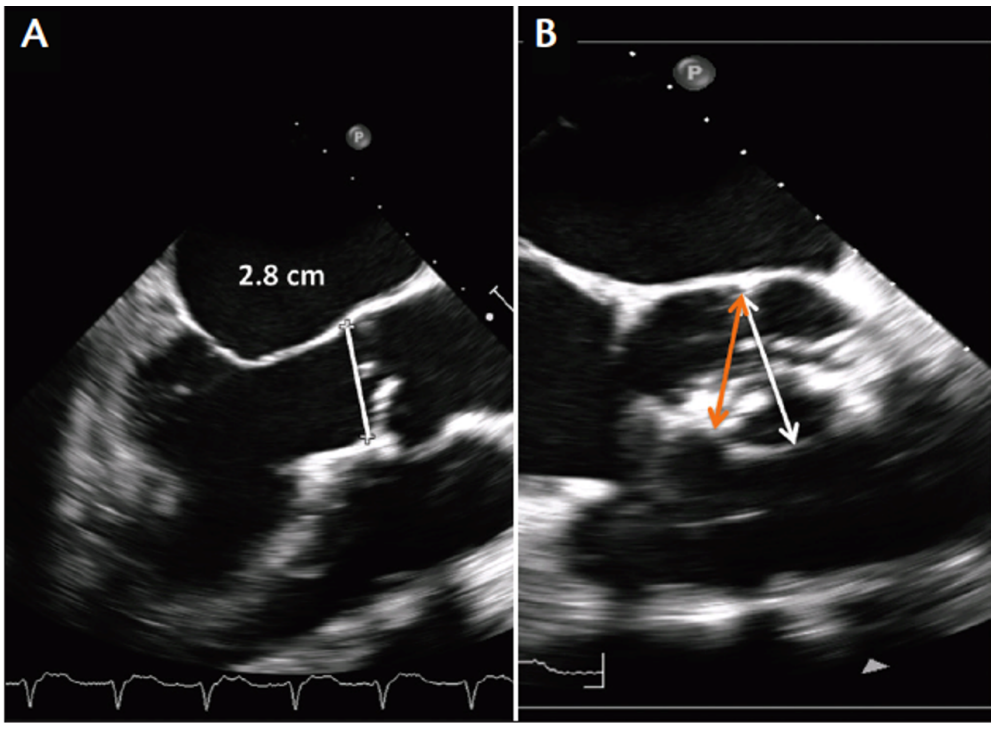

Fig. 2.2 a) Two-dimensional TEE measurement of the aortic annulus, from the hinge point of one leaflet to another (midesophageal long-axis view) b) The orange arrow indicates the underestimated measured diameter, while the white one represents the true diameter (sagittal view) [61].

aforementioned limitation, the use of alternative three-dimensional imaging modalities has been proposed for pre-operative size assessment of the aortic annulus and prosthetic valve selection.

2.1.2 Multidetector Computed Tomography

In cardiovascular medicine, multidetector computed tomography (MDCT) has been traditionally employed to detect, diagnose or follow up coronary artery disease. However, in recent years it has also played a key role in the context of TAVI for patient selection, procedure planning and prosthetic device sizing [62].

CT imaging exploits X-ray beams to create a sequence of cross-sectional images of the body. The structure of a CT scanner is mainly composed of the patient's bed and the gantry. The gantry is a large ring-shaped structure with a rotor that surrounds the patient. The rotor is equipped with an X-ray tube with energy levels in the range 20-150 keV. While the X-ray emitter rotates around the patient, a detector, placed in diametrically opposite side, is used to constantly receive the beams, once they have passed through the patient's body. Images are ultimately reconstructed by measuring from different angles the attenuation coefficients of X-ray beams in the volume of the object studied. Iodine-based radiocontrast agents, which can absorb exogenously given X-rays, are typically injected in the patient to enhance the quality of the reconstructed images. During the scan, the bed is translated along the axis of the rotor to acquire a series of cross-sectional images covering the area of interest [63].

For accurate size assessment of the aortic annulus by MDCT imaging, synchronisation with the electrocardiogram (ECG), through either retrospective ECG gating or prospective ECG triggering, is required [64]. Images are typically acquired at the beginning of systole (10-20% of the cardiac cycle) [65]. After the acquisition, 3D image data must be processed to create a plane that corresponds to the virtual basal ring of the aortic valve and contains the three lowest insertion points (hinge points) of the leaflets (Fig. 2.3). Based on the generated planar image, three different measurement strategies have been proposed for prosthesis selection [64]:

1. Measurement of the long and short diameters (D_L and D_S) of the oval aortic annulus. The mean diameter D is calculated by averaging the 2 values [$D = (D_L + D_S)/2$];

2. Planimetry of the area A of the aortic annulus and calculation of the diameter D that corresponds to this area under the assumption of full circularity [$D = 2\sqrt{(A/\pi)}$];

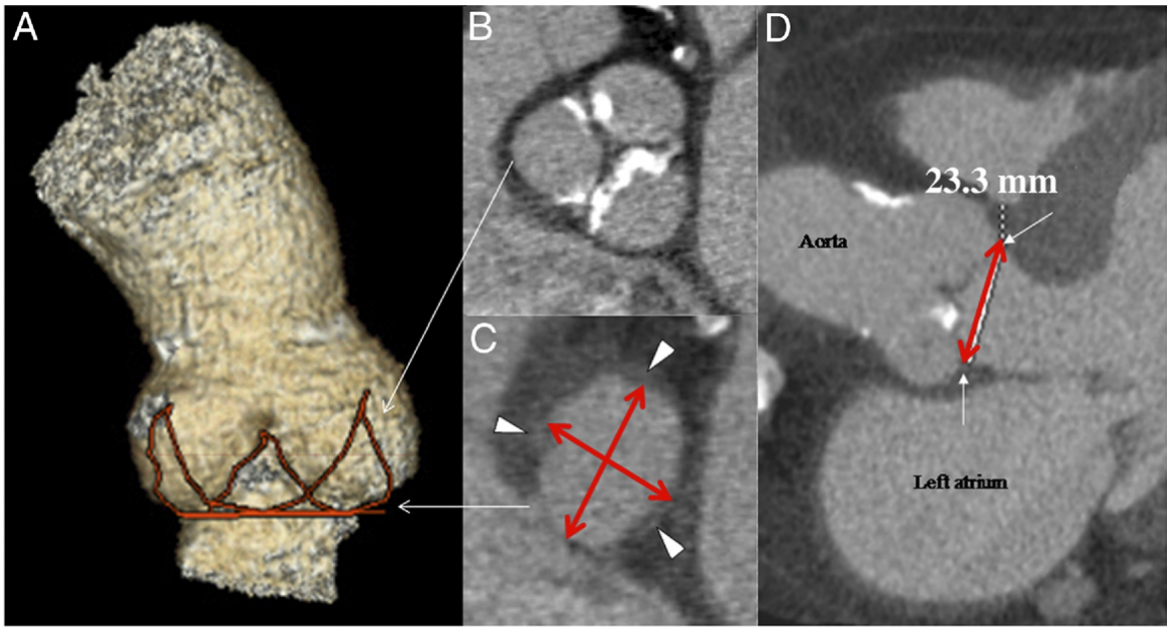

Fig. 2.3 a) 3-dimensional reconstruction of the aortic root b) Ascending aorta at the sinuses level (short-axis view) c) Aortic root at the level of the basal attachment of the aortic leaflet (short-axis view). The red arrows represent the long- and short-axis annular diameters. The white arrows are the hinge points of the leaflets d) Measurements of the aortic annulus in the 3-chamber view (plane similar to echocardiographic long-axis plane) taken from the hinge point of one leaflet to another [48].

3. Measurement of the circumference C of the aortic annulus and calculation of the diameter D that corresponds to this area under the assumption of full circularity ($D = C/\pi$);

The annular circumference is more stable than the annular area, as it undergoes negligible deformation throughout the cardiac cycle [51, 66]. However, it has been observed that measurements based on methods 1 and 2 offer better interobserver agreement across operators and platforms [67].
In a recent investigation comparing the influence of different imaging modalities (TTE, TEE, MDCT) on theoretical valve sizing, selection based on effective MDCT diameter showed the best agreement to theoretical choice based on intra-operative direct sizing [68]. Especially, MDCT appeared to be much more precise than TTE and TEE in patients with a pronounced elliptic annulus. Other studies demonstrated that MDCT-based sizing results in a reduced incidence of paravalvular aortic regurgitation compared to TEE-based sizing [64, 69, 70].
The aforementioned advantages lend strong support to a three-dimensional characterisation of the aortic annulus for TAVI device selection. Nevertheless, the application of MDCT is associated with some limitations due to the exposure to both contrast and radiation. In fact,

the risk of contrast nephropathy is very high in patients with renal morbidity, which is quite common in elderly people affected by AS [49, 50].

2.1.3 3D Transesophageal Echocardiography

Three-dimensional echocardiography is essentially based on the same principles described in section 2.1.1. However, a special ultrasound probe is used to scan volumes, instead of standard sector planes, and dedicated software is employed to process 3D datasets. While 64-128 piezoelectric crystals are mounted on a 2D-TEE probe, a 3D-TEE probe is equipped with a matrix array of 2500 miniaturised crystals [71]. Each crystal can be independently activated and steered to generate an ultrasound beam that covers a pyramidal scanning volume. 3D-TEE systems are capable of performing all the standard 2D functions. In addition, it is possible to use multiplane modes to simultaneously display independent scanning planes associated with the same heartbeat.

The multiplane mode allows to easily align the short-axis view of the aortic valve to obtain a cross-sectional image of the true annulus (Fig. 2.4). Similarly to MDCT, one of the three measuring strategies described in section 2.1.2 can be applied to the aforementioned planar

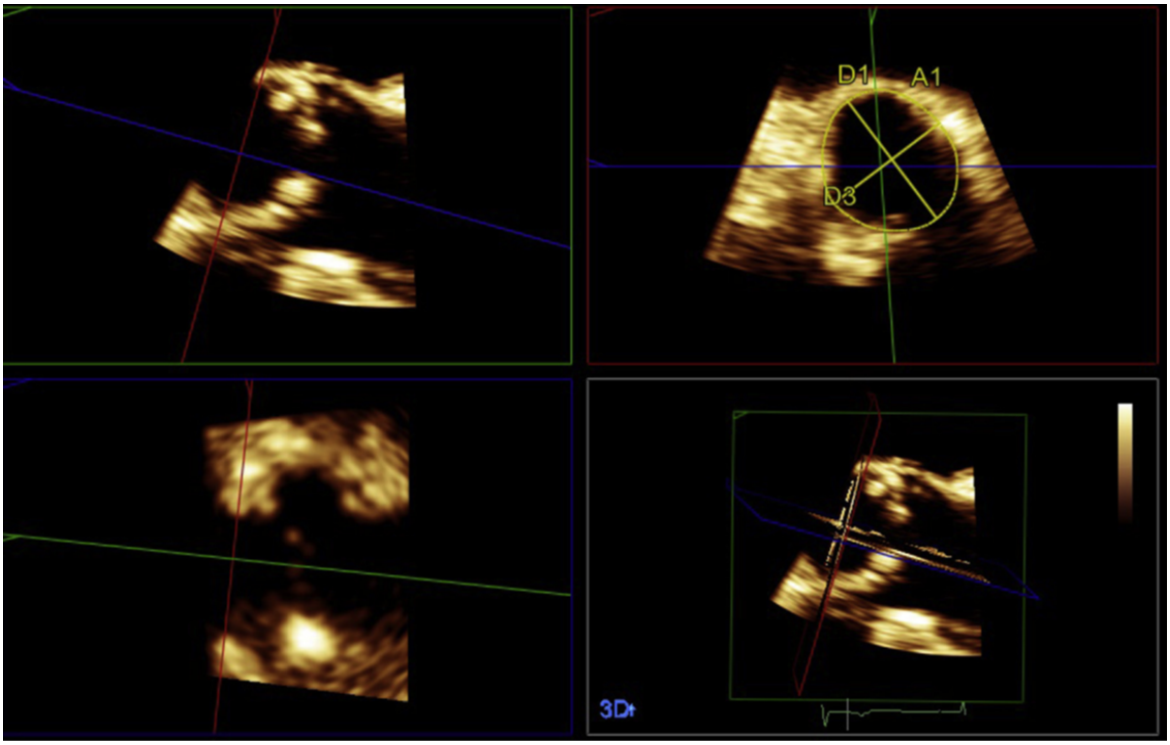

Fig. 2.4 Size assessment of the aortic annulus from 3D-TEE data. A1 is the annular area, D1 the maximum diameter and D3 the minimum diameter [72].

image to determine the annular diameter and select the size of the prosthetic device to be implanted.
Compared to MDCT, 3D-TEE has the benefit of providing three-dimensional information without the drawbacks associated with contrast administration and radiation exposure. However, the agreement between 3D-TEE- and MDCT-based prosthetic valve sizing is still debated. In a recent study by Podlesnikar et al. [73], 3D-TEE and MDCT measurements of the annular area led to the same prosthetic valve size in 88% of the patients. On the other hand, Vaquerizo et al. [74] reported that MDCT and 3D-TEE agreed in the prosthesis size in only 44% of patients, considering the diameter calculated from the annular perimeter, and in 38%, considering the diameter calculated from the annular area. It has to be said that the selection of the prosthesis size strictly depends on the defined sizing cutoffs. If we purely consider the estimated annular area, it has been widely reported in the literature that measurements performed by 3D-TEE are averagely 9.6-12.89% smaller than those obtained by MDCT [75–77]. Therefore, the combination of 3D-TEE cross-sectional measurements with sizing cutoffs originally defined for MDCT could potentially lead to significant undersizing of the prosthetic device.
Despite its growing potential, the application of 3D-TEE in the context of TAVI is relatively new. 3D-TEE is not as widely available as its two-dimensional counterpart [50]. Moreover, while software for MDCT analysis is highly evolved for the purposes of TAVI, the one for 3D-TEE requires more time to reach the same level of refinement [75]. Due to that, 3D-TEE is currently mainly regarded as an alternative to be used in patients with contraindications to MDCT [50].

2.1.4 Cardiovascular Magnetic Resonance

CMR is a rapidly evolving non-invasive imaging modality that offers comprehensive, multiparametric assessment of cardiac structure and function in a variety of clinical situations. In recent years, it has emerged in the context of TAVI as an alternative to echocardiography and MDCT for assessments of AS, procedural planning and post-TAVI follow-up [78].

The basic operating principle of magnetic resonance imaging (MRI) exploits the magnetic property of hydrogen atoms contained in the water molecules that form all the tissues of the human body [79]. Since its nucleus contains one proton, the hydrogen atom has a strong magnetic moment. In an MRI machine, the patient is placed inside a constant magnetic field that causes all the hydrogen protons to line up to either the patient's feet or the head. A radio frequency pulse is then used to disrupt this alignment. Once the pulse is turned off, the protons gradually re-align with the static magnetic field, emitting photons in the process. The

time required to regain the initial orientation strictly depends on the characteristics of the tissue. Therefore, by monitoring the emitted photons, it is possible to determine the various relaxation times and use their values to define the contrast in the MRI image [79].

Compared to 3D-TEE and MDCT, CMR is definitely less popular for aortic annulus sizing and TAVI device selection. CMR is more costly and time consuming than the other two imaging modalities, hence it is not easily accessible in all health services [78]. Furthermore, implanted devices like pacemakers, which are far from unusual in elderly people affected by

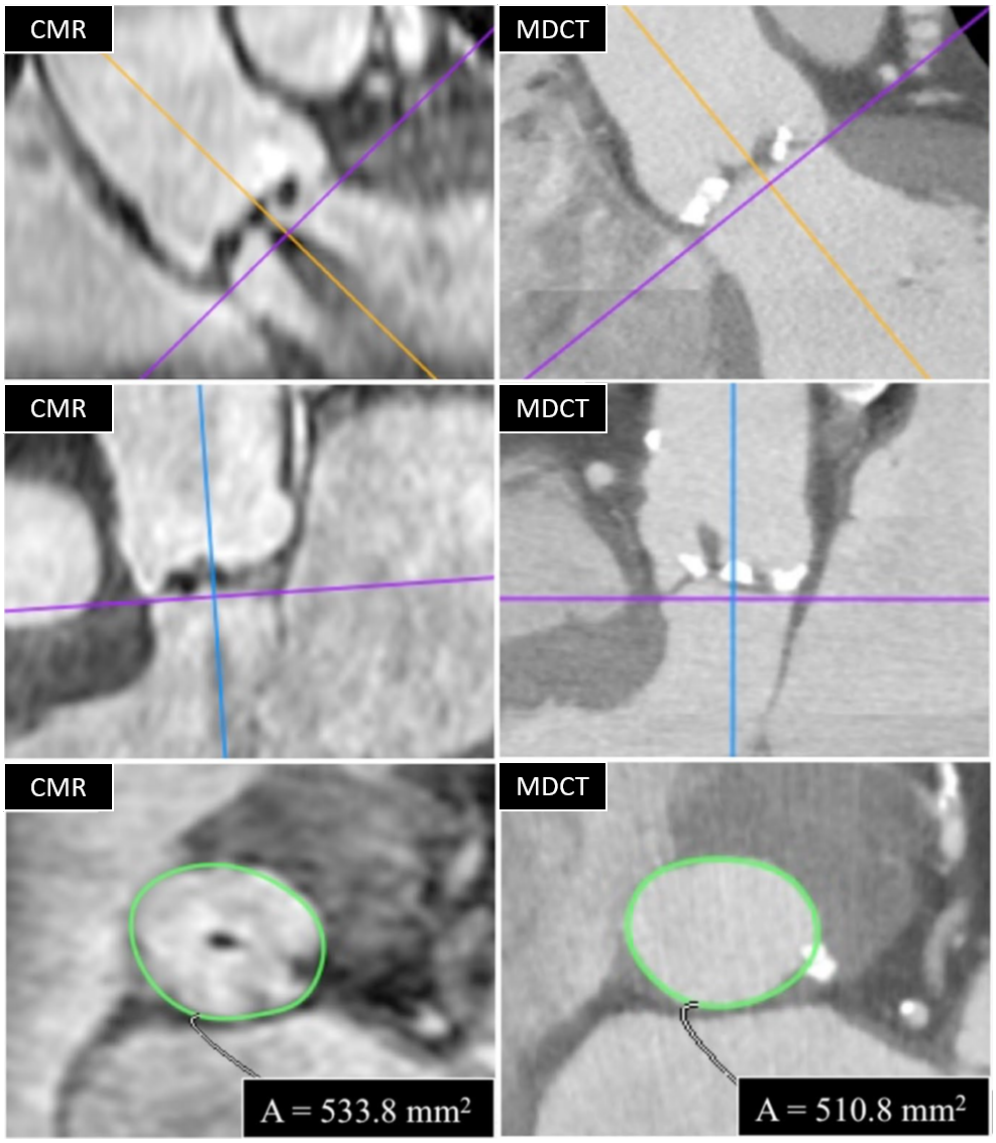

Fig. 2.5 CMR- and MDCT-based size assessment of the aortic annulus. The first two pictures of each column represent two orthogonal reconstruction planes. The pictures at the bottom are double oblique transverse reconstructions at the level of the aortic annulus [80].

AS, can be a relative or an absolute contraindication to CMR [78].
Nevertheless, recent studies demonstrated that non-contrast CMR could be a valuable alternative to MDCT, for patients with chronic kidney disease or intolerance to contrast media, and 3D-TEE, for patients with serious esophageal diseases [80–82]. A comparison between a CMR- and an MDCT-based size assessment of the aortic annulus is shown in Fig. 2.5. In terms of performance, CMR stands up to the level of confidence of MDCT. Faletti et al. [80] and Koos et al. [81] observed good agreement between CMR and MDCT annular measurements with low intraobserver and interobserver variability. Faletti et al. [80] also reported good agreement between CMR and 2D-TEE measurements and further investigated the performance of CMR in the valve sizing process. Substantial agreement was found between CMR and MDCT with mismatched prosthesis in only 18% of cases for the SAPIEN XT valve and 22% for CoreValve.

2.2 Intra-operative Techniques

Current clinical guidelines indicate that the size of the prosthetic valve to be implanted should be determined by exclusively relying on pre-operative imaging data. As discussed in the previous section, various imaging modalities have been employed to assess the size of the aortic annulus and each one is characterised by very specific advantages and disadvantages. In addition to the modality-specific drawbacks, all imaging-based approaches share two inherent limitations. Firstly they introduce a certain degree of subjectivity. Although fully automated aortic root analysis software has recently appeared in the market [83, 84], imaging data are usually manually processed and interpreted by the operator. Hence results may vary depending on operator experience [47]. Furthermore, the exact point of the cardiac cycle that should be taken into account for the assessment of the implantation region is still being debated. According to some clinicians the phase in which the annulus exhibits the largest diameter should be considered. Others recommend using the phase associated with the best image quality [80]. Secondly, as anticipated in section 1.2, they do not take into account potential changes in the annular geometry caused by BAV.
The aforementioned limitations could potentially be overcome by integrating intra-operative sizing methods into existing imaging-based procedures. To the best of our knowledge, only three intra-operative approaches have been described in the literature and they all rely on BAV balloon catheters. The work presented in this thesis clearly fits in this class of sizing techniques.

2.2.1 Calibrated Aortic Angiography

The idea of exploiting a valvuloplasty balloon catheter to double check the size of the implantation region right before valve deployment was originally described by Alain Cribier, the interventional cardiologist who performed the very first TAVI in 2002.
During this procedure, called calibrated balloon valvuloplasty, a standard BAV catheter is positioned inside the native aortic valve and then inflated with a diluted contrast agent through a three-way stopcock. As soon as the waist of the balloon is visibly compressed by the aortic annulus, the stopcock is closed and aortography is performed to exclude the presence of aortic regurgitation. Before deflating and withdrawing the catheter, the amount of contrast injected in the balloon is carefully recorded. On the bench, the balloon is inflated again to the same volume, and the associated diameter is determined by means of a sizing plate [85].
Cerillo et al. [47] demonstrated that, despite its simplicity, this technique can be extremely useful in case of conflicting measurements from multimodal pre-operative imaging, borderline annulus, massive and\or eccentric calcifications and bicuspid aortic valve. In their study, the described methodology led to a strategy change in 22.6% of the cases.

2.2.2 Valvuloplasty Pressure Balloon Catheter

An alternative approach to intra-operatively size the aortic annulus using a standard valvuloplasty balloon catheter was proposed by Babaliaros et al. [54, 86]. The protocol of this technique can be summarised as follows:

1. The starting BAV catheter is selected so that its diameter is within 2 mm of the patient's annular diameter measured by TEE;

2. The BAV catheter is connected via a 4-way stopcock to a 30 cc inflation syringe and an indeflator device for pressure measurements (Fig. 2.6 A);

3. The balloon is inflated on a test bench and the volume of saline-contrast mixture in the inflation syringe is adjusted, to guarantee an intra-balloon pressure of 2 atm at maximum inflation (Fig. 2.6 B);

4. A caliper is used to measure the diameter of the balloon at 2 atm (Fig. 2.6 C);

5. The balloon is deflated and positioned inside the implantation region. Then BAV is performed;

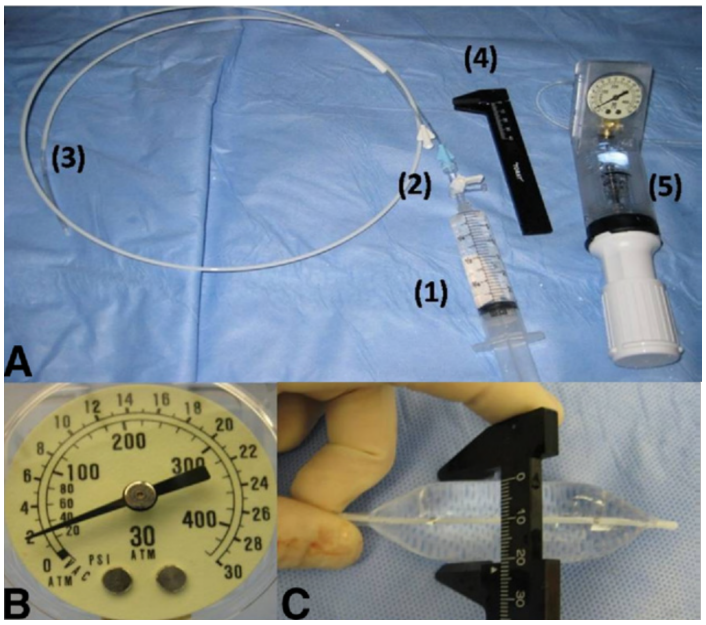

Fig. 2.6 (A) The equipment used for balloon aortic valvuloplasty (BAV) annulus sizing includes: (1) inflation syringe; (2) 4-way stop clock; (3) BAV catheter; (4) sterile caliper; and (5) indeflator pressure gauge. (B) The volume in the inflation syringe is adjusted so that complete emptying of the syringe results in a nominal pressure of 2 atm in the BAV catheter (measurement from indeflator pressure gauge shown). (C) At 2 atm, the balloon diameter is measured with a sterile caliper [54].

6. If the intra-balloon pressure measured does not exceed 2 atm, it means that the annular diameter is larger that the balloon diameter. On the other hand, if additional intra-balloon pressure is present, the diameter of the balloon must be larger than the annular diameter;

7. The minimum prosthesis size that is greater than the balloon diameter capable of generating additional intra-balloon pressure is selected for implantation;

This procedure shares many similarities with the method described in section 2.2.1. In particular, they both rely on standard commercial BAV catheters and require manual calibration to establish a relationship between balloon diameter and volume of injected fluid. The main difference is the condition used to select the prosthetic valve size, based on the balloon diameter. In calibrated aortic angiography, the balloon diameter associated with the absence of para-balloon leakage during aortography is taken as a reference, instead of the balloon diameter associated with additional intra-balloon pressure. Despite this difference, these two approaches lead to very similar results in terms of percentage of valve size changes, as a consequence of intra-operative size assessment of the aortic annulus [47].
Assuming that the performance of the two techniques is the same, the one described in this

section has the benefit of not requiring imaging. That clearly makes the process simpler, less invasive and potentially more objective, since intra-balloon pressure data do not require interpretation by the operator.
The main drawback of both intra-operative techniques is the lack of precision. Firstly, the tools currently employed, such as the inflation syringe and the pressure gauge on the indeflator, are not specifically designed for the task and they offer very low resolution. Secondly, every aspect of the procedures, from fluid injection to pressure reading, is entirely manual. The lack of precision might not be a problem now because the range of available TAVI device sizes is quite limited. In the future, the percentage of cases where the annulus is borderline will increase with the increased range of prosthesis sizes [87], hence better precision will be mandatory.

2.2.3 Valvuloplasty Conductance Balloon Catheter

A more engineered approach for intra-operatively assessing the size of the aortic annulus was described by Svendsen et al. [60]. They developed a novel BAV catheter equipped with a series of electrodes placed on the surface of the inner guidewire pipe (Fig. 2.7). By connecting the catheter to an external computer console, it is possible to apply a small amount of alternating electrical current I (136 μA_{p-p}, 1-10 kHz) through the two outer electrodes, while measuring in real-time the voltage V between adjacent pairs of middle electrodes. According to Ohm's Law, the conductance G can be calculated from I and V as:

$$G = \frac{I}{V}$$

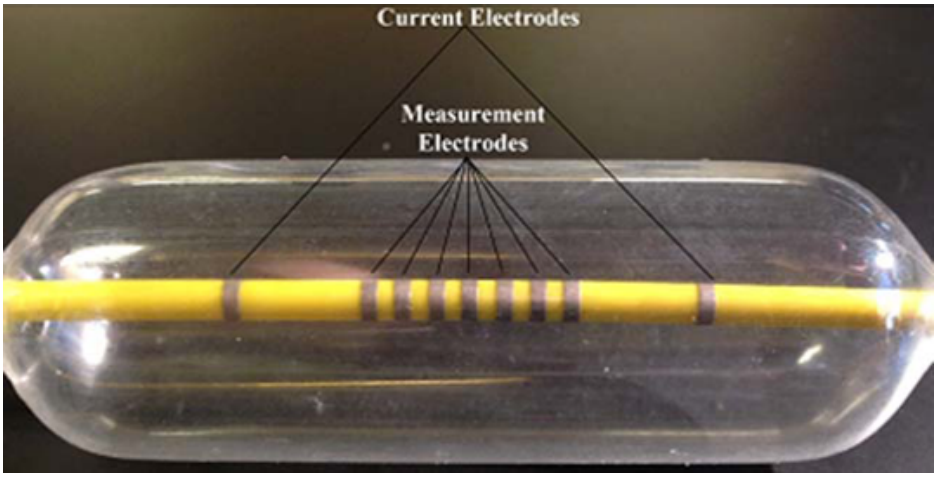

Fig. 2.7 Placement of the electrodes inside the conductance BAV catheter [60].

Based on the definition of conductance, the cross-sectional area *CSA* of the balloon between adjacent measuring electrodes can be expressed as:

$$CSA = \frac{IL}{V\sigma}$$

where L is the known fixed distance between the electrodes and σ is the conductivity of the fluid used to inflate the balloon. Obviously, the balloon diameter can be easily inferred from the *CSA*, under the assumption of perfect circularity.
The device, which is not commercially available, was first tested on the bench using circular steel, glass and plastic rigid phantoms with inner diameters ranging from 20 to 30 mm. The accuracy of the measured diameter compared to the true diameter was -0.11 ± 0.26 mm. Ex vivo experiments on explanted domestic swine hearts were also performed. Measurements of swine aortic annuli taken with the conductance balloon catheter were compared against measurements taken with dilators (mean difference -0.3 ± 1.1 mm) and CT measurements (mean difference -1.0 ± 1.6 mm).
Although this method is technically more advanced and accurate than the two intra-operative techniques described in the previous subsections, it is characterised by two key limitations. Firstly, the relatively complex system this technique relies on cannot be immediately integrated with BAV catheters currently employed in routine clinical practice. Secondly, while it provides a precise solution to measure the cross-sectional area of the BAV catheter, it does not offer an equivalently precise way to understand when the balloon has made contact with the annular walls. Apposition of the balloon against the valve leaflets and the annular walls can only be verified either through imaging or by adopting the pressure-based strategy described in section 2.2.2.

2.3 Summary

In this chapter, pre-operative and intra-operative techniques for assessing the dimensions of the aortic annulus were reviewed.
Pre-operative approaches based on TTE and TEE were traditionally considered the golden standard for TAVI device selection. Nevertheless, new methods based on three-dimensional imaging modalities have emerged in recent years. The advantages and the disadvantages of these methods are summarised in Tab. 2.1.
Pre-operative techniques alone might not be able to guarantee optimal prosthetic valve selection in all patients. In fact, they do not take into account potential changes in the annular geometry introduced by BAV and they are affected by a certain degree of subjectivity. Due

to that, the integration of intra-operative techniques into the current TAVI workflow was proposed. The intra-operative approaches reported in the literature and their main advantages and disadvantages are summarised in Tab. 2.2.

Imaging Modality	**Main Advantages**	**Main Disadvantages**
TTE\TEE [47–50, 58, 59]	Golden standard for many years, simple, widely available	Underestimation of the annular diameter
MDCT [49, 50, 62–70]	Precise 3D information, well developed for TAVI	Exposure to contrast and radiation
3D-TEE [50, 71–77]	3D information (precision still debated, see section 2.1.3)	Not widely available, not well developed for TAVI yet
CMR [78–82]	Precise 3D information	Expensive, time consuming, incompatible with implanted devices like pacemakers

Table 2.1 Pre-operative techniques to size the aortic annulus, advantages and disadvantages.

Technique	**Main Advantages**	**Main Disadvantages**
Calibrated Aortic Angiography [47, 85]	Based on commercial BAV catheters	Contrast injection, balloon-annulus apposition interpreted from images, lack of precision
Pressure Balloon Catheter [47, 54, 86]	Based on commercial BAV catheters, balloon-annulus apposition evaluated objectively	Lack of precision
Conductance Balloon Catheter [60]	Accurate estimate of the balloon cross-sectional area	Based on a new BAV catheter design, never tested on humans

Table 2.2 Intra-operative techniques to size the aortic annulus, advantages and disadvantages.

Chapter 3

Materials and Methods

In this chapter, the equipment and the methods employed to achieve the aim and objectives of this project are presented. Section 3.1 describes the two robotic inflation devices designed to experimentally extract intra-balloon pressure-volume curves. In Section 3.2, the commercial BAV balloon catheter and the two mathematical models devised to characterise the balloon inflation are introduced. The algorithm implemented to size the annular structure in which the balloon is inflated is outlined in Section 3.3. The chapter concludes with the description of the idealised annular phantoms used to experimentally validate the proposed approach.

3.1 The Robotic Inflation Devices

Two different robotic inflation devices were prototyped. The first one was manufactured to experimentally perform a preliminary evaluation of the basic idea upon which the project was initiated and highlight potential criticalities. By neglecting the injection speed required in the real application (see Section 1.1.3), it was possible to design an extremely cheap device that costs approximately 200£ and can be programmed using open source software.
The second platform was designed to overcome the limitations of the first prototype in terms of speed, precision and structural stiffness. That was achieved by employing industrial grade mechanical and electrical components, which raised the overall cost of the system to approximately 2000 £. Nevertheless, the second prototype shares almost the same core functional logic as the first one. Both systems are described in the following subsections.

3.1.1 The First Prototype

The first prototype of the robotic inflation device, represented in Fig. 3.1, essentially consists of a 10 ml syringe (Terumo Corporation, Shibuya, Tokyo, Japan), fixed on a 3D printed

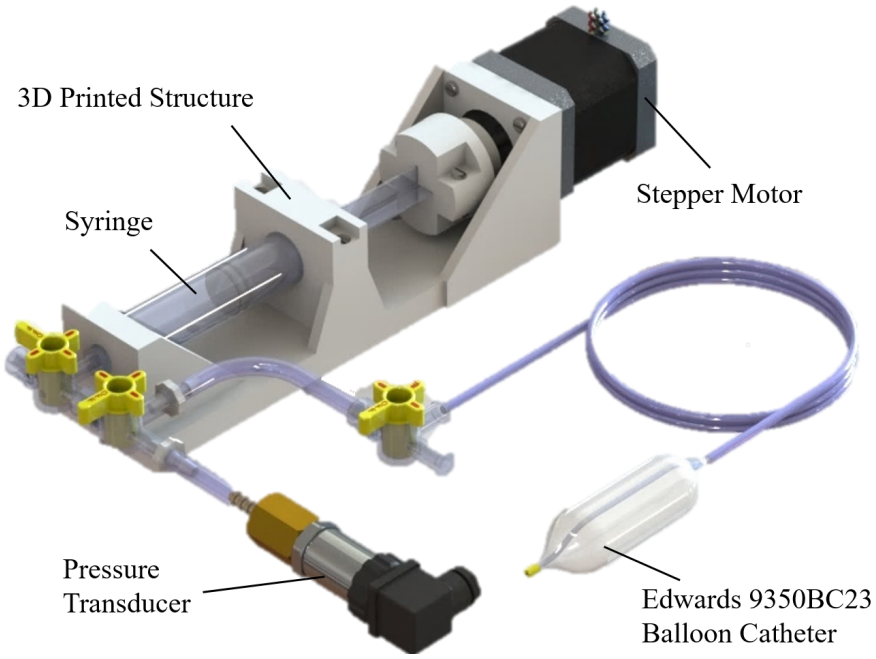

Fig. 3.1 3D rendered first prototype of the robotic inflation device.

structure made of VisiJet EX200 resin (3D Systems, Rock Hill, SC, US). The movement of the plunger is regulated by a Nema 17 non-captive linear stepper motor with anti-rotation mechanism (17HS1003, RobotDigg, Shanghai, China). The lead screw equipped on the motor is characterised by a Tr8*8 trapezoidal thread (outer diameter 8 mm; lead 8 mm). That implies that the plunger linearly travels 8 mm for each full rotation of the motor. The relevant technical specifications of the linear actuator are summarised in Tab. 3.1. The suitability of the motor, which was already available in our laboratory at the beginning of this project, was checked by performing the calculations included in Appendix A.1.

The inner diameter of the syringe is 15.8 mm. By considering the plunger shaft perfectly rigid and assuming that the syringe is filled completely with an incompressible liquid, it can be determined that approximately 0.008 ml of fluid are moved by a single motor step. Hence, the amount of liquid injected into or extracted from the balloon can constantly be monitored by simply counting the number of executed steps in an open-loop fashion.

Pressure data is acquired using a PXM319-007A10V absolute pressure transducer (Omega

Holding Torque	Rated Current	Detent Torque	Steps per Revolution	Screw Thread
260 *Nmm*	0.4 *A*	12 *Nmm*	200	Tr8*8

Table 3.1 Technical specifications of the linear stepper motor.

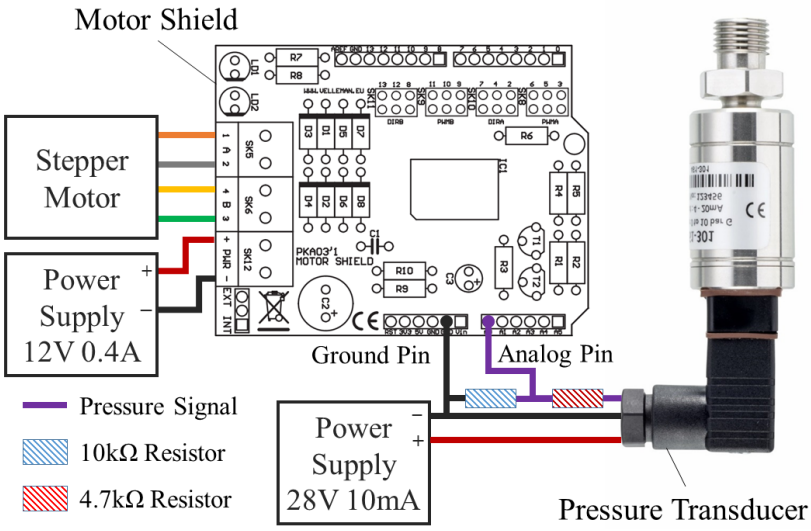

Fig. 3.2 An Arduino Uno board with a motor shield stacked on top is used to both control the stepper motor and acquire pressure data.

Engineering Inc., Stamford, CT, US). The motor and the sensor are interfaced with an Arduino Uno microcontroller combined with a VMA03 motor shield (Velleman, Gavere, Belgium) (Figure 3.2). The shield allows to exploit an external power supply and four digital pins of the Arduino board to control motor direction and speed. A single analog input of the microcontroller is used to acquire pressure data. The balloon catheter employed in this project (see Section 3.2 for a detailed description) operates over an absolute pressure range of $0-5$ atm ($\simeq 0-0.5$ MPa). Since the maximum analog input voltage of the Arduino is 5 V, a voltage divider is required to rescale the output of the transducer ($0-7$ bar $= 0.7$ MPa; $0-10$ V) and make our pressure range of interest readable (Figure 3.2). A system of PVC pipes and 3-way stopcocks with luer-lock fittings (Cole-Parmer, Vernon Hills, IL, US) is used to hydraulically connect the balloon catheter and the sensor to the syringe (Figure 3.1).

The robotic inflation device is entirely managed by a computer program developed in Processing, an open-source Java-based programming language and integrated development environment. Communication via USB cable with the Arduino is enabled by the Firmata protocol, which is implemented in the firmware uploaded on the microcontroller. The program is composed of two main code blocks: the graphical user interface (GUI) and the Processing sketch. The GUI, shown in Fig. 3.3 allows the user to specify the modality of operation (balloon inflation\deflation), the amount of fluid to be injected\extracted in millilitres and the speed of the plunger, in terms of delay between the motor steps in milliseconds. Intra-balloon pressure and volume data are plotted in real-time on the graph located at the bottom right corner of the GUI.

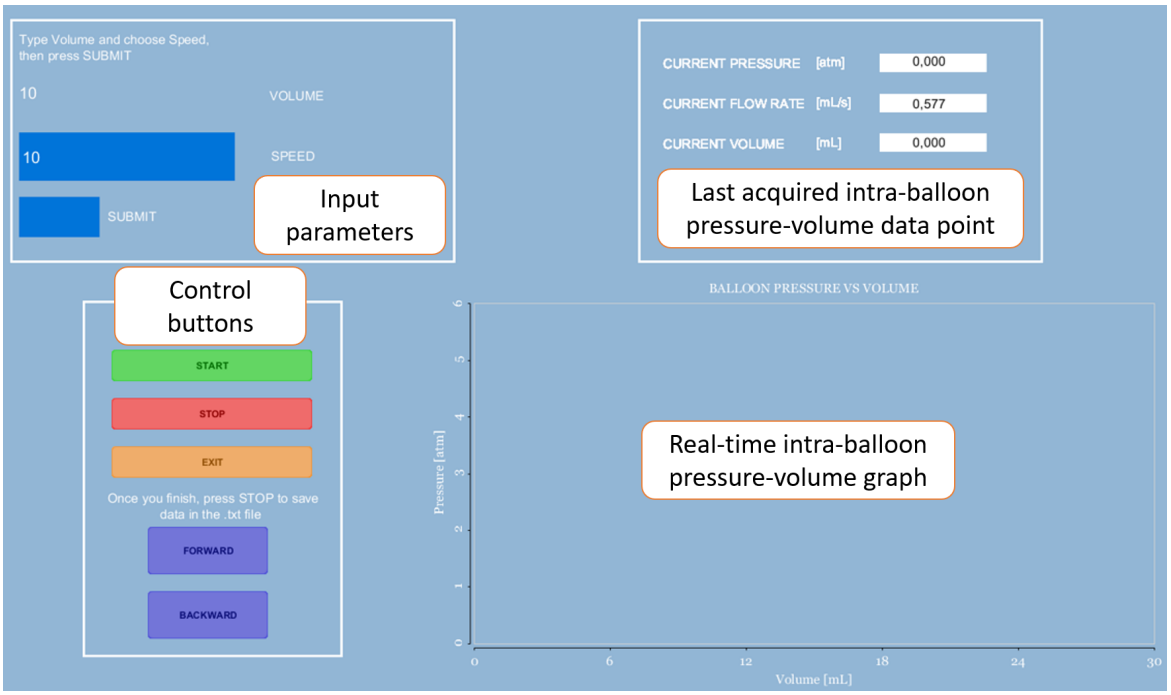

Fig. 3.3 The graphical user interface of the first robotic inflation device.

All low- and high-level functionalities required to operate the platform and manage data acquisition are implemented in the Processing sketch. Basically, the code in the Processing sketch takes the inputs from the GUI and feeds them to an automated routine, which drives the stepper and regulates data acquisition as shown in Algorithm 1. At the end of the routine,

Algorithm 1: Implementation of the automated motor control and data acquisition routine.

```
Input Desired Volume;
Input Desired Speed;
Set Inflation/Deflation;
if (Start Button is pressed) then
    Current Volume = 0;
    Measure Intra-balloon Absolute Pressure;
    Open Text File;
    Write Intra-balloon Pressure and Volume to Text File;
    while (Current Volume < Desired Volume) AND (Pressure < 4 atm) do
        Move One Step Forward/Backward;
        Recalculate Current Volume;
        Measure Intra-balloon Absolute Pressure;
        Write Intra-balloon Pressure and Volume to Text File;
    end
    Close Text File;
end
```

a text file, containing an absolute pressure value in [atm] and a volume value in [ml] for each step executed by the motor is exported. For a detailed description of the code inside the Processing sketch, see Appendix B.1.

3.1.2 The Second Prototype

In terms of hardware architecture, the second prototype, shown in Fig. 3.4, is almost identical to the first one. Nevertheless the whole system is designed to be structurally stronger and operate at higher speeds.
The platform embeds a 50 ml gas tight syringe (ILS, Stuetzerbach, Germany), equipped with luer-lock connector, metal collar and PTFE seals. The selected product is specifically designed to be installed on syringe pumps and it can withstand a pressure up to 8 atm. While the syringe barrel is fixed on a 15 mm thick Perspex plate by means of two holders made from AISI 304 stainless steel, the plunger is connected to a Thomson PC25LX999B03-0100FM ball screw linear actuator (Altra Industrial Motion, Braintree, MA, US) through a custom clamping joint, also made from AISI 304 stainless steel. The holders, the joint and the

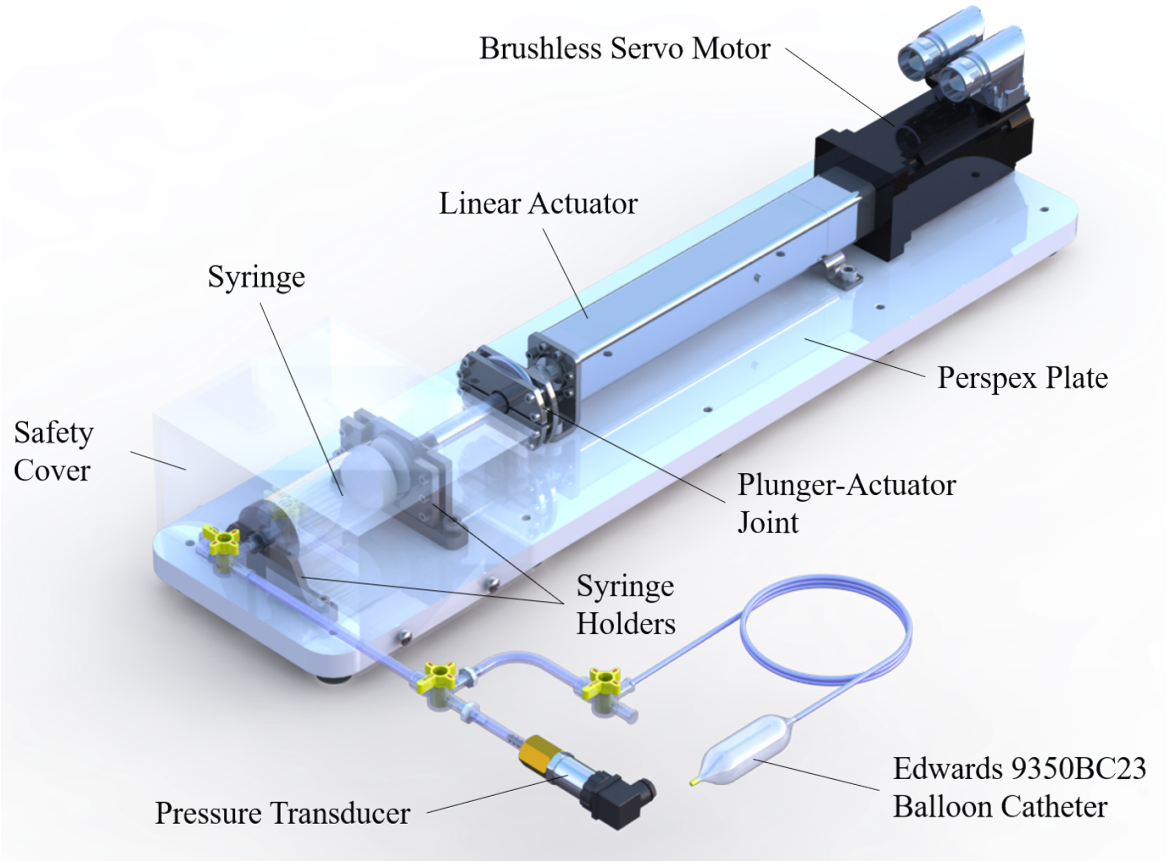

Fig. 3.4 3D rendered second prototype of the robotic inflation device.

plate were modelled using Solidworks (Dassault Systèmes, Vélizy-Villacoublay, France) and machined at the UCL mechanical workshop. The main technical specifications of the linear actuator are summarised in Tab. 3.2.

Screw Lead	Stroke Length	Max Input Speed	Max Acceleration	Max Linear Speed	Repeatability ($\pm$ error)	Load (Dynamic)
3 *mm*	100 *mm*	8000 *RPM*	10 m/s^2	1.33 m/s	0.01 *mm*	1250 *N*

Table 3.2 Technical specifications of the Thomson PC25 linear actuator.

A Kollmorgen AKM22G-ANDNC-00 brushless servomotor (Altra Industrial Motion, Braintree, MA, US), whose main technical specifications are included in Tab. 3.3, is coupled with the linear actuator to control the movement of the plunger. The motor is equipped with an

Rated Speed	Rated Torque	Rated Power	Max Speed	Peak\Continuous Stall Torque	Peak\Continuous Stall Current
7000 *RPM*	0.74 *Nm*	0.54 *kW*	8000 *RPM*	2.79\0.88 *Nm*	19.3\4.82 A_{rms}

Table 3.3 Technical specifications of the Kollmorgen AKM22G servomotor associated with its maximum rated DC bus voltage (160 *V*).

internal smart feedback device (SFD). The SFD exploits a resolver to analogically track the position of the motor shaft. A 4 wire interface allows to digitally send shaft position information and motor temperature data to the drive. The feedback system guarantees an accuracy of $\pm$9.75 minutes of arc on the measured shaft angular position with a resolution of 0.0013 minutes of arc.

The linear actuator and the motor were mainly selected according to the description of the BAV procedure provided in Section 1.1.3. Starting with a completely empty balloon catheter, the platform must be capable of fully inflating it in approximately 3 s. Both maximum intra-balloon pressure acting on the plunger and estimated head losses associated with viscous effects were considered, as thoroughly explained in Appendix A.2.

Based on the geometry of the syringe and the linear actuator, under the assumption of perfectly rigid shaft and incompressible liquid, the volume of fluid injected into or extracted from the balloon catheter can be calculated by monitoring the angular displacement of the motor shaft. Since the inner diameter of the syringe is 32.57 mm, it can be determined that approximately 0.007 ml of fluid are moved when the motor shaft rotates 1°. While this strategy is practically identical to the one applied to the first prototype, the second prototype

provides enhanced precision for two main reasons. Firstly the overall higher mechanical stiffness of the second prototype is more in line with the perfectly rigid shaft assumption. Secondly and most importantly, a closed-loop strategy is employed, instead of an open-loop one, to control the position of the plunger. The position feedback of the SFD ensures an accuracy of roughly ± 0.001 ml.
The rotation of the motor is managed by a Kollmorgen AKD-T00606-ICAN-E000 BASIC drive with expanded I\O (Altra Industrial Motion, Braintree, MA, US). The peculiar feature of the chosen drive, whose electrical data are reported in Tab. 3.4, is that it can be programmed in two ways. The first option is to use a programmable logic controller (PLC) connected to

Continuous Current	Peak Current	Continuous Output Power	Rated Main Volt. Supply	Rated Main Input Freq.	Auxiliary Volt. Supply
6 A_{rms}	18 A_{rms}	2 kW	120 to 240 V	50-400 Hz or DC	24 V_{DC}

Table 3.4 Technical specifications of the Kollmorgen AKD-T00606 drive.

the drive using a standard industrial communication protocol, such as EtherCAT, PROFINET RT or Modbus/TCP. The second option is to connect the drive to a PC via Ethernet cable and program it directly through the coding interface available in the AKD Workbench software, freely distributed by Kollmorgen. To keep the platform compact and cost-effective, the latter solution was adopted in this project.
Pressure data is measured using the same PXM319-007A10V absolute pressure transducer described in Section 3.1.1. The signal is acquired through one of the two analog inputs available on the AKD-T00606 drive. Since the operating range of the analog pins is ± 12 V_{DC}, no tension divider is required to interface the pressure sensor with the drive. As shown in Fig. 3.4, the same system of PVC pipes and 3-way stopcocks, utilised for the first platform, is used to hydraulically connect the balloon catheter and the sensor to the syringe.
From the electrical point of view, the motor drive is connected to a standard electrical socket which provides a nominal single-phase voltage of 230 V_{AC} with a frequency of 50 Hz. A dual output DC power supply is used to provide 24 V to the auxiliary components of the drive and 28 V to the pressure transducer.

Two separate environments, available in the AKD Workbench software, are used to program the motion sequences of the plunger and manage data acquisition. The Program View, shown in Fig. 3.5, was used to design a console application that allows the user to select among three operational modalities and input the relevant control parameters. The application is based on the AKD BASIC programming language. The first modality corresponds almost

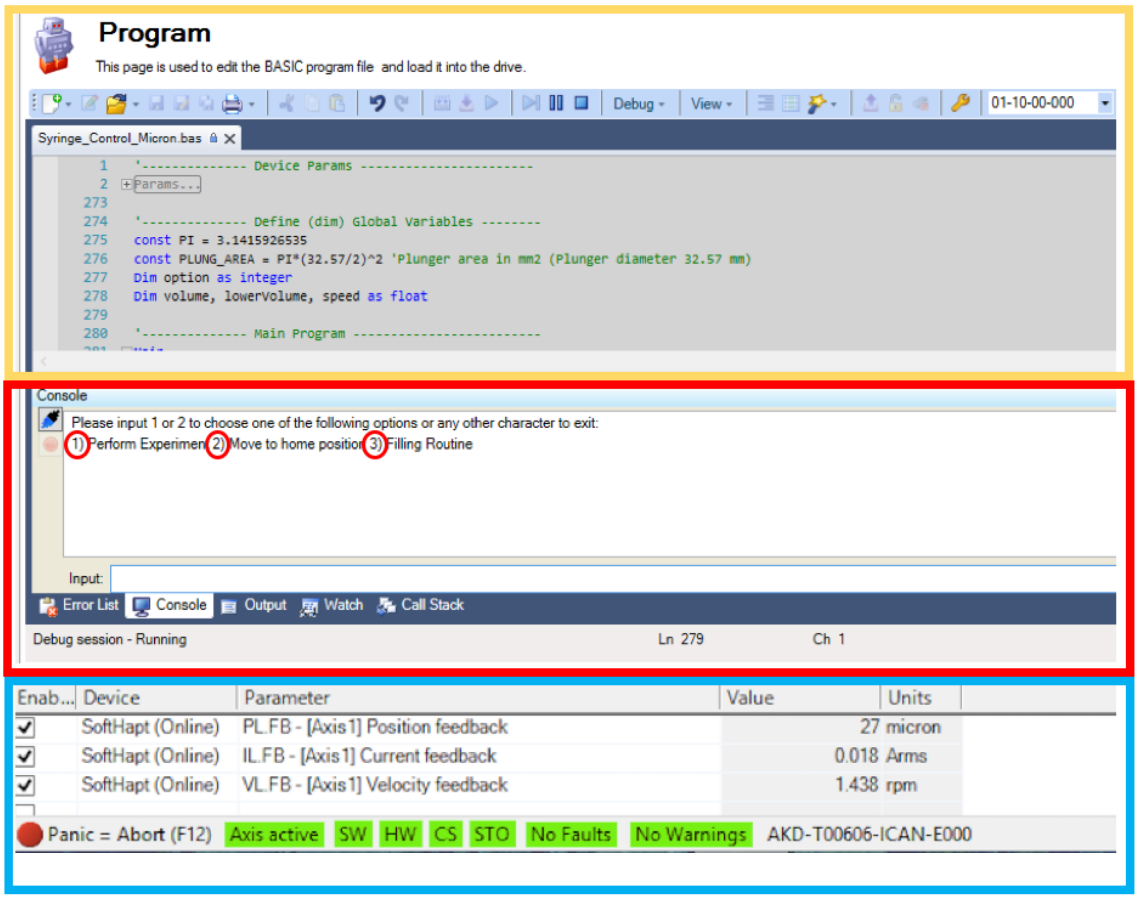

Fig. 3.5 The Program View environment: the yellow box highlights the area where the actual BASIC code is written; the red box shows the console that can be used by the user to select one of the implemented functional modalities of the platform; the blue box indicates the area where various feedback parameters can be displayed [88].

entirely to the control logic described in Algorithm 1. The second one enables the user to perform the homing procedure of the linear servo axis. The third one allows to move the syringe plunger back and forth between two specifiable positions at a certain speed. For a detailed description of the AKD BASIC code see Appendix B.2.

In the Scope environment the user can choose up to six channels to be recorded simultaneously and plotted on the screen in real-time. The position feedback of the linear servo axis, the analog input associated with the pressure transducer and a digital output were selected for this application. The digital output is only used to label data recorded after the motor is stopped, because the maximum intra-balloon pressure has been reached. The sampling rate, the duration of the recording and the trigger can be configured through the graphical user interface. In this platform the recording is always triggered by a command in the AKD BASIC code. Acquired data can be exported as a .CSV file for further processing.

Table 3.5 summarises the main advantages and disadvantages of the two robotic inflation devices described in this section.

Inflation Device	**Main Advantages**	**Main Disadvantages**
First Prototype	Cheap and easy to manufacture ($\approx$ 200£) Open-source hardware and software Highly customisable graphical user interface	Slow injection speed (<0.5 ml/s) Low injectable volume (10 ml) Open-loop strategy to control the position of the plunger
Second Prototype	Suitable injection speed for the real case scenario (>10 ml/s) High injectable volume (50 ml) Closed-loop strategy to control the position of the plunger	Expensive ($\approx$ 2000£) Heavier and bulkier Rigid console user interface

Table 3.5 Comparison between the two robotic inflation devices.

3.2 The Valvuloplasty Balloon Catheter

Balloon catheters currently employed in the medical industry can be classified into two main groups, based on the pressure at which they operate. Low-pressure balloons are made of elastomers, such as latex or silicone, and they are usually employed in fixation and occlusion. Typically they are dip-molded in a tubular shape that is subsequently expanded several times its actual operating size. Therefore, they are not designed to be inflated to precise dimensions and keep well defined shapes during inflation [89].
High-pressure balloon catheters are designed to apply forces in medical procedures like angioplasty and valvuloplasty. Hence, they must ensure a controlled and repeatable size during inflation to prevent damage to the vessels. For that reason, they are molded to their inflated geometry during the manufacturing process and they are made of materials characterised by high tensile strength and low compliance. PE, PET, PU, PVC and nylon are some of the materials that can be used to manufacture high-pressure balloon catheters [89].

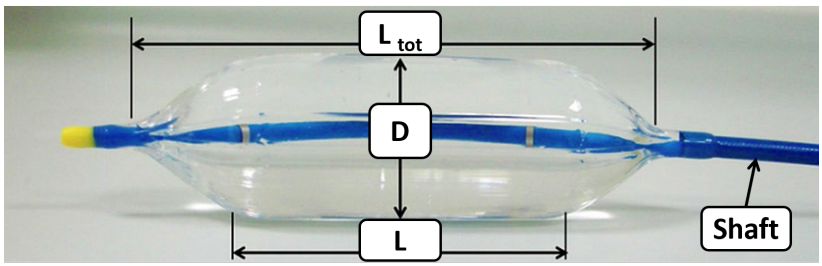

Fig. 3.6 The Edwards 9350BC23 balloon catheter and its geometrical parameters. D and L are respectively the outer diameter and the length of the central cylindrical region. L_{TOT} is the total length of the balloon [35].

A standard high-pressure balloon consists of a cylindrical body and two ends that can have various shapes. The balloon is wrapped around a long tube, the catheter shaft, characterised by the presence of two concentric cavities. The inner cavity is required for the guidewire, while the outer one is used to inflate the balloon. The portion of the shaft inside the balloon is characterised by an extra length that makes it look slightly curved when the catheter is deflated. This design allows such portion to simply straighten up during inflation, avoiding potentially harmful longitudinal stress. Therefore, the axial load associated with the intra-balloon pressure is fully taken by the balloon membrane. The proximal end of the shaft embeds a standard Y-connector that provides access to the two cavities.
The BAV balloon catheter used in this study is the Edwards 9350BC23 (Edwards Lifesciences, Irvine, CA, US), which is part of the Edwards SAPIEN 3 transcatheter prosthetic valve implantation kit. The device, shown in Fig.3.6, is designed to reach a diameter of 23 mm at the nominal intra-balloon gauge pressure of 4 atm ($\simeq$ 0.4 MPa). The nominal pressure is associated with a nominal volume of 21 ml. The main specifications of the Edwards 9350BC23 are listed in Tab. 3.6.

Nominal Diameter	23 mm
Nominal Volume	21 ml
Nominal Gauge Pressure	4 atm
Rated Burst Gauge Pressure	6 atm
Total Length	75 mm
Cylindrical Region Length	40 mm
Catheter Shaft Diameter	9 F (3 mm)
Catheter Shaft Length (from tip to Y-connector)	1300 mm

Table 3.6 Technical specifications of the Edwards 9350BC23 valvuloplasty balloon catheter.

3.2.1 Balloon Material Characterisation

The balloon material was mechanically characterised as part of a previous project carried out in our research group [35, 52]. Uniaxial tensile tests were performed to retrieve the characteristic stress-strain curve of the material and check for isotropy.
A Zwick Roell Z5.0 (Zwick GmbH & Co.,Ulm, Germany) machine, connected via Ethernet to a computer, was used for the tests (Fig. 3.7). The machine is capable of applying a maximum traction load of 5 kN. Its crosshead can travel at a speed of up to 600 mm/min with a positioning accuracy of $\pm 2\ \mu m$. The force applied to the test specimen is measured in real-time with a 0.5 grade load cell, according to DIN EN ISO 7500-1. A software interface allows to operate the machine and post-process measured data. Test data are internally acquired at a rate of 400 kHz and transmitted to the computer at a frequency of 500 Hz.

Five samples were extracted from the Edwards 9350BC23 balloon catheter using a manually operated die-cutter. The specimens were characterised by a dumbbell-shaped geometry with a test length of 20 mm and a test width of 4 mm, according to BS ISO 37:2005 (Fig.3.8). The thickness of each single specimen was measured by means of a micrometer with a resolution of 0.001 mm. Three samples were cut along the circumferential direction of the balloon, while two were cut along the longitudinal direction.
During the tests each specimen was pulled to its breaking point at a constant speed of the crosshead of 5 mm/min. Stress and strain values were calculated from force and displacement

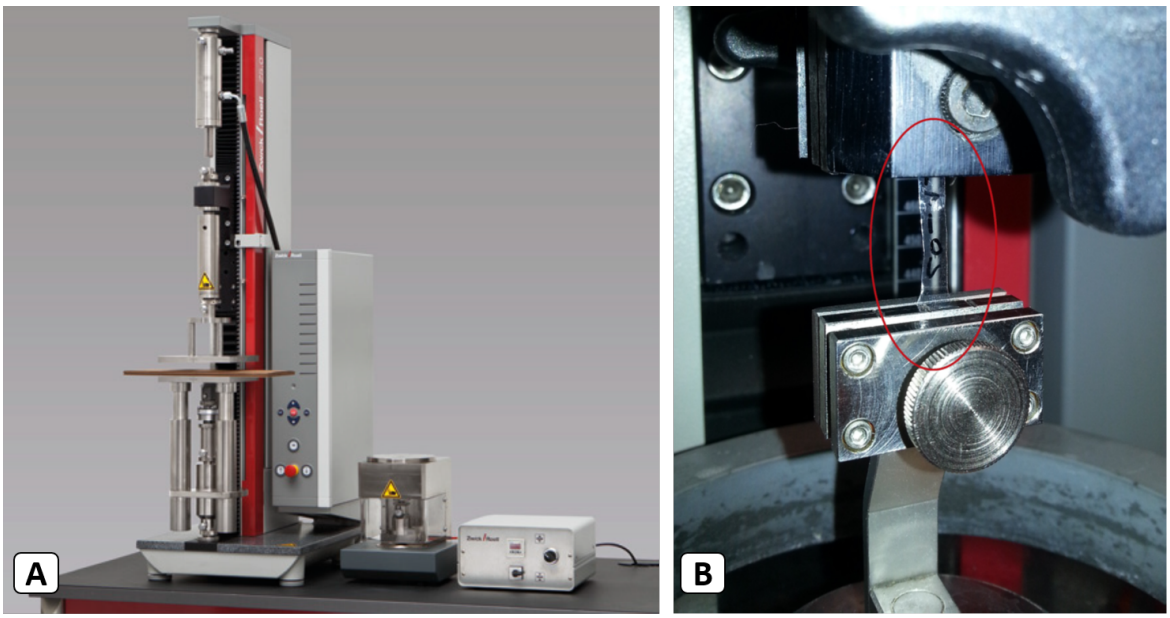

Fig. 3.7 a) The Zwick Roell Z5.0 tensile machine used for the tensile tests on the balloons. b) A dumbbell-shaped sample during the experiment [52].

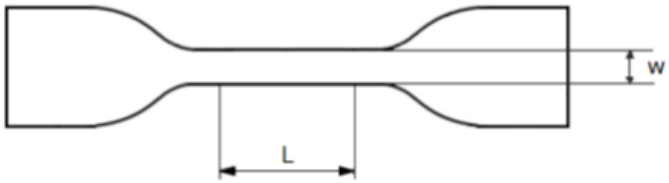

Fig. 3.8 Shape and dimensions of dumb-bell specimen. The test length L was 20 mm, while the test width w was 4 mm. [52].

data according to the following definitions:

$$\sigma = \frac{F}{t \cdot w} \tag{3.1}$$

$$\varepsilon = \frac{\Delta L}{L_0} \tag{3.2}$$

where F is the measured traction force, ΔL is the measured distance between the two grippers holding the sample, while t, w and L_0 are respectively the initial thickness, the initial test width and the initial test length of the specimen.

In this work, the stress-strain curve depicted in Fig. 3.9 was considered for the material. The curve, which suggests an hyperelastic behaviour, was defined by averaging data obtained from the tests on the three specimens cut along the circumferential direction.

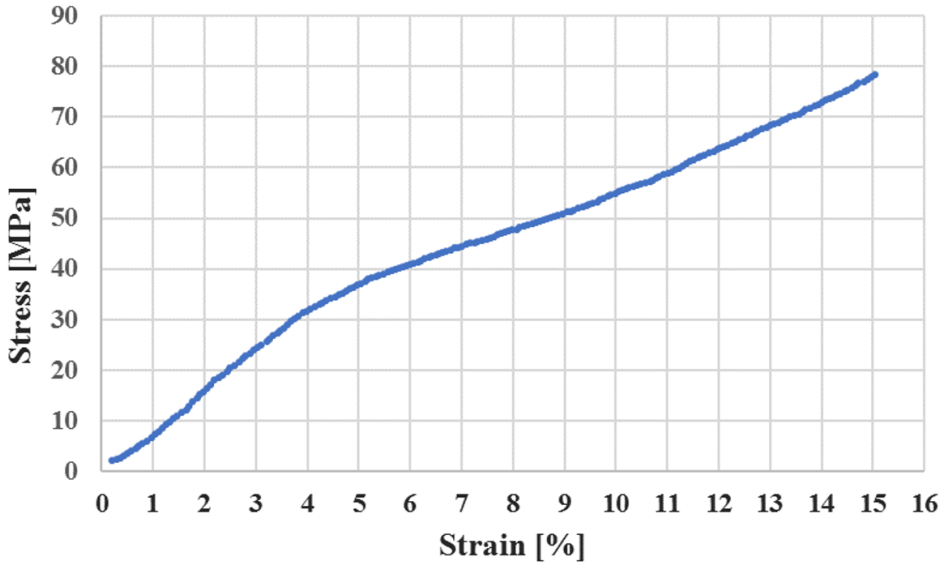

Fig. 3.9 Average stress-strain curve obtained from the tests on three specimens cut along the circumferential direction of the balloon.

For relatively large deformations, specimens cut along the circumferential direction exhibited a different behaviour, compared to the ones cut along the longitudinal direction. Nevertheless, the discrepancies at low strains were negligible, allowing to consider the assumption of isotropy valid within the standard operating range of the BAV balloon catheter (maximum strain $< 15\%$).
A Poisson's ratio of 0.45 was selected based on tensile test data reported in the literature [36].

3.2.2 Balloon Analytical Model

The sizing algorithm, described in detail in Section 3.3, requires a mathematical formulation that relates intra-balloon pressure and volume to the balloon diameter during free inflation. The first model was implemented analytically by approximating the balloon catheter as a pressurised cylindrical thin-walled vessel with hemispherical ends, as shown in Figure 3.10. The thin-walled vessel assumption is accurate for ratios of thickness to inside diameter less than $1/20$. Under these conditions, radial stress is negligible, and hoop and longitudinal stresses can be approximated as equally distributed across the wall thickness. Therefore, the hoop stress σ_{Hc} and the longitudinal stress σ_{Lc} for the thin-walled cylindrical portion can be expressed as:

$$\sigma_{Hc} = \frac{(p - p_e)D}{2t_c} \tag{3.3}$$

$$\sigma_{Lc} = \frac{(p - p_e)D}{4t_c} \tag{3.4}$$

where p is the intra-balloon absolute pressure, p_e is the external pressure, D is the unstretched diameter and t_c is the thickness of the cylindrical walls. Assuming a linear elastic constitutive

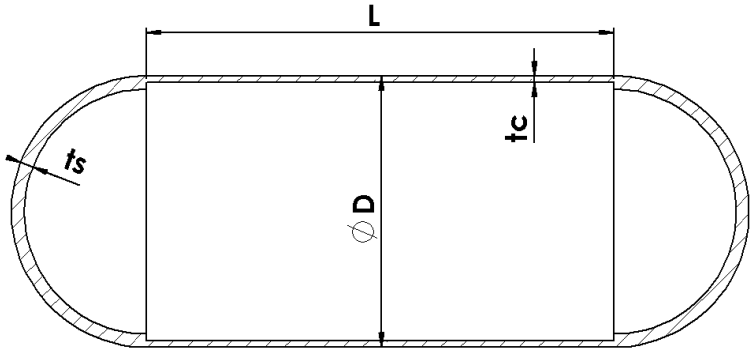

Fig. 3.10 The balloon catheter was modelled as a cylindrical thin-walled vessel with hemispherical ends.

behaviour, the hoop strain ε_{Hc} and the longitudinal strain ε_{Lc} can be written as:

$$\varepsilon_{Hc} = \frac{1}{E}(\sigma_{Hc} - \nu\sigma_{Lc}) \tag{3.5}$$

$$\varepsilon_{Lc} = \frac{1}{E}(\sigma_{Lc} - \nu\sigma_{Hc}) \tag{3.6}$$

where E is the Young's modulus and ν the Poisson's ratio. By combining the previous equations, the volumetric strain of the cylindrical portion of the balloon can be obtained:

$$\varepsilon_c = \varepsilon_{Lc} + 2\varepsilon_{Hc} = \frac{(p - p_e)D}{4t_c E}(5 - 4\nu) \tag{3.7}$$

The same reasoning can be applied to the two hemispherical ends. Together they form a thin-walled sphere, characterised by hoop stress σ_{Hs} and strain ε_{Hs}:

$$\sigma_{Hs} = \frac{(p - p_e)D}{4t_s} \tag{3.8}$$

$$\varepsilon_{Hs} = \frac{1}{E}(\sigma_{Hs} - \nu\sigma_{Hs}) \tag{3.9}$$

where t_s is the thickness of the hemispherical portions. The volumetric strain of the sphere made of the two hemispherical ends is:

$$\varepsilon_s = 3\varepsilon_{Hs} = \frac{3(p - p_e)D}{4t_s E}(1 - \nu) \tag{3.10}$$

Considering constant external atmospheric pressure, Equations 3.7 and 3.10 can be combined to define a general analytical relation between the instantaneous balloon volume and the intra-balloon absolute pressure valid during free inflation:

$$V(p) = \frac{\pi L D^2}{4}\left[1 + \frac{(p - p_e)D}{4t_c E}(5 - 4\nu)\right] + \frac{\pi D^3}{6}\left[1 + \frac{3(p - p_e)D}{4t_s E}(1 - \nu)\right] + c \tag{3.11}$$

In Equation 3.11, L is the unstretched length of the cylindrical region and c is a constant accounting for the presence of the guide wire pipe and potential residual saline solution inside the balloon cavity. To fully characterise the mathematical model, the parameters D, L, E, ν, t_c, t_s and c need to be determined.

Since the geometric specifications provided by the manufacturer refer to the balloon in its pressurised configuration when the material is stretched, the 3D unstretched non-collapsed geometry was reconstructed to obtain D and L. The catheter was connected to an open tank by means of a 3-way stopcock valve. Water was filled into the container until a distance

of approximately 2 cm between the free surface of the fluid and the cylindrical surface of the balloon was reached. In such circumstances, the intra-balloon transmural pressure is approximately $200-400$ Pa and the associated deformations are considered negligible. The stopcock valve was then closed. The device and the valve were disconnected from the reservoir and positioned in a polariscope, next to a millimetric reference scale. A high-resolution picture was taken and subsequently imported into Solidworks. By resizing the image according to the reference scale, the outer geometry of the balloon was reconstructed by firstly drawing half of the contour line on top of it, as shown in Fig. 3.11. Secondly, the partial contour line was revolved around the longitudinal axis of the balloon to create a 3D surface geometry. The position of the longitudinal axis was iteratively adjusted to guarantee a good overlap between the 3D surface and the balloon 2D contour on the image plane. Based on measurements on the reconstructed part, D was set to 20.75 mm and L to 35.82 mm.
To calculate E, data obtained from the tensile tests described in Section 3.2.1 were imported into Matlab (MathWorks, Natick, MA, US) and fitted with a linear regression model. As depicted in Fig. 3.12, only data within a strain range of 0-15% were taken into account for the analysis. The resulting optimal fit, obtained for $E = 556$ MPa, is characterised by a root-mean-square error $RMSE = 5.37$ MPa and a coefficient of determination $R^2 = 0.93$,

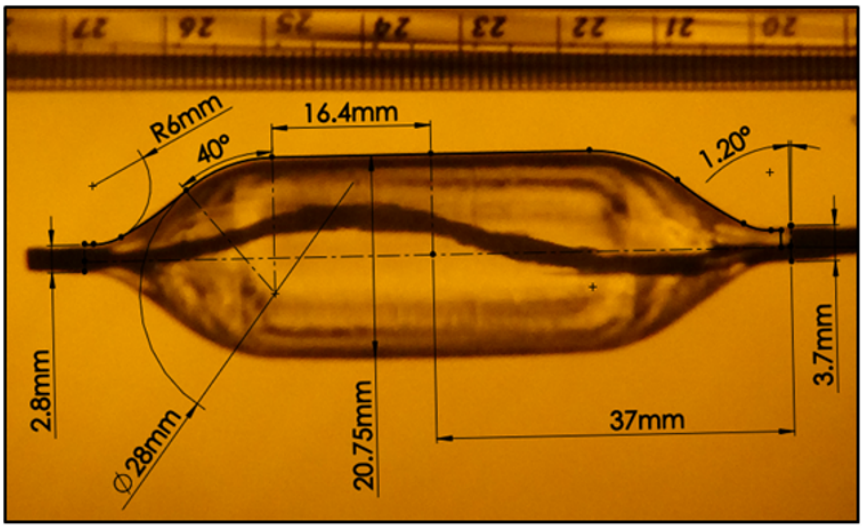

Fig. 3.11 Reconstruction of the balloon unstretched non-collapsed geometry from a polariscopic image in Solidworks.

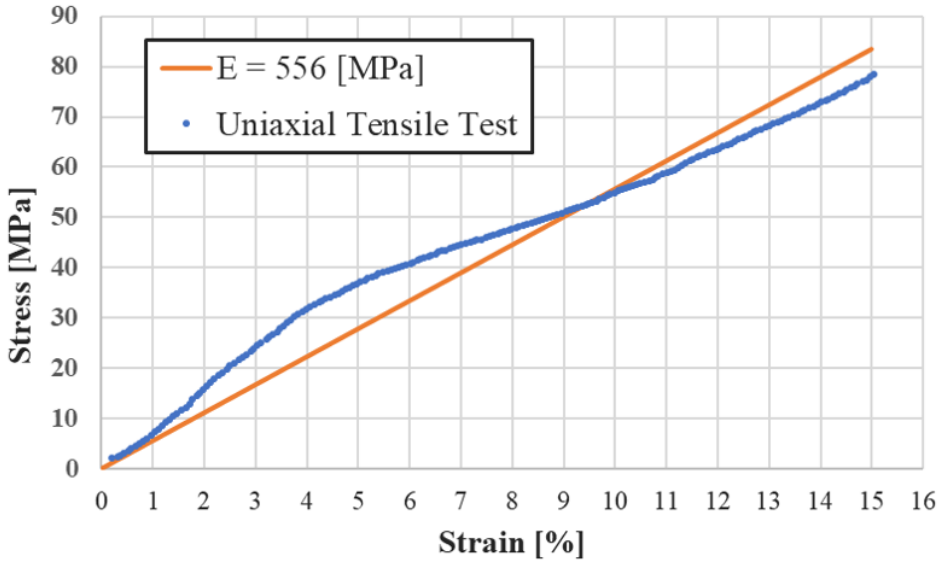

Fig. 3.12 Linear regression performed on the material characteristic stress-strain curve to calculate the Young's modulus.

respectively calculated as:

$$RMSE = \sqrt{\frac{\sum_{i=1}^{N}[f(x_i)-y_i]^2}{N}} \; ; \; R^2 = \frac{\sum_{i=1}^{N}[f(x_i)-\bar{y}]}{\sum_{i=1}^{N}[y_i-f(x_i)]^2} \tag{3.12}$$

where (x_i, y_i) are the coordinates of the data points, N is the number of data points, $\bar{y}$ is the average of the y-coordinates of the data points and f is the fitted function.
As anticipated in the previous subsection, the value of the Poisson's ratio $\nu = 0.45$ was taken from the literature [36]. The thickness t_c was retrieved from the analytical expression of the stretched diameter of the balloon cylindrical portion D_s as a function of the transmural pressure:

$$D_s(p) = D + \frac{(p-p_e)D^2}{4t_cE}(2-\nu) \tag{3.13}$$

By imposing a value of D_s equal to 23 mm for a transmural pressure of 4 atm, as per device specifications, Equation 3.13 can be solved for t_c (in this case, $t_c = 0.05$ mm). The remaining unknowns t_s and c need to be calibrated for each of the two platforms. The calibration procedure can be summarised as follows:

1. Experimental free inflation data are acquired with the robotised inflation device of choice. The balloon is inflated to its maximum operating pressure and deflated for

five times. A one minute wait between each run allows to minimise the impact of viscoelastic effects on the acquired pressure-volume (p-v) data;

2. p-v data from the tests are imported into Matlab and averaged to generate a characteristic p-v curve. The curve is smoothened using a robust local regression (loess) filter;

3. The critical point at which the balloon starts stretching is identified within the dataset as the maximum of the numerical second derivative of the pressure with respect to the volume. The portion of the curve where the material is tensioned is extracted accordingly (Fig. 3.13).

4. Nonlinear least-squares data fitting is performed to fit analytical expression of the volume (Equation 3.11) to the extracted dataset (Fig. 3.14). Since t_s and c are the only degrees of freedom of the function $V(p)$, they are calculated as a result of the fitting;

For the first robotic inflation device, the optimal fit characterised by $RMSE = 0.055$ ml and $R^2 = 0.99$ was achieved for $t_s = 0.05$ mm and $c = 1.66$ ml. For the second prototype, the best fit characterised by $RMSE = 0.010$ ml and $R^2 = 0.98$ was obtained for $t_s = 0.05$ mm and $c = -3.8$ ml.

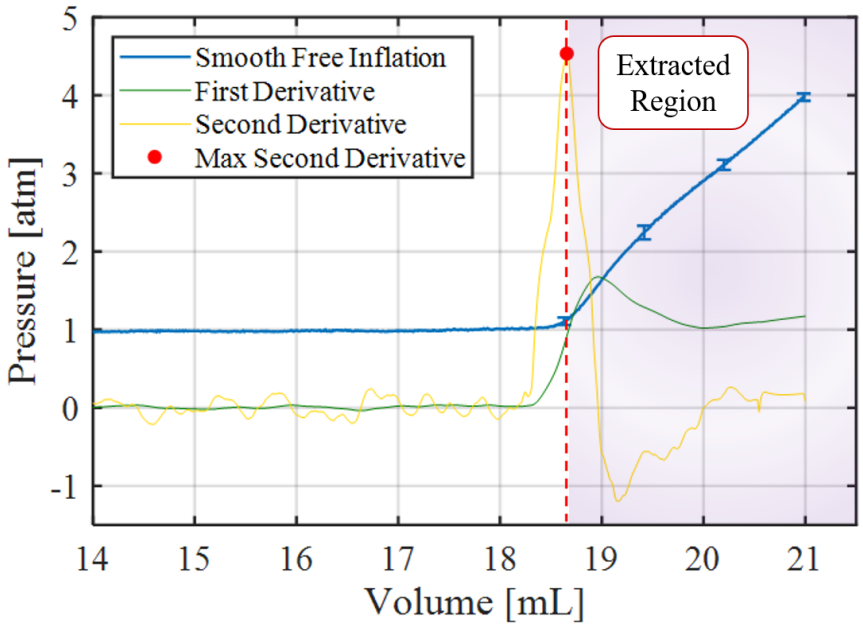

Fig. 3.13 Extracting the portion of the balloon characteristic free inflation curve where the material is tensioned. Data on the graph were acquired with the first robotic inflation device.

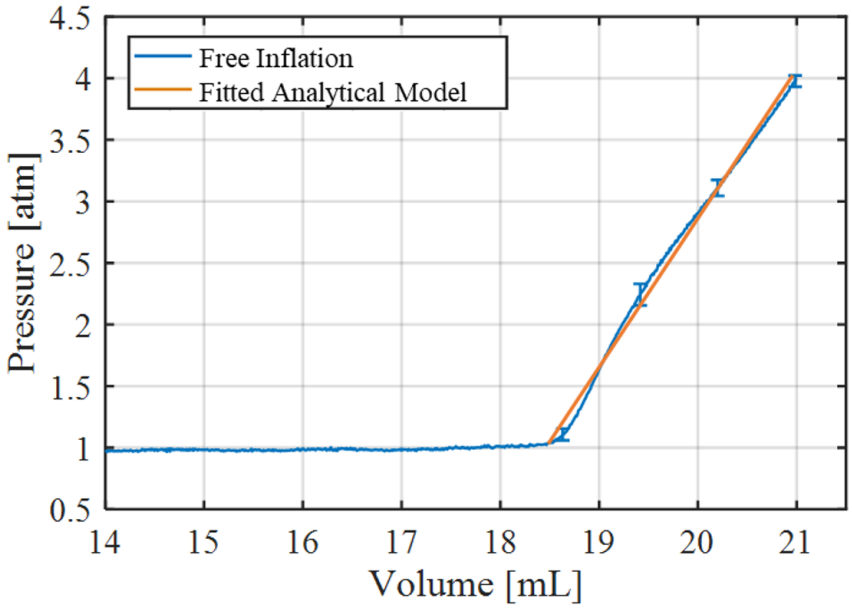

Fig. 3.14 Fitting the analytical model to the extracted portion of the balloon characteristic free inflation p-v curve. Data on the graph were acquired with the first robotic inflation device.

3.2.3 Balloon Numerical Model

The analytical model of the balloon free inflation, described in the previous subsection, is characterised by the following approximations:

1. Radial stresses are neglected, due to the thin-walled vessel assumption;
2. The material is linear elastic;
3. For the calculation of the stretched diameter D_s (Equation 3.13), the cylindrical portion of the balloon alone is considered. Potential distortions introduced by the two hemispherical ends are ignored;
4. The thickness of the hemispherical ends is uniform. Its value is not based on measurements on the actual device, rather it is estimated from experimental p-v data;

To investigate whether the sizing strategy proposed in this work would benefit from a more accurate description of the mechanics of the balloon free inflation, an alternative numerical model was developed.
The solid 3D model of the balloon was built by simply adding thicknesses to the 3D surface reconstructed for the analytical model. The thicknesses were manually determined by performing measurements with a micrometer on five stripes, obtained by cutting the actual

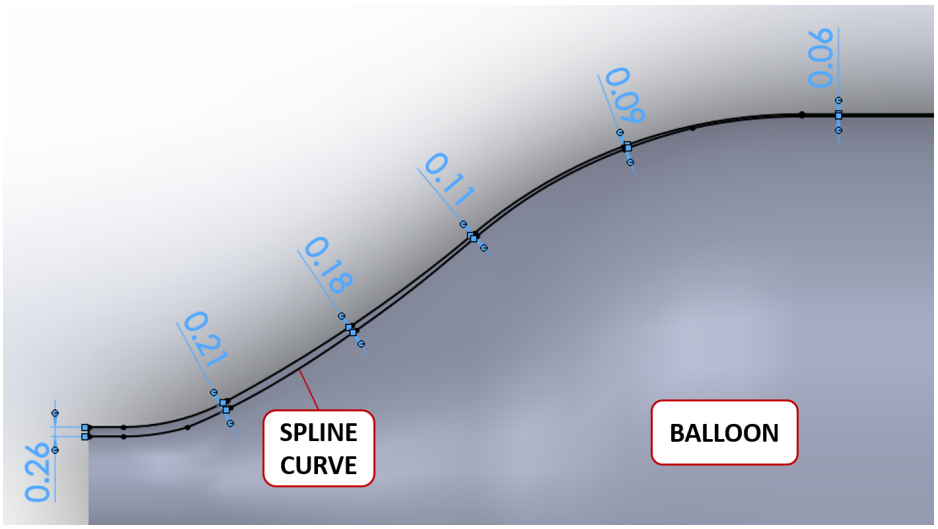

Fig. 3.15 Modelling the variable thickness of the hemispherical region using a spline curve to define the inner geometry. The displayed values are in millimetres.

device along the circumference. In agreement with the injection blow molding manufacturing process of the balloon, the wall thickness was found to decrease longitudinally from 0.26 mm at the extremity to 0.06 mm in the cylindrical region, where it remains approximately constant. The variable thickness of the hemispherical regions was modelled in Solidworks using a spline curve to define the inner geometry, as shown in Fig. 3.15.

Considering the symmetrical nature of the investigated problem, finite element (FE) analysis can be performed on just a portion of the model, to save computational resources. Therefore, a 120° sector of the balloon was split into two, using the plane of symmetry perpendicular to the longitudinal axis, to create the final 3D model. This is the smallest portion still capable of achieving the trifolded balloon configuration described in [90].

All simulations were performed with the FE software MSC Marc (MSC Software Corporation, Santa Ana, California, USA), choosing the implicit method and assuming large deformations. Abaqus (Dassault Systèmes Simulia Corp., Johnston, Rhode Island, US) was used to mesh the part. The model was discretised with 8-node hexahedral solid elements (13824, after sensitivity analysis), as illustrated in Fig. 3.16.

The liquid filled cavity feature integrated in MSC Marc was utilised to retrieve intra-balloon volume data, given a pressure load. Under the assumption that the cavity is completely filled with liquid, the volume is calculated as

$$V = \exp\left(\frac{\kappa ln(V_0) - p}{\kappa}\right) \tag{3.14}$$

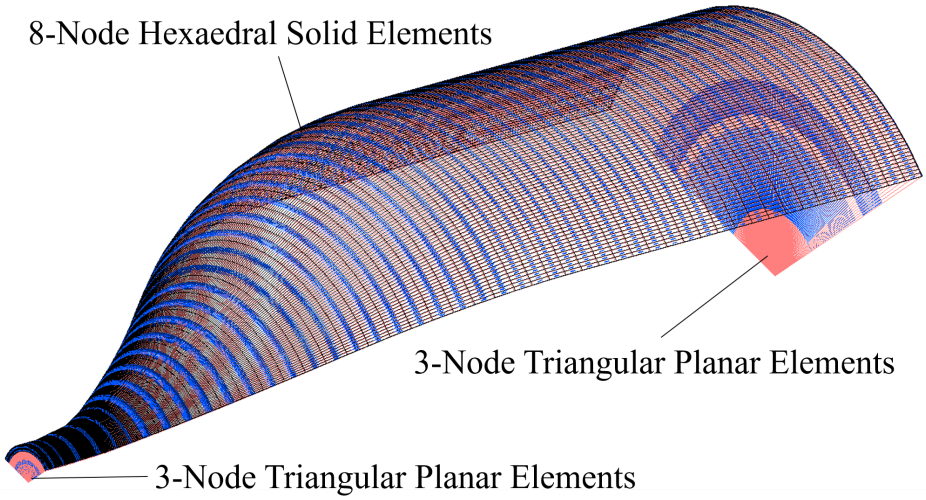

Fig. 3.16 The reconstructed 3D model was discretised using 8-node hexahedral solid elements for the body and 3-node triangular planar elements to delimit the fluid cavity.

where V_0 is the initial volume, p is the pressure and κ is the Bulk modulus. The Bulk modulus of water (2150 MPa) was adopted in the simulations. In addition to the inner surface of the FE model, two sets of 3-node triangular planar elements were positioned as shown in Fig. 3.16, to define the inspected cavity volume. Those elements do not contribute to the stiffness equations of the model. Since the cyclic symmetry option was configured to take into account the axisymmetry of the balloon, lateral boundaries were not required to identify the cavity volume.
The following boundary conditions were imposed for the nodal displacements:

- Nodes on the plane of symmetry perpendicular to the longitudinal axis were constrained in the longitudinal direction;
- Nodes on the two planes delimiting the 120° sector of the balloon were forced to move on those planes;
- Nodes on the plane perpendicular to the longitudinal axis and coincident with the extremity of the balloon could only move longitudinally;

Four different models for nearly incompressible elastomeric materials, Neo-Hookean, Yeoh, three term Mooney-Rivlin and Ogden, and a linear material model were defined in MSC Marc using data from the uniaxial tensile tests (see Sec. 3.2.1). For the linear model, the values of the Young's modulus ($E = 556$ MPa) and the Poisson's ratio ($\nu = 0.45$) were inferred as described in Sec 3.2.2. The parameters of the other models were determined through the experimental data fit tool available in MSC Marc. Tensile test data were downsampled by a

factor of ten, from 800 to 80 stress-strain points, for the analysis. The strain energy density function W of each model, expressed as a function of the principal strain invariants I_1, I_2 and I_3, as well as the model parameters and the relative least squares error e_r calculated through the fitting, are listed below:

- **Neo-Hookean:** $W = C_{10}(I_1 - 3)$ with $C_{10} = 107.908$ and $e_r = 1.007$;
- **Yeoh:** $W = C_{10}(I_1 - 3) + C_{20}(I_1 - 3)^2 + C_{30}(I_1 - 3)^3$ with $C_{10} = 103.833$, $C_{20} = 0$, $C_{30} = 479.854$ and $e_r = 1.444$;
- **Three term Mooney-Rivlin:** $W = C_{10}(I_1 - 3) + C_{01}(I_2 - 3) + C_{11}(I_1 - 3)(I_2 - 3)$ with $C_{10} = 78.188$, $C_{01} = 33.189$, $C_{11} = 0$ and $e_r = 0.841$;
- **Ogden:** $W = \sum_{n=1}^{N} \frac{\mu_n}{\alpha_n} \left(\bar{\lambda}_1^{\alpha_n} + \bar{\lambda}_2^{\alpha_n} + \bar{\lambda}_3^{\alpha_n} - 3 \right)$ where $N = 3$, $\mu_1 = 16943.3$ MPa, $\mu_2 = 4752.82$ MPa, $\mu_3 = 4529.82$ MPa, $\alpha_1 = 0.018$, $\alpha_2 = 0.018$, $\alpha_3 = 0.016$ and $e_r = 0.710$. $\bar{\lambda}_1$, $\bar{\lambda}_2$ and $\bar{\lambda}_3$ are the deviatoric stretch ratios;

For each material model a structural static simulation was run. The simulation starts with the balloon in its non-collapsed relaxed configuration and intra-balloon transmural pressure equal to zero. Then, the transmural pressure is linearly increased for 3 seconds (400 steps), until a value of 4 atm is reached. At the end of the simulation, p-v data and balloon diameter associated with each step are extracted. The balloon diameter is retrieved by tracking the radial displacement of a node located on the outer surface of the cylindrical portion and lying on the plane of symmetry perpendicular to the longitudinal axis.

The five numerical p-v datasets were imported into Matlab and fitted with a second degree polynomial, expressing the transmural pressure as a function of the volume:

$$p(v) = av^2 + bv + c \tag{3.15}$$

The resulting values of the coefficients and the fitting errors are included in Tab. 3.7. Subsequently, an additional parameter d was added to Equation 3.15, to make the function capable of shifting along the x-axis:

$$p(v) = a(v + d)^2 + b(v + d) + c \tag{3.16}$$

Mathematically speaking Equation 3.16 is equivalent to the inverse of the function in Equation 3.11 (see Sec. 3.2.2). The main difference is that the former is based on numerical data, while the latter is derived analytically, considering the approximations listed at the beginning

Material Model	a	b	c	R^2	Root-Mean-Square Error
Linear	-0.093	4.549	-50.110	1	0.005 atm
Neo-Hookean	-0.127	6.056	-65.880	1	0.002 atm
Yeoh	-0.107	5.296	-58.72	1	0.006 atm
Three term Mooney-Rivlin	-0.127	6.123	-66.920	1	0.002 atm
Ogden	-0.134	6.390	-69.620	1	0.002 atm

Table 3.7 Coefficients of the second degree polynomial used to fit the numerical free inflation p-v datasets, associated with the analysed material models, and resulting fitting errors.

of this section.

The same procedure described in Sec. 3.2.2 to calibrate the parameters t_s and c of Equation 3.11 for the two platforms, was employed to calculate d for all the model-specific $p(v)$ functions and finally pick the material model to be used in our sizing algorithm. The values of d obtained for the two platforms and the associated fitting errors are reported in Tab. 3.8. The model-specific $p(v)$ functions fitted to the average free inflation p-v curve, obtained using the first prototype of the robotic inflation device, are depicted in Fig. 3.17. According to the results of the analysis, in the case of both robotic inflation devices the linear material model is the one that allows Equation 3.16 to better approximate experimental data. Therefore, it was selected for the sizing algorithm. This result is mainly caused by the impact of the inherent compliance of the platforms on acquired p-v data. The components of the inflation devices are not perfectly rigid. Hence, when the system is pressurised, their deformation adds up to the volumetric expansion of the balloon. Having said that, it is important to highlight that the linear model does not describe the mechanics of the actual balloon more accurately than the other models. It simply allows to better incorporate the contributions of all deformable components that where not formally included in the analysis.

Material Model	d_1	R_1^2	$RMSE_1$	d_2	R_2^2	$RMSE_2$
Linear	-1.743	0.998	0.037 atm	3.746	0.990	0.094 atm
Neo-Hookean	-1.990	0.921	0.232 atm	3.421	0.945	0.218 atm
Yeoh	-1.955	0.946	0.1925 atm	3.464	0.960	0.184 atm
Three term Mooney-Rivlin	-2.025	0.887	0.277 atm	3.375	0.916	0.269 atm
Ogden	-2.049	0.859	0.310 atm	3.343	0.892	0.306 atm

Table 3.8 Model-specific values of the constant d, obtained for the two platforms, and associated fitting errors. The values associated with the first platform are denoted by subscript 1, while the ones associated with the second platform are denoted by subscript 2.

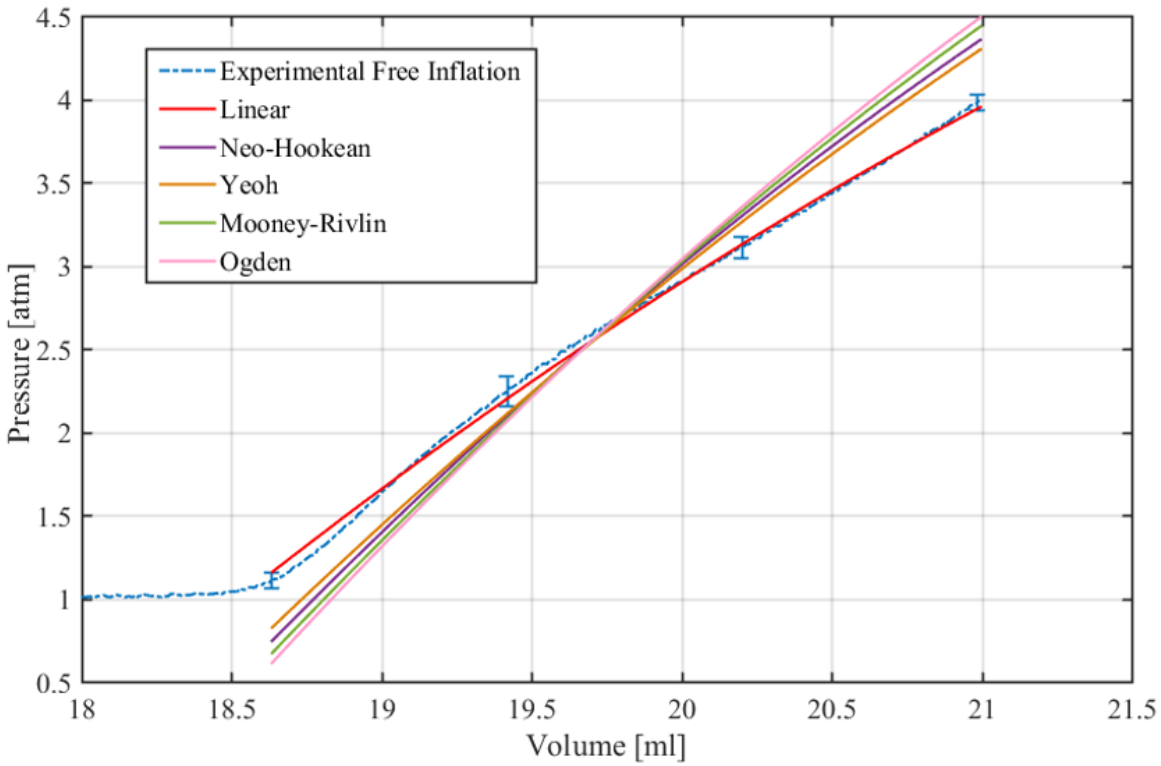

Fig. 3.17 Model-specific $p(v)$ functions fitted to the average free inflation p-v curve retrieved from data acquired with the first platform.

The mathematical equation expressing the balloon diameter as a function of the transmural pressure for the linear material model was determined by fitting numerical diameter and pressure data, extracted from the simulation, with a second degree polynomial:

$$D(p) = 0.0528p^2 + 0.474p + 20.75 \tag{3.17}$$

The resulting optimal fit is characterised by $RMSE = 0.0085$ mm and $R^2 = 1$. Equation 3.17 is equivalent to Equation 3.13, defined for the analytical model.
In the next section, the logic of the sizing algorithm will be presented and the crucial role played by the two mathematical models of the balloon free inflation will be clarified.

3.3 The Sizing Algorithm

The sizing algorithm presented in this section was entirely developed in Matlab. In all sizing experiments data were first acquired using the robotic inflation devices and then processed offline to extract the annular diameter.
The proposed approach is built upon the assumption that the diameter of the balloon, measured

at the time when full contact with the annular walls is first attained, equals the annular diameter. Therefore, sizing can be performed indirectly by identifying the point within the acquired dataset, at which the *p-v* curve deviates from the free inflation curve, and estimating the corresponding balloon diameter. This is achieved by iteratively performing linear regression on the *p-v* dataset, as shown in Algorithm 2. In each iteration, the data point with the lowest volume value is removed, a line is fitted to the updated dataset and the associated RMSE is extracted. The process stops when the RMSE is smaller than an empirically set threshold (0.03 atm). Thus, the equation of a line, which approximates the portion of the processed *p-v* curve deviating from the free inflation curve, is obtained. The symbolic mathematical capabilities of Matlab can then be exploited to find the desired point as the intersection between the fitted line and the model p-v function. Depending on the model selected to describe the balloon free inflation, the p-v function can either be Equation 3.11 or Equation 3.16. Figure 3.18 illustrates the identification of the intersection point for two different annular diameters, using the analytical model of the balloon free inflation.
Once the intersection point is identified, its associated pressure is either fed to Equation 3.13 or Equation 3.17, again, based on the selected mathematical description of the balloon free

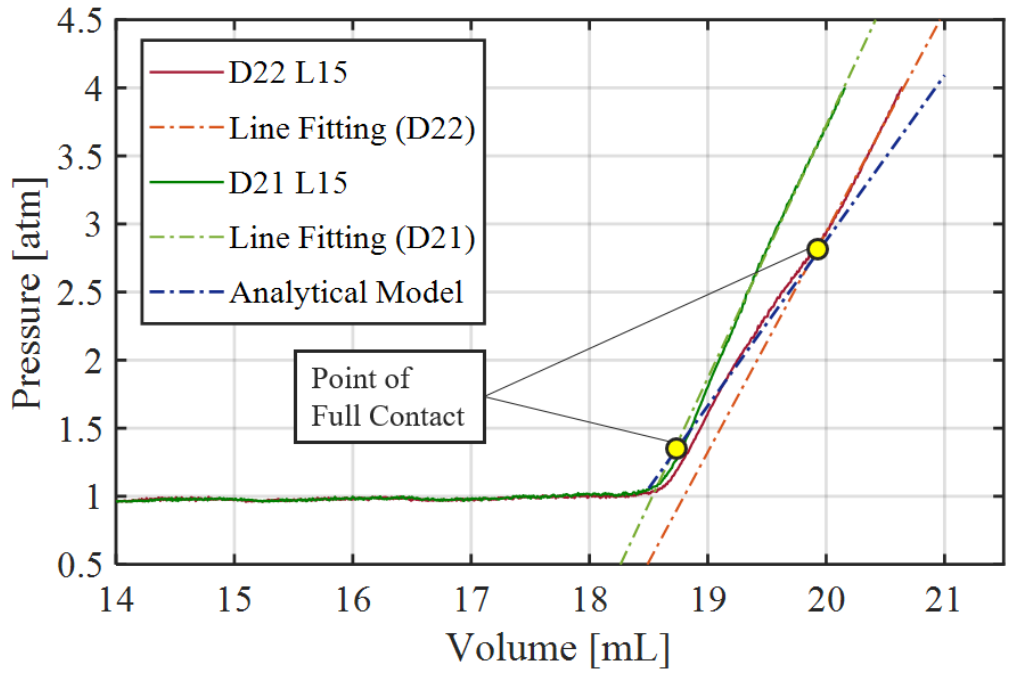

Fig. 3.18 Example of iterative linear regression performed on *p-v* curves obtained from experimental valvuloplasty on idealised annuli with diameters of 22 and 21 mm (and 15 mm length). The point of full contact is where the *p-v* curve deviates from the free inflation curve, as a result of the balloon-annulus contact.

inflation. Finally the annular diameter is determined.
The overall sizing strategy is summarised in the following pseudo code (Algorithm 2).

Algorithm 2: Implementation of the sizing algorithm

input : Experimental p [atm] - v [ml] Data
output : Annular Diameter
Fit p-v Data with a Line;
Extract Root-Mean-Square Error (RMSE);
while *(RMSE>setRMSE)* **do**
    `// setRMSE empirically set to 0.03 atm`
    Delete First p-v Data Point (Lowest Volume);
    Fit Updated p-v Dataset with a Line;
    Extract RMSE;
end
if *Analytical Model* **then**
    Solve the system $\begin{cases} Fitted\ Line\ Equation \\ Analytical\ Model\ V(p)\ Function\ (Equation\ 3.11) \end{cases}$ for p;
    Substitute p in Equation (3.13);
    return Annular Diameter;
else
    Solve the system $\begin{cases} Fitted\ Line\ Equation \\ Numerical\ Model\ p(v)\ Function\ (Equation\ 3.16) \end{cases}$ for p;
    Substitute p in Equation (3.17);
    return Annular Diameter;
end

3.4 The Annular Phantoms

The proposed approach was validated *in vitro* on two sets of aortic annular phantoms that were designed approximating the implantation site as a cylinder.
The first set is composed of six rigid cylinders machined in four 5 mm-thick acrylic plates specifying a diametral dimensional tolerance of ± 0.1 mm. The plates could be stacked, as shown in Fig. 3.19, to obtain the lengths of 15 mm and 20 mm delimiting reported annular length variability in adult human aortic valves [15]. Good alignment between the plates is guaranteed by means of two centering pins. The diameters were selected to take into account typical (21, 22 and 23 mm) and extremely aggressive (18, 19 and 20 mm) balloon-annulus sizing ratios [33].
In vivo studies have shown that the annular perimeter of patients affected by severe AS undergoes negligible deformation over the cardiac cycle [51, 66]. Also, after prosthetic

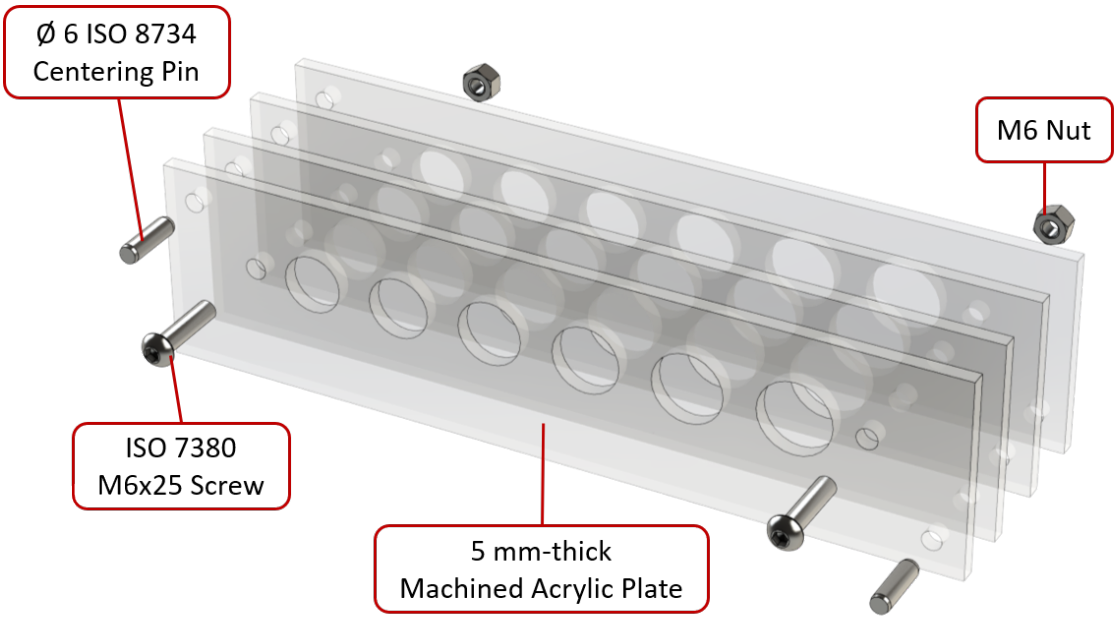

Fig. 3.19 Idealised rigid annular phantoms with diameters ranging from 18 mm to 23 mm.

valve implantation, significant changes in the annular diameter were not observed [91, 92], indicating substantial material stiffness. Hence, the rigidity assumption is considered valid for severe forms of the disease.

The second set of annular phantoms is composed of eight 3D printed compliant cylinders. The set can be further divided into two subgroups of four cylinders (Fig. 3.20), based on the inner diameter that is either 21 or 22 mm. Only two diameters where taken into account for reasons that will be clarified in the next chapter. Except for the inner diameter, all phantoms share the same geometry characterised by a constant thickness of 5 mm and a length of 40 mm. The reason why the compliant phantoms are longer than the rigid ones is that they were designed to both represent milder forms of AS and explore the applicability of the

Fig. 3.20 The set of idealised compliant phantoms 3D printed with PolyJet technology.

proposed technique in the more general context of vessel sizing.
The phantoms were 3D printed using an Objet500 Connex (Stratasys Inc., Rehovot, Israel) that exploits PolyJet technology. Such technology not only guarantees an accuracy down to 0.014 mm, but it also allows to mix two different curable liquid photopolymers in order to adjust the compliance of the final product. Tango Black Plus, which results in a soft rubber-like material after curing, and VeroClear, which on the contrary becomes stiff once cured, were combined using specific mix ratios to have phantoms with shore hardness 60A, 70A, 85A and 95A in both subgroups. Since typical values for the stiffness of the left ventricular outflow tract are not reported in the literature, the shore hardness values were selected considering the definition of vessel rigidity K provided in [36] and the associated range of values identified for the stenotic annulus. K is derived from the definition of vessel compliance included in ISO 5840:2015 and can be expressed as:

$$K = \frac{(p_2 - p_1)}{100(d_2 - d_1)} d_1 \tag{3.18}$$

where p_1 and d_1 are respectively the diastolic pressure and the corresponding diameter of the vessel, while p_2 and d_2 are the same values measured during systole. In [36] values of K up to approximately 400 kPa/% are considered plausible for stenotic annuli. To check whether the material-geometry combination of each phantom was consistent with the defined range of K, numerical analyses were carried out.
Firstly, the materials created by 3D printing the chosen mix ratios of Tango Black Plus and VeroClear needed to be mechanically characterised. Therefore, uniaxial tensile tests to failure where performed. Four 2 mm-thick sheets, one for each selected shore hardness, were 3D printed and five samples were extracted from each sheet by means of a manually operated die-cutter. The same machine and the same protocol described in Section 3.2.1 were employed for the tests. The obtained average stress-strain curves are depicted in Fig. 3.21. The curves associated with shore hardness 60A and 70A exhibit an hyperelastic behaviour. On the other hand, the other two, which are associated with higher percentages of VeroClear, have a different shape and they appear almost linear for very low values of strain.
Secondly, the two cylindrical models used to 3D print the phantoms were prepared for the simulations. A 120° sector was taken from each cylinder and split into two, using the plane of symmetry perpendicular to the longitudinal axis. The resulting 3D models were imported into Abaqus and discretised with 2520 8-node hexahedral solid elements. Then, the files with the meshed bodies were imported into MSC Marc. Similarly to what was done for the numerical model of the balloon (Section 3.2.3), the integrated liquid filled cavity feature was adopted to determine the inner volume of the phantoms, given a pressure load. Also in this case, two

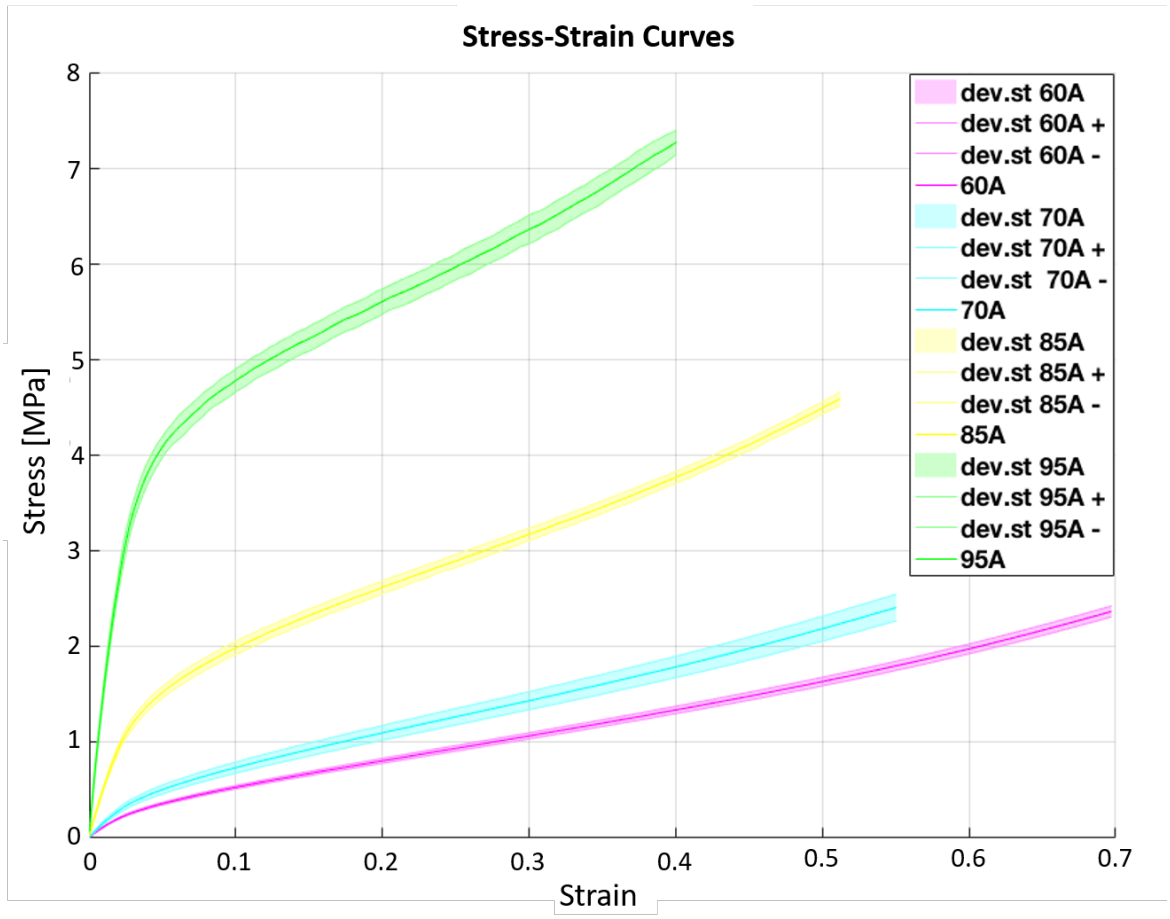

Fig. 3.21 Stress-strain curves of the four materials obtained by 3D printing different mix ratios of Tango Black Plus and VeroClear. The thickest lines in the graph, labelled with shore hardness values (60A, 70A, 85A, 95A), are the average stress-strain curves. The thin ones represent the standard deviation of the measured stresses as a function of strain.

sets of 3-node triangular planar elements, which do not contribute to the stiffness equations of the model, were positioned as shown in Fig. 3.22, to define the inspected cavity volume. Since the cyclic symmetry option was configured to take into account the axisymmetry of the phantom, lateral boundaries were not required to identify the cavity volume.
The following boundary conditions were imposed for the nodal displacements:

- Nodes on the plane of symmetry perpendicular to the longitudinal axis were constrained in the longitudinal direction;
- Nodes on the two planes delimiting the 120° sector of the cylinder were forced to move on those planes;

The experimental data fit tool available in MSC Marc was used to define the material properties of the hexahedral elements. The Ogden material model, whose strain energy

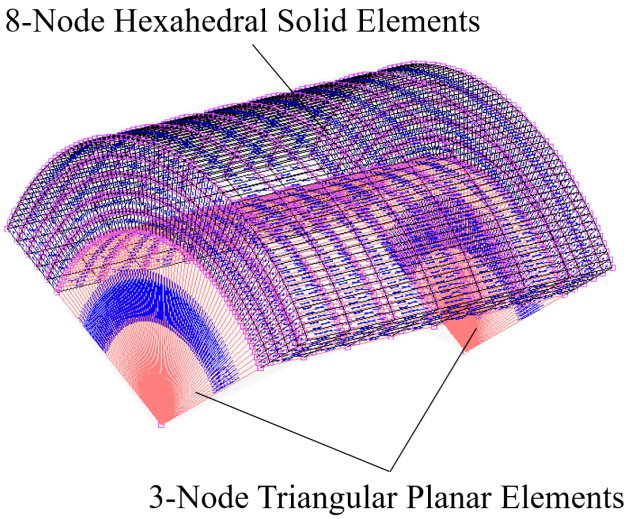

Fig. 3.22 Finite element model of the compliant phantom with inner diameter 21 mm, discretised using 8-node hexahedral solid elements for the body and 3-node triangular planar elements to delimit the fluid cavity.

density function W was introduced in Section 3.2.3, was used to fit stress-strain data from the uniaxial tensile tests. The resulting values of the coefficients and the fitting errors for each shore hardness are included in Tab 3.9. While the Ogden model fits experimental data well for shore 60A and 70A, it results in relatively high fitting errors for shore 85A and 95A. Due to that, two linear models were defined for the two stiffer materials, only taking into account the steep portion of the stress-strain curves at very low values of strain (0-0.05), as shown in Fig. 3.23. The values of the modulus of elasticity, calculated by performing linear regression in Matlab, are 35.81 MPa for the material with shore hardness 85A and 109.6 MPa for the one with shore hardness 95A. A Poisson's ratio of 0.45 was assumed for both.

For each geometry-material configuration in the set of compliant phantoms, a structural static simulation was run choosing the implicit method. The simulation starts with the phantom in its relaxed state and cavity pressure equal to zero. Then, the pressure is linearly

Shore Hardness	μ_1 [MPa]	μ_2 [MPa]	μ_3 [MPa]	α_1	α_2	α_3	e_r
60A	44.27	0.001	3.16	0.05	12.46	0.44	7.19
70A	156.30	7.01e-006	11.43	0.028	23.56	0.073	6.75
85A	921.27	163.22	651.83	0.007	0.007	0.006	15.19
95A	3905.68	595.57	943.848	0.004	0.005	0.005	21.26

Table 3.9 Coefficients of the strain energy density function W of the Ogden model for the 3D printed materials and resulting fitting errors.

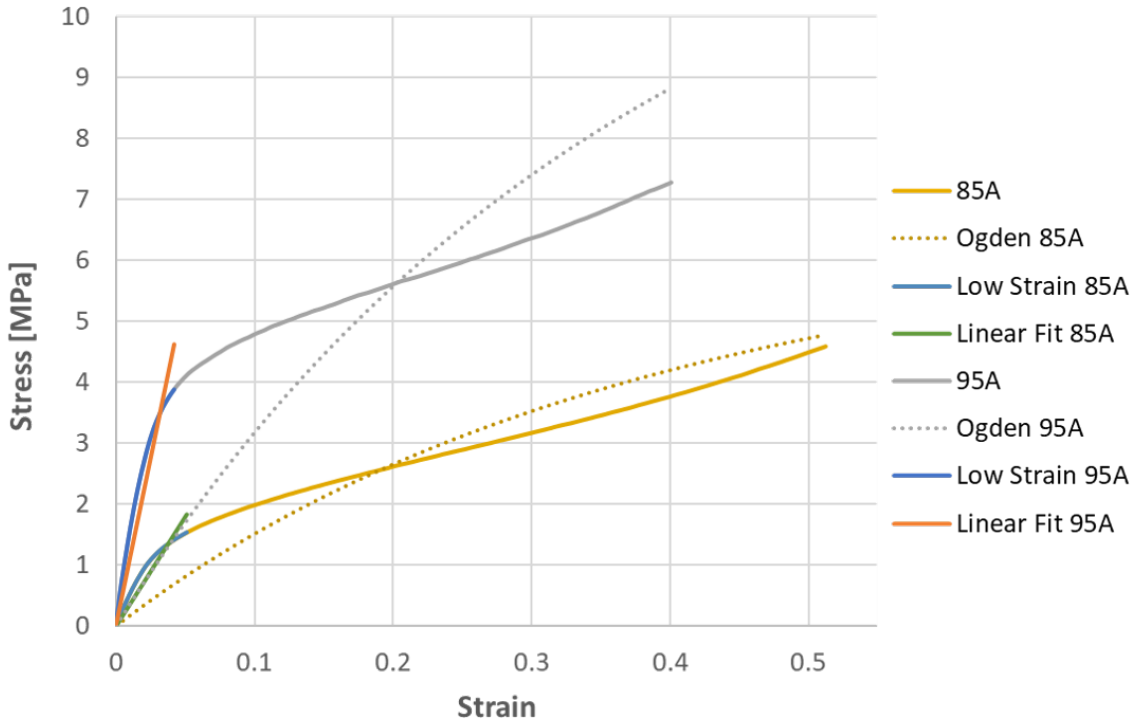

Fig. 3.23 The Ogden material model does not accurately describe the mechanical behaviour of the 3D printed materials with shore hardness 85A and 95A. Therefore, a linear model was adopted to characterise the behaviour of the materials at low strains.

increased for 3 seconds (400 steps), until a value of 40 mmHg (5.33 kPa) is reached. The selected pressure value is the difference between the arterial peak systolic pressure and the arterial diastolic pressure in a normotensive person. At the end of the simulation, the inner diameter of the phantom is calculated from the radial displacement of a node located on the inner surface. Based on that, the value of the rigidity K for the phantom can be estimated. The values of K retrieved for the whole set are included in Tab. 3.10. In conclusion, it can be deduced that all compliant phantoms fall in the rigidity range specified in [36] ($\leq$ 400 kPa/%).

Diameter [mm]	Shore 60A	Shore 70A	Shore 85A	Shore 95A
21	17.34 kPa/%	24.07 kPa/%	113.65 kPa/%	348.01 kPa/%
22	16.06 kPa/%	22.30 kPa/%	105.25 kPa/%	322.31 kPa/%

Table 3.10 Numerically estimated rigidity values of the compliant phantoms in kPa/%.

3.5 Summary

In this chapter, the two robotic inflation devices designed to extract intra-balloon p-v curves during TAVI were presented and compared in terms of hardware components, software architecture and performance. The BAV catheter used in this project was then introduced. In particular, the steps taken to develop two mathematical models with different levels of approximation, to characterise the mechanical behaviour of the balloon during free inflation, were outlined. Subsequently, the role played by the balloon mathematical models in the context of aortic annulus sizing was clarified and the core logic of the sizing algorithm was explained. Finally, the two sets of idealised annular phantoms manufactured to validate the proposed approach were described.
The next chapter includes the descriptions of all the experiments that have been carried out, together with discussions regarding the observed results.

Chapter 4

Experimental Protocols, Results and Discussion

In this chapter, the experiments performed to validate the proposed approach for sizing the aortic annulus are discussed. Section 4.1 includes the description of the sizing tests carried out on idealised rigid phantoms using the first prototype of the robotic inflation device. The sizing experiments conducted with the second prototype of the robotic inflation device on idealised rigid and compliant annular phantoms are reviewed in Section 4.2 and Section 4.3 respectively. The chapter concludes with the presentation of the additional tests executed to analyse the impact of injection speed on p-v data. The results observed in each set of experiments are discussed at the end of the corresponding section.

4.1 Sizing the Rigid Annular Phantoms with the First Prototype of the Inflation Device

As previously stated, the first prototype of the robotic inflation device, described in Section 3.1.1, was manufactured to perform a preliminary assessment of the basic idea upon which the project was based and highlight potential criticalities. That was done through the set of experiments presented in this section. The proposed sizing approach was tested on the rigid annular phantoms introduced in Section 3.4. The adopted experimental protocol can be divided into several steps, which are summarised below:

1. The first prototype of the robotic inflation device and the rigid phantoms were fixed on a 5 mm-thick steel plate, as shown in Fig. 4.1;

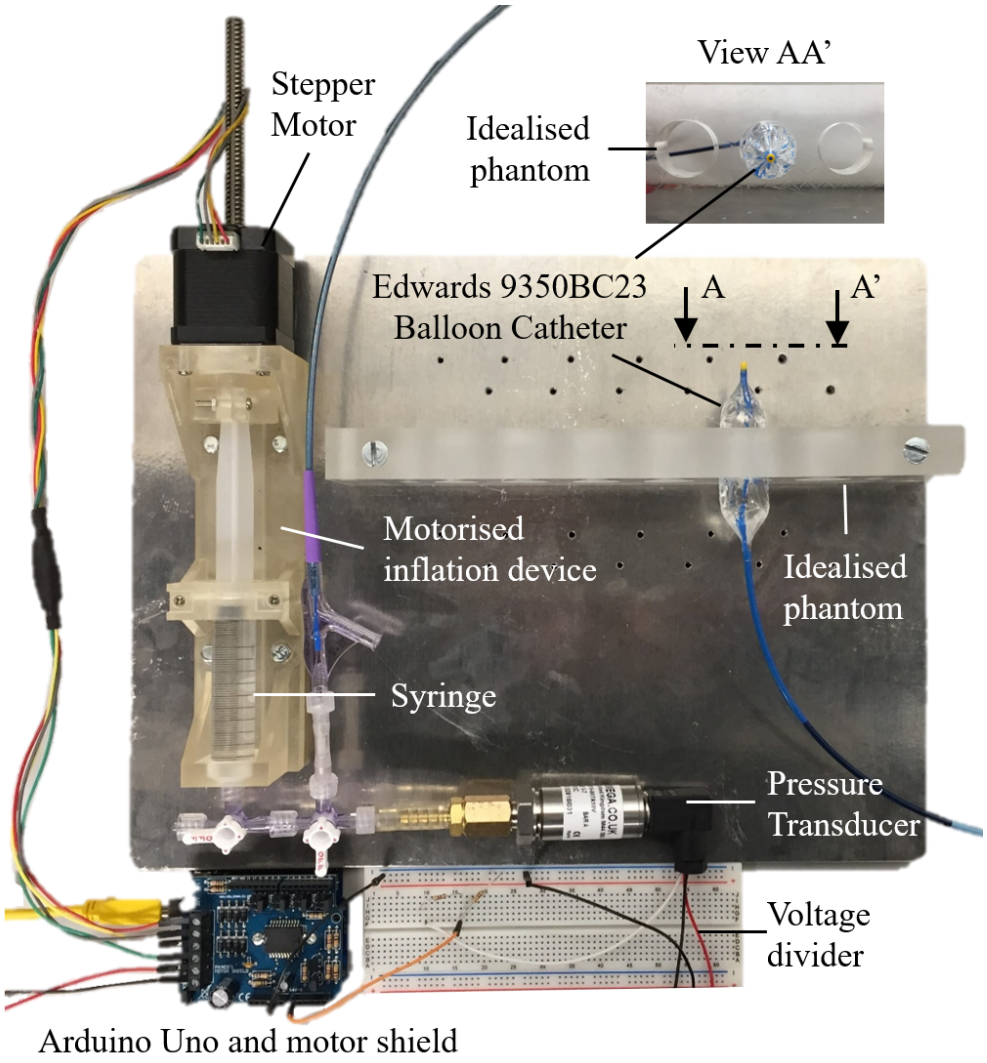

Fig. 4.1 Sizing the idealised rigid aortic annular phantoms with the first prototype of the robotic inflation device: Top view of the experimental setup and front view of the balloon catheter inside the idealised phantom.

2. The plunger of the robotic inflation device was moved all the way back inside the barrel. Subsequently, the hydraulic circuit connecting the robotic inflation device, the pressure transducer and the balloon catheter was filled with saline solution by means of a standard syringe connected to one of the two 3-way stopcock valves. The orientation of the platform was changed several times during the filling process in order to facilitate the removal of all visible air bubbles. At the end of the procedure, the circuit was closed and the additional syringe was removed, making sure to leave approximately 13 ml of fluid inside the balloon. This pre-inflation is required to enable the robotic inflation device to inject enough fluid to observe the transition from

non-stressed balloon material to stressed balloon material and maximum intra-balloon pressure;

3. Free inflation p-v data were acquired, according to the procedure described in Section 3.2.2, to calibrate the parameters of both the analytical (see Section 3.2.2) and the numerical (see Section 3.2.3) models of the balloon free inflation;

4. For each phantom configuration five p-v curves were extracted. Considering that six annular diameters (18, 19, 20, 21, 22 and 23 mm) and two annular lengths (15 and 20 mm) were taken into account, sixty tests were performed in total. During each run the balloon was placed inside the phantom and inflated to its maximum operating pressure at a flow rate of approximately $0.076\,\frac{\text{ml}}{\text{s}}$. No particular precautions were taken to enforce any axial positioning of the balloon. Since an homing function was not implemented on the first prototype of the robotic inflation device, the number of steps taken by the motor was used to send the plunger to its starting position at the end of each test. A one minute wait between each run was imposed to minimise the impact of viscoelastic effects on the acquired p-v data;

5. Acquired p-v data were imported into Matlab and processed offline using both versions of the sizing algorithm, the one based on the analytical model and the one based on the numerical model. The results of the processing will be presented and discussed in the next subsection, alongside additional observations about the acquired data.

4.1.1 Results and Discussion

A unique p-v curve, for each phantom configuration, was obtained by averaging the results of the five tests, as shown in Fig. 4.2. Despite the preliminary calculations performed to assess the suitability of the stepper motor (Appendix A.1), in practice the platform was not capable of inflating the balloon to its maximum operating pressure (absolute pressure of 5 atm). Due to that, Fig. 4.2 only includes p-v data associated with an absolute pressure less than or equal to 4 atm. Furthermore, data associated with the experiments on the 23 mm-diameter phantom are not depicted, as contact with the annular walls was not attained within this limited pressure range.

It can be observed from the graph that, for annular diameters bigger than or equal to the balloon unstretched diameter (≥ 20.75 mm), the full contact with the annular wall is immediately identifiable from the point at which the p-v curve deviates from the free inflation curve. The algorithm presented in Section 3.3 was developed based on this observation. The coordinates of this point are independent from the length of the phantom. The annular

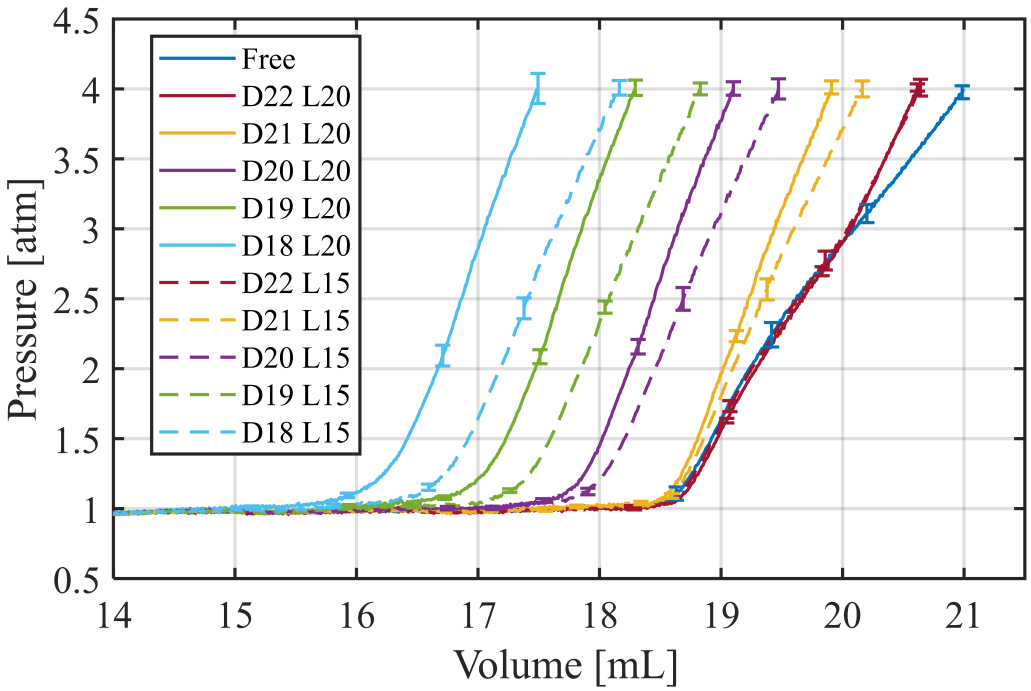

Fig. 4.2 Comparison between average absolute pressure-volume curves obtained by inflating the balloon inside idealised rigid phantoms with different diameters (D) and lengths (L), using the first prototype of the robotic inflation device.

length only affects the slope of the curve after full contact. More specifically, the longer the phantom, the steeper the portion of the curve that deviates from the free inflation curve is. For annular diameters smaller than 20.75 mm, the balloon reaches full contact with the annulus, while its membrane is not tensioned. Therefore, the departure from the free inflation curve is not directly associated with the annular diameter. Rather, it is caused by the balloon inability to deploy freely, which produces an anticipated tensioning of the balloon material. For these diameters, the point at which the balloon material starts tensioning depends significantly on the annular length. In these circumstances, it is impossible to obtain a direct and unbiased estimate of the annular diameter, from basic considerations on p-v data. This observation supports the decision to develop mathematical models of the free inflation, which do not describe the phase during which the balloon undergoes volumetric expansion at constant intra-balloon atmospheric pressure (collapsed non-tensioned state). On this basis, the sizing was only performed on phantoms with diameters larger than 20.75 mm (21 and 22 mm).

The results obtained by processing experimental p-v data with the sizing algorithm built upon the analytical model of the balloon free inflation are summarised in Tab. 4.1. The outputs of the sizing algorithm that exploits the numerical model are presented in Tab. 4.2. Overall, the

Phantom Diameter [mm]	Phantom Length [mm]	Avg. Meas. Diameter [mm]	Std. Dev. [mm]	Avg. Error [%]
22	20	22.002	$\pm$0.031	0.007
21	20	20.908	$\pm$0.051	0.438
22	15	22.204	$\pm$0.110	0.927
21	15	21.133	$\pm$0.101	0.632

Table 4.1 Nominal annular diameter vs average measured diameter (first prototype of the robotic inflation device) with standard deviation and average error for each phantom configuration. Experimental data were processed using the sizing algorithm based on the analytical model of the balloon free inflation.

experimental results clearly confirm that intra-balloon p-v data can be used to determine the annular diameter of idealised rigid phantoms with good precision. In the examined cases, the proposed approach exhibited good repeatability (maximum standard deviation $\pm$0.110 mm and $\pm$0.132 mm with the analytical and the numerical model, respectively) and high accuracy (maximum average error 0.927% and 1.460% with the analytical and the numerical model, respectively). The average error is calculated as in Equation 4.1.

$$\underset{Error}{Average} = \left| \frac{Average\ Measured\ \varnothing - Annular\ \varnothing}{Annular\ \varnothing} \right| \tag{4.1}$$

Although the analytical model of the balloon free inflation seems to be consistently associated with slightly more accurate results, the performances of both versions of the sizing algorithm are almost identical. This similarity makes sense considering that the two models were constructed starting from the same balloon geometry and utilising the same linear isotropic material model. Fig. 4.3 helps visualising how close the two models are in practice, when both versions of the sizing algorithm are used to process the same p-v dataset. On the other

Phantom Diameter [mm]	Phantom Length [mm]	Avg. Meas. Diameter [mm]	Std. Dev. [mm]	Avg. Error [%]
22	20	22.143	$\pm$ 0.027	0.651
21	20	20.863	$\pm$0.065	0.654
22	15	22.321	$\pm$0.085	1.460
21	15	21.153	$\pm$0.132	0.728

Table 4.2 Nominal annular diameter vs average measured diameter (first prototype of the robotic inflation device) with standard deviation and average error for each phantom configuration. Experimental data were processed using the sizing algorithm based on the numerical model of the balloon free inflation.

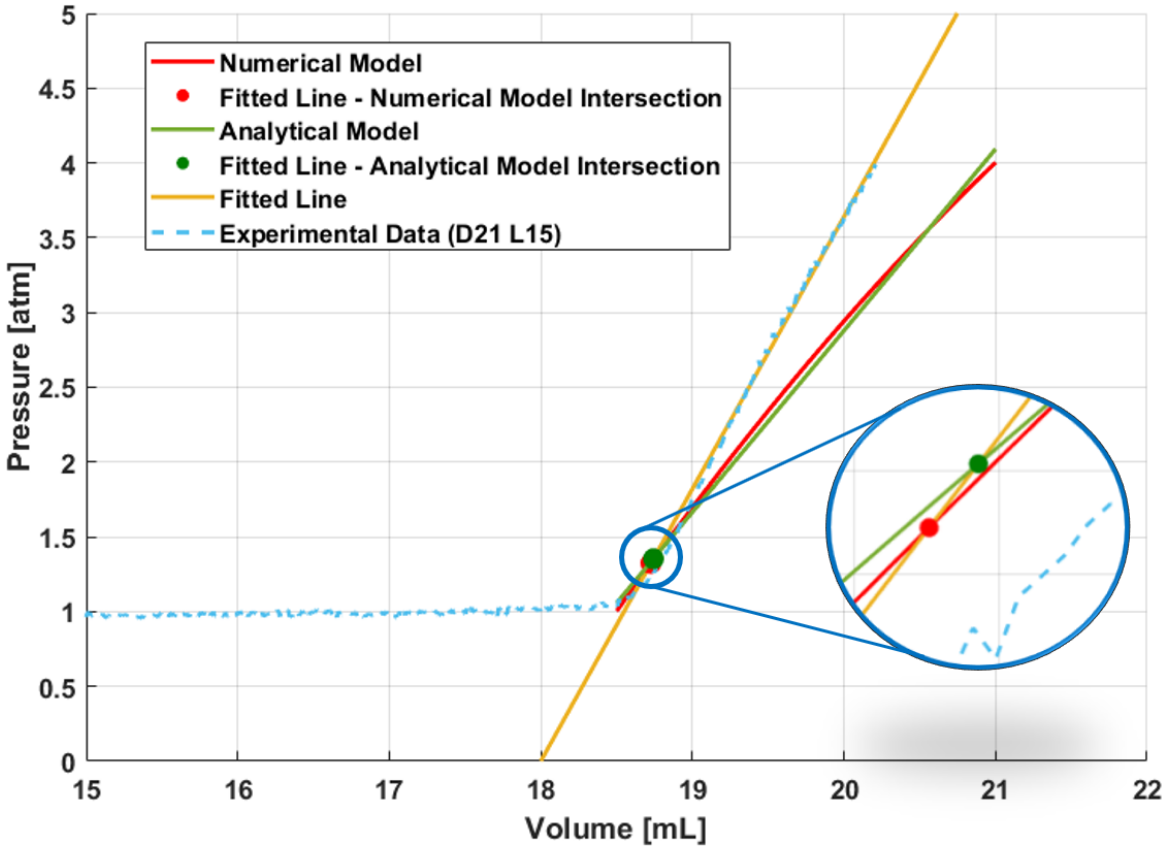

Fig. 4.3 The graph illustrates the processing of the same experimental p-v dataset (phantom diameter 21 mm, annular length 15 mm) with both versions of the sizing algorithm.

hand, it would be reasonable to expect the analytical model to lower the accuracy of the sizing algorithm, given its higher degree of approximation compared to the numerical one. Very likely that is not the case because of the characteristic compliance of the robotic inflation device. In Section 3.2.3, it was explained how the inherent compliance of the components of the platform precluded the selection of more accurate material descriptions for the numerical model. The same reasoning can be applied to fully understand the experimental results. Almost certainly, the numerical model provides a more accurate description of the balloon mechanics. Nevertheless, the analytical model, with its additional degree of freedom t_s determined through calibration, is more flexible and it can adapt slightly better to the additional compliance introduced by the inflation device itself.

By looking at p-v datasets acquired during different test runs performed on the same phantom, it can be observed that often p-v curves appear to be mildly shifted along the x-axis. As shown in Fig. 4.4, that can actually have a more significant impact on the estimated annular diameter than the mathematical model of the balloon free inflation selected for the sizing

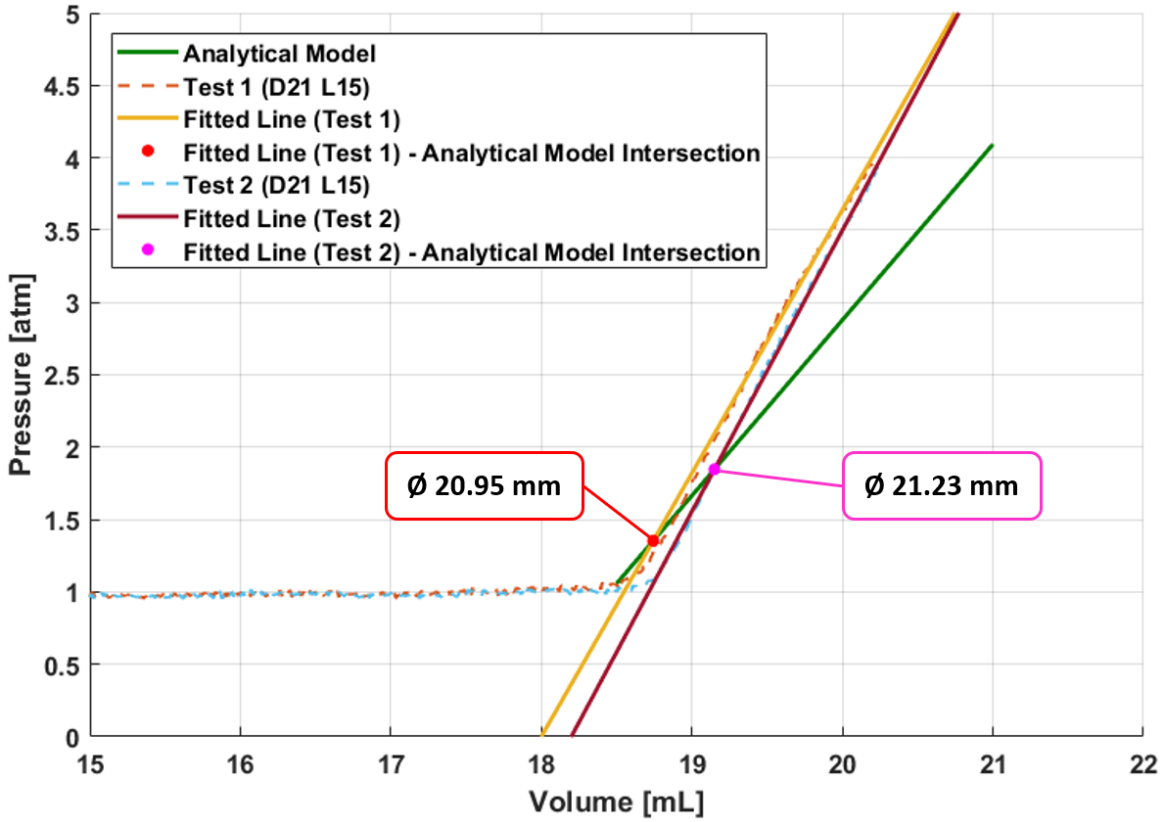

Fig. 4.4 The graph illustrates the processing of two p-v datasets acquired during different test runs performed on the same phantom (phantom diameter 21 mm, annular length 15 mm). The p-v curves are slightly shifted along the x-axis. That explains the difference between the two estimated annular diameters.

algorithm. Very likely, this phenomenon can be imputed to inaccuracies associated with the logic implemented to control the position of the plunger. The open-loop nature of the chosen control-strategy does not allow to check whether the motor loses steps during the motion. Moreover, the absence of a dedicated sensor, such as a proximity, to precisely home the plunger after each experiment introduces an additional potential source of errors. This problem probably represents the main cause of variability in the observed results. Therefore, it also explains the discrepancies in the average measurements obtained for the same diameter and different annular lengths.

4.2 Sizing Idealised Rigid Annular Phantoms with the Second Prototype of the Inflation Device

The experiments described in this section were carried out to compare the performance of the two robotic inflation devices using the idealised rigid phantoms as a reference. The test rig, which includes the platform previously described in Section 3.1.2, is shown in Fig. 4.5. It is relevant to specify that the platform was not rigidly fixed to the table. The importance of this detail will be clarified in the next subsection.
The protocol used for the tests is very similar to the one described in Section 4.1 and it can be summarised as follows:

1. The plunger of the gas tight syringe was moved all the way back inside the barrel to its homing position. Subsequently, the hydraulic circuit connecting the syringe, the pressure sensor and the catheter was filled with saline solution by means of a standard syringe connected to one of the two 3-way stopcock valves. The orientation of the platform was changed several times during the filling process in order to facilitate

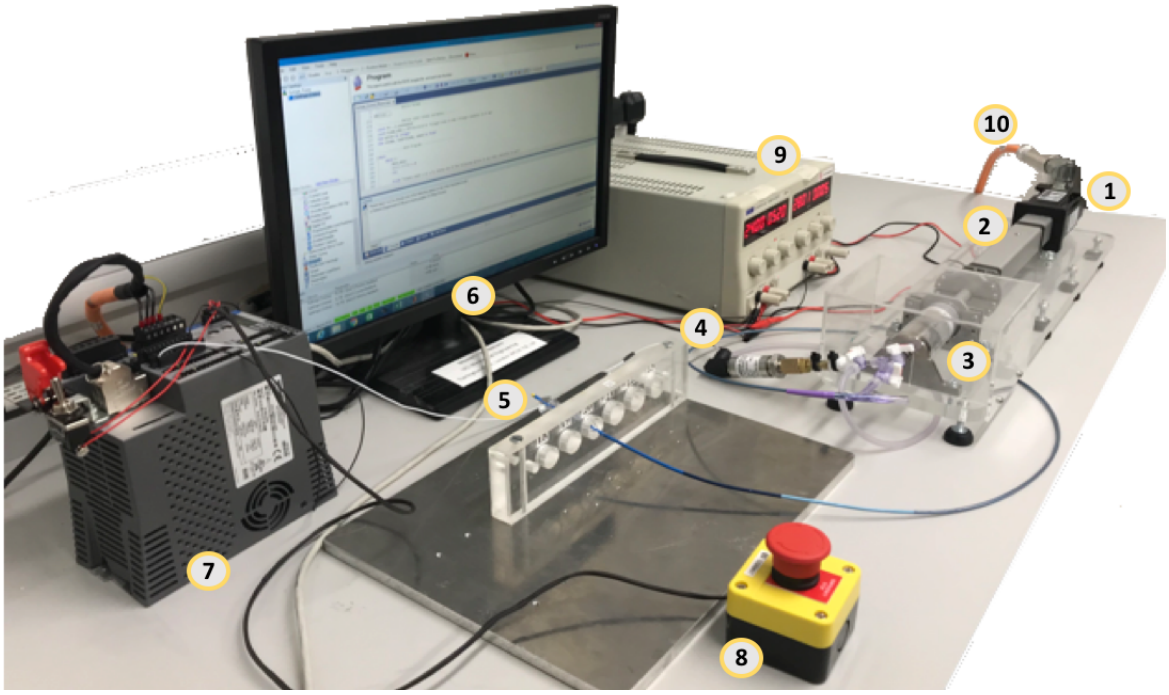

Fig. 4.5 1) Servomotor 2) Linear actuator 3) Gas tight syringe 4) Pressure transducer 5) Balloon catheter 6) PC with AKD Workbench 7) Motor drive 8) Emergency button 9) Auxiliary power supplier for the drive and the pressure transducer 10) Motor-drive cable [88].

the removal of all visible air bubbles. At the end of the procedure, the circuit was closed and the additional syringe was removed. A very small amount of saline solution was left inside the catheter in order to have the balloon in its fully deflated state at atmospheric intra-balloon pressure;

2. Free inflation p-v data were acquired, according to the procedure described in Section 3.2.2, to calibrate the parameters of both the analytical (see Section 3.2.2) and the numerical (see Section 3.2.3) models of the balloon free inflation;

3. Only the two phantoms with annular length 20 mm and inner diameters 21 and 22 mm were taken into account for the experiments. For each phantom configuration five p-v curves were extracted (ten tests in total). During each run the balloon was placed inside the phantom and inflated to an absolute intra-balloon pressure of 4.5 atm at a flow rate of approximately 1 $\frac{\text{ml}}{\text{s}}$. No particular precautions were taken to enforce any axial positioning of the balloon. At the end of each test the plunger was moved back to its homing position. A one minute wait between each run was imposed to minimise the impact of viscoelastic effects on the acquired p-v data;

4. Acquired p-v data were imported into Matlab and processed offline using both versions of the sizing algorithm, the one based on the analytical model and the one based on the numerical model. The results of the processing will be presented and discussed in the next subsection, alongside additional observations about the acquired data.

4.2.1 Results and Discussion

A unique p-v curve for each phantom configuration was obtained by averaging the results of the five tests, as shown in Fig. 4.6. Visually speaking, the curves look quite similar to their counterparts depicted in Fig. 4.2, obtained with the first prototype of the robotic inflation device. In particular, the slope of the portions where the membrane of the balloon is tensioned is almost identical. Unfortunately, this implies that the second platform is not significantly stiffer than the first one. Its weakest link is the perspex plate (see Section 3.1.2) that gradually bends as the increasing pressure pushes the plunger and the barrel of the syringe in opposite directions. This phenomenon remains invisible to the naked eye in the pressure range adopted for the experiments. The problem was spotted while trying to verify the nominal maximum capabilities of the system (measured absolute pressure ≈ 6 atm). It is important to highlight that the first prototype of the inflation device is altogether structurally weaker than the second one. However, for the experiments described in the previous section this specific problem was unknowingly mitigated by fixing the inflation device to a steel plate.

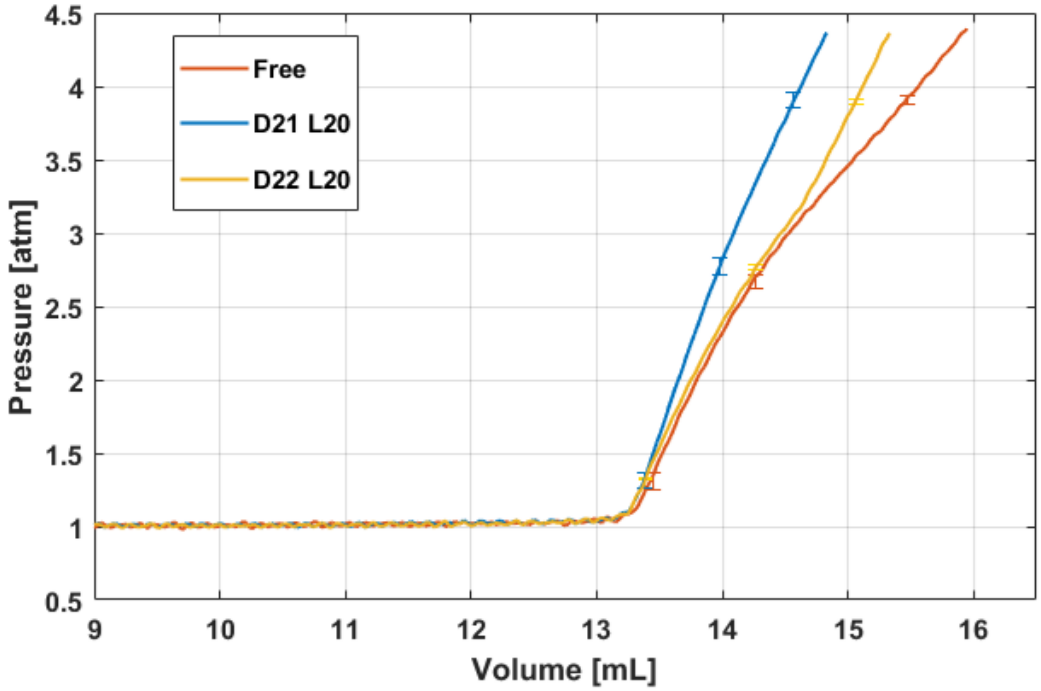

Fig. 4.6 Comparison between average absolute pressure-volume curves obtained by inflating the balloon inside two rigid phantoms with different diameters (D) and same length (L), using the second prototype of the robotic inflation device.

On the good side, the datasets extracted with the second platform overall exhibit slightly lower values of standard deviation, indicating better repeatability. Very likely, this improvement can be attributed to the preciser closed-loop strategy implemented to control the position of the plunger.

Tab. 4.3 summarises the results obtained by processing the acquired p-v datasets with both versions of the sizing algorithm. The measured values confirm the conclusion drawn in the

Phantom Diam. [mm]	Length [mm]	Mathematical Model	Avg. Meas. Diam. [mm]	Std. Dev. [mm]	Avg. Err. [%]
21	20	analytical	20.803	±0.055	0.937
22	20	analytical	22.086	±0.024	0.392
21	20	numerical	20.774	±0.080	1.075
22	20	numerical	22.313	±0.021	1.421

Table 4.3 Nominal annular diameter vs average measured diameter (second prototype of the robotic inflation device) with standard deviation and average error for each phantom configuration. Experimental data were processed using both versions of the sizing algorithm, setting a threshold of 0.03 atm for the RMSE in the iterative line fitting algorithm.

previous section that intra-balloon p-v data can be used to determine the annular diameter of idealised rigid phantoms. Nevertheless, the second platform performed slightly worse than the first one in each of the phantom configurations considered for the comparison. The most significant discrepancies were detected in the measurements taken on the phantom characterised by an inner diameter of 21 mm. By visually inspecting the processing outputs associated with this phantom configuration, it was observed that the lines created through the iterative line fitting algorithm were not precisely overlapping the portions of the p-v curves where the membrane of the balloon is tensioned. This problem could be caused by the intrinsic characteristic compliance of the second platform, which influences acquired p-v data in such a way that the portions where the balloon material is stressed exhibit a more pronounced non-linear shape compared to their counterparts extracted with the first platform. Hence, the default RMSE threshold value (0.03 atm) in the iterative line fitting algorithm might be too tight, forcing the program to discard more p-v data than intended.

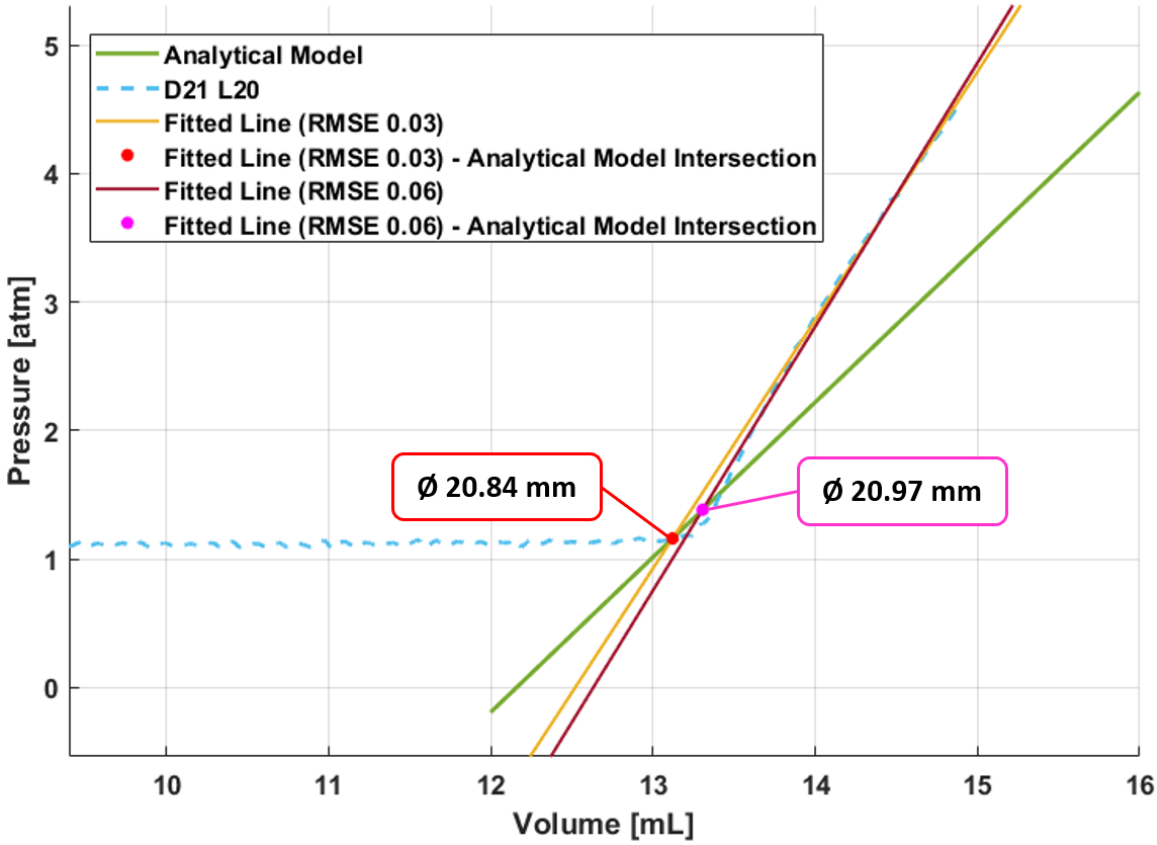

Fig. 4.7 The graph illustrates the processing of the same experimental p-v dataset (phantom diameter 21 mm, annular length 20 mm) with the version of the sizing algorithm based on the analytical model, using two different RMSE thresholds (0.03 and 0.06 atm) in the iterative line fitting algorithm.

Phantom Diam. [mm]	Length [mm]	Mathematical Model	Avg. Meas. Diam. [mm]	Std. Dev. [mm]	Avg. Err. [%]
21	20	analytical	20.942	$\pm$0.043	0.276
22	20	analytical	21.983	$\pm$0.034	0.075
21	20	numerical	20.963	$\pm$0.057	0.174
22	20	numerical	22.260	$\pm$0.027	1.180

Table 4.4 Nominal annular diameter vs average measured diameter (second prototype of the robotic inflation device) with standard deviation and average error for each phantom configuration. Experimental data were processed using both versions of the sizing algorithm, a new threshold of 0.06 atm for the RMSE in the iterative line fitting algorithm.

Based on this hypothesis, the p-v datasets obtained with the second platform were processed again, changing the value of the RMSE threshold from 0.03 to 0.06 atm. The updated results, reported in Tab. 4.4, seem to confirm the aforementioned hypothesis. Although the new RMSE threshold allowed to lower the average error in all examined cases, the measurements taken on the phantom with annular diameter 21 mm are the ones that benefited most from this change. Fig. 4.7 helps visualising the impact of the RMSE threshold on the sizing process.

4.3 Sizing Idealised Compliant Annular Phantoms with the Second Prototype of the Inflation Device

The experiments discussed in this section were performed to assess the impact of the compliance of the implantation region on the performance of the proposed sizing approach. That was done by using the second prototype of the robotic inflation device to inflate the balloon catheter inside the compliant idealised phantoms presented in Section 3.4.
The same experimental protocol described in the previous section was adopted:

- The hydraulic circuit of the platform had already been filled with saline solution and the calibration parameters had been extracted for the tests on the rigid phantoms;
- For each phantom configuration five p-v curves were extracted. Considering that two annular diameters (21 and 22 mm) and four values of shore hardness (60A, 70A, 85A, 95A) were taken into account, forty tests were performed in total. During each run the phantom was positioned on the table. Then, the balloon was placed inside the phantom and inflated to an absolute intra-balloon pressure of 4.5 atm at a flow rate of approximately $1\,\frac{\text{ml}}{\text{s}}$. No particular precautions were taken to enforce any axial positioning of the balloon. At the end of each test the plunger was moved back to its

homing position. A one minute wait between each run was imposed to minimise the impact of viscoelastic effects on the acquired p-v data;

- Acquired p-v data were imported into Matlab and processed offline using both versions of the sizing algorithm, the one based on the analytical model and the one based on the numerical model. Based on the observations discussed in the previous section, an RMSE threshold of 0.06 atm was set for the iterative line fitting algorithm. The results of the processing will be presented and discussed in the next subsection, alongside additional observations about the acquired data.

4.3.1 Results and Discussion

The average p-v curves with associated standard deviation values for each phantom configuration are shown in Fig. 4.8 and Fig. 4.9. Based on the two graphs, it can be immediately noticed that for phantoms with the same annular diameter the slope of the portion of the p-v curve deviating from the free inflation curve increases with the stiffness of the phantom.

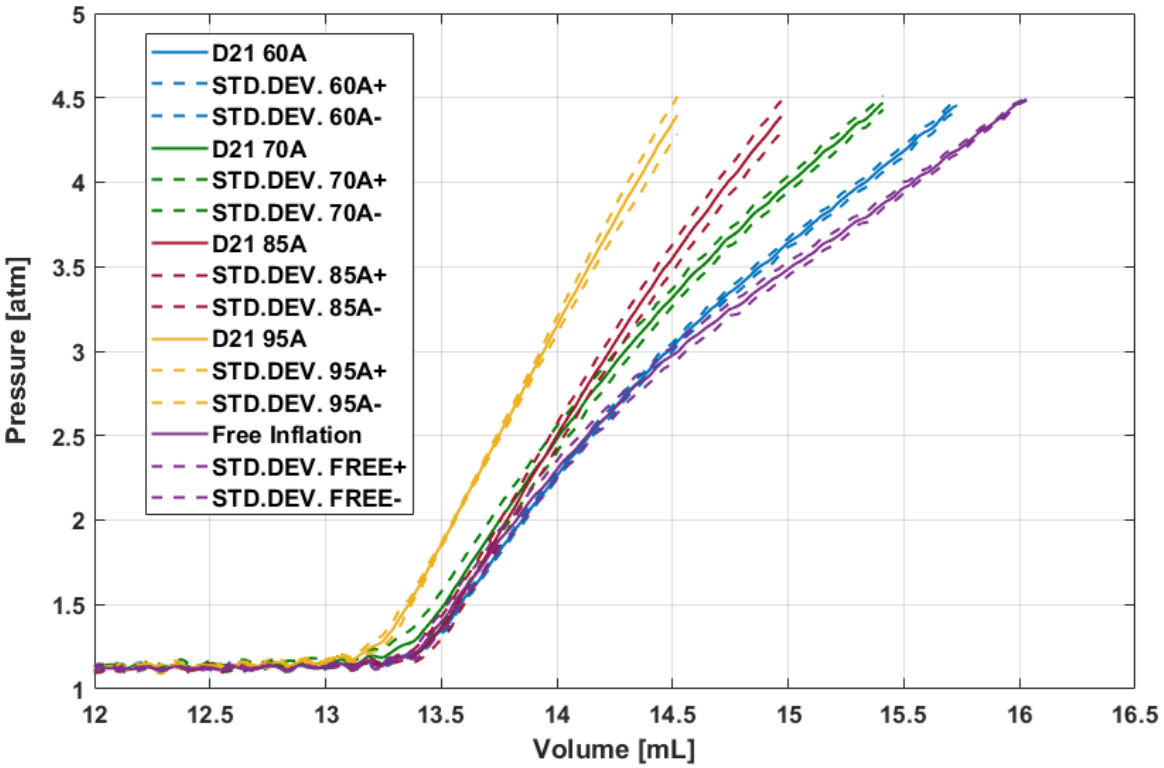

Fig. 4.8 Comparison between average absolute pressure-volume curves obtained by inflating the balloon inside compliant phantoms with diameter 21 mm and different shore hardness (60A, 70A, 85A, 95A), using the second prototype of the robotic inflation device.

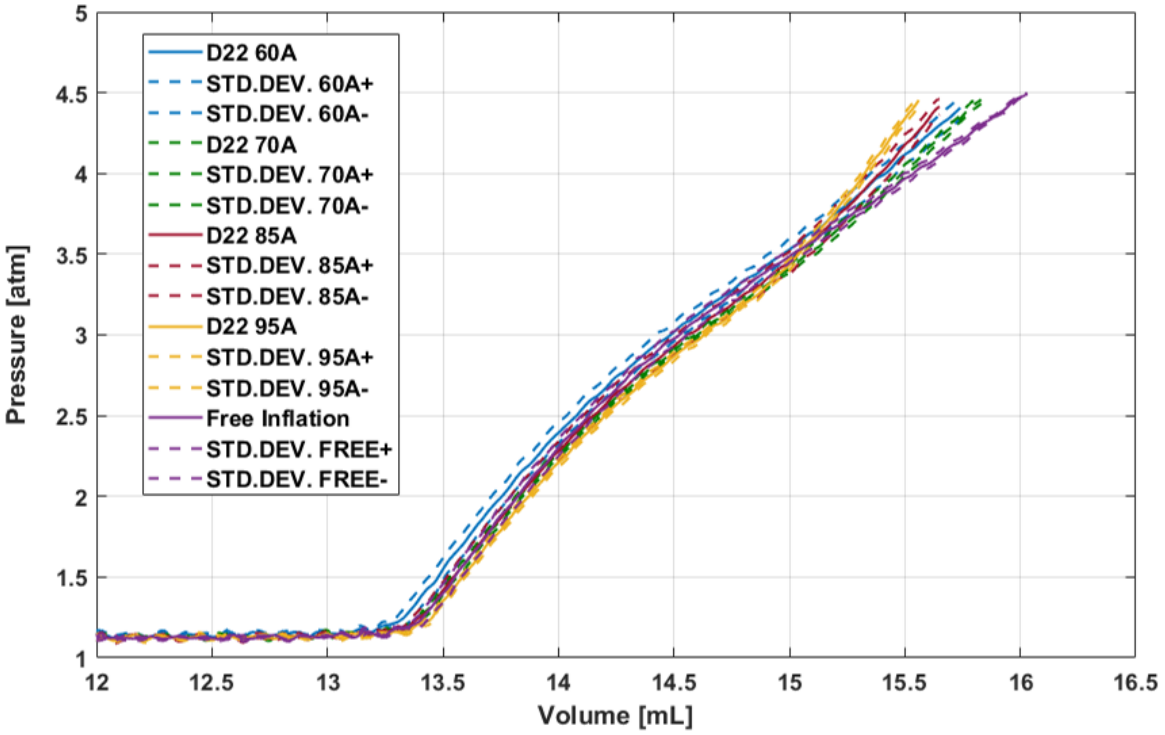

Fig. 4.9 Comparison between average absolute pressure-volume curves obtained by inflating the balloon inside compliant phantoms with diameter 22 mm and different shore hardness (60A, 70A, 85A, 95A), using the second prototype of the robotic inflation device.

Not surprisingly, both the material properties of the phantom and the annular length have an impact on the steepness of the aforementioned portion of the p-v curve (see Section 4.1). That means that it could potentially be impossible to distinguish a stiffer implantation region from a longer one by simply looking at p-v data.

In addition, it can be observed that, for lower values of shore hardness, the portion of the p-v curve that deviates from the free inflation curve becomes less linear. That could possibly represent a problem for the sizing strategy, which relies on an iterative line fitting algorithm to identify the point of full contact between the balloon and the annular walls.

The results of the sizing associated with both versions of the sizing algorithm are summarised in Tab. 4.5. Three different colors, orange, red and magenta, are used to identify the cases where a valid value for the annular diameter cannot be retrieved. Average diameters, standard deviations and average errors are calculated without taking these cases into account. Orange values represent balloon diameters that are inconsistent with the catheter intrinsic characteristics and the pressure range measured during the experiments (from approximately 1 to 4.5 atm). Based on the technical specifications and the reconstructed unstretched non-collapsed geometry of the balloon catheter, thoroughly discussed in Section 3.2, the range of admissible

Nominal Phantom Diameter 21 mm (Analytical)								
Shore [A]	Test 1 [mm]	Test 2 [mm]	Test 3 [mm]	Test 4 [mm]	Test 5 [mm]	Avg. Meas. Diam. [mm]	Std. Dev. [mm]	Avg. Err. [%]
95	20.923	20.953	20.953	20.868	20.936	**20.927**	±0.031	0.350
85	21.282	21.153	21.214	21.211	21.285	**21.229**	±0.050	1.090
70	20.566	19.975	20.490	20.977	20.247	**20.977**	0	0.110
60	20.621	20.133	20.494	20.526	19.717	-	-	-
Nominal Phantom Diameter 22 mm (Analytical)								
Shore [A]	Test 1 [mm]	Test 2 [mm]	Test 3 [mm]	Test 4 [mm]	Test 5 [mm]	Avg. Meas. Diam. [mm]	Std. Dev. [mm]	Avg. Err. [%]
95	22.069	22.210	22.263	22.239	22.226	**22.201**	±0.068	0.915
85	20.556	21.584	21.148	21.869	21.663	**21.566**	±0.263	1.972
70	20.739	21.816	22.110	46.863	23.235	**21.963**	±0.147	0.168
60	24.199	33.662	43.563	26.767	23.888	-	-	-
Nominal Phantom Diameter 21 mm (Numerical)								
Shore [A]	Test 1 [mm]	Test 2 [mm]	Test 3 [mm]	Test 4 [mm]	Test 5 [mm]	Avg. Meas. Diam. [mm]	Std. Dev. [mm]	Avg. Err. [%]
95	20.930	20.964	20.964	20.865	20.946	**20.934**	±0.037	0.315
85	21.392	21.233	21.302	21.317	21.404	**21.330**	±0.0627	1.570
70	NI	NI	NI	21.137	NI	**21.137**	0	0.652
60	20.9/21.9	NI	21.1/21.6	21.0/21.7	NI	-	-	-
Nominal Phantom Diameter 22 mm (Numerical)								
Shore [A]	Test 1 [mm]	Test 2 [mm]	Test 3 [mm]	Test 4 [mm]	Test 5 [mm]	Avg. Meas. Diam. [mm]	Std. Dev. [mm]	Avg. Err. [%]
95	22.069	22.21	22.263	22.239	2.226	**22.201**	±0.068	0.915
85	21.2/21.3	22.144	22.077	22.364	22.298	**22.221**	±0.115	1.003
70	20.8/22.3	22.441	22.500	22.573	20.9/22.5	**22.505**	±0.054	2.294
60	21.1/22.3	NI	NI	21.4/22.0	21.5/22.0	-	-	-

Table 4.5 p-v data acquired by inflating the balloon catheter inside the compliant phantoms were processed using both versions of the sizing algorithm. The results are summarised in the table above.

diameters can only span from 20.75 to 23 mm. The red-colored NI abbreviation, which stands for "no intersection", indicates that the line identified through the iterative line fitting algorithm does not intersect the mathematical model of the balloon free inflation (Fig. 4.10a). Hence, the annular diameter cannot be estimated. The magenta is used to highlight all cases where two plausible annular diameters are determined and a it is therefore impossible to choose a unique result (Fig. 4.10b). That happens when two solutions to the system of equations in the sizing algorithm (see Algorithm 2 in 3.3) are found. Obviously, since the analytical model of the balloon free inflation is characterised by a linear $p(v)$ function, the

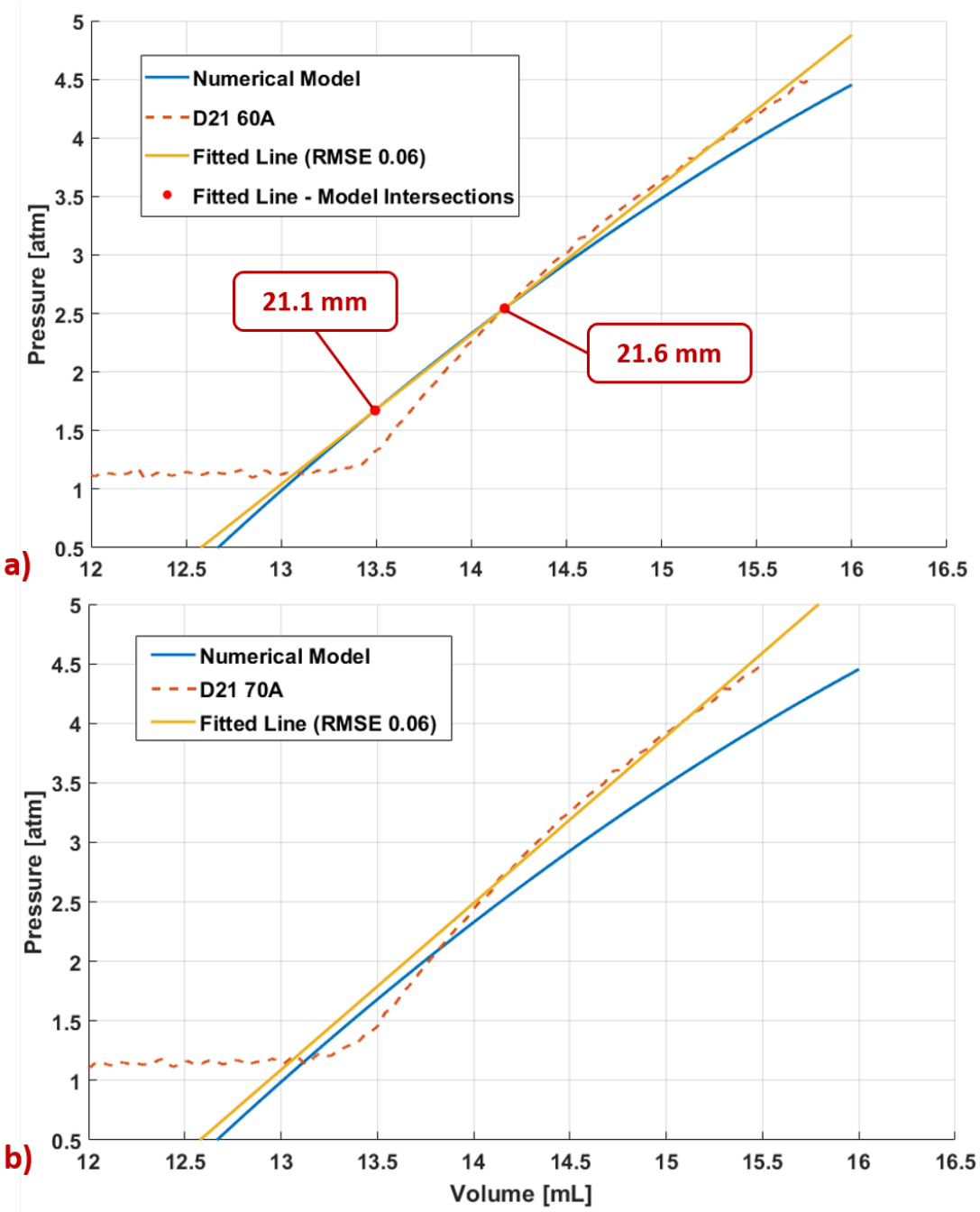

Fig. 4.10 a) The graph illustrates the case where two valid annular diameters, 21.1 and 21.6 mm, are determined b) The graph depicts the case where no intersection between the fitted line and the numerical model of the balloon free inflation is found.

situations associated with red and magenta can only occur when the numerical model is used. The results in Tab. 4.5 extend some of the conclusions discussed in the previous two sections of this chapter. As a matter of fact, they confirm that intra-balloon p-v data can be used

to determine the annular diameter of idealised phantoms characterised by a rigidity greater than approximately 100 kPa/% (see Tab. 3.10 in Section 3.4). On phantoms characterised by values of rigidity in the aforementioned range, the proposed approach showed good repeatability (maximum standard deviation $\pm$ 0.263 mm and $\pm$ 0.115 mm with the analytical and the numerical model, respectively) and high accuracy (maximum average error 1.972% and 1.570% with the analytical and the numerical model, respectively).
On the contrary, on more compliant phantoms, the proposed method failed to robustly return a precise estimate of the annular diameter. The problem essentially lies in the strategy adopted to identify the contact point between the balloon and the annular walls within the acquired p-v dataset. As predicted, the iterative line fitting algorithm does not perform well on p-v data associated with softer materials. In such cases, due to the non-linearity of p-v data, many points are discarded by the algorithm and the line ends up fitting only the upper portion of the curve that deviates from the free inflation curve (Fig. 4.10a and Fig. 4.10b). That introduces a misplacement of the contact point, which in turn causes the sizing algorithm to output incorrect or invalid results. It is also important to highlight that for softer annuli the interaction between the balloon catheter and the annular walls clearly produces less perceivable variations on p-v data. Therefore, the angle of incidence between the fitted line and the mathematical models of the balloon free inflation is bigger, making the sizing process more sensitive to disturbances and prone to errors.

4.4 Assessing the Impact of Injection Speed on Pressure-Volume Data

The mathematical models of the balloon free inflation developed in the context of this project were created neglecting the viscoelastic properties of the material composing the balloon membrane. As a result, time-independent relationships between intra-balloon pressure and volume were defined for both models (Equation 3.11 and 3.16). Based on this approximation, all the experiments presented in the previous sections of this chapter were performed keeping a very low flow rate during the inflation ($\leq 1 \frac{\text{ml}}{\text{s}}$). That allowed to evaluate the proposed sizing approach under quasi-static conditions, minimising the impact of head losses, associated with the fluid flowing from the syringe to the balloon, on acquired p-v data.
The experiments described in this section were performed to qualitatively assess what happens to p-v data when the injection speed is increased to the values potentially required by the real application (Sec. 1.1.3) and highlight potential problems that would limit the applicability

of the proposed sizing methodology in such conditions. The experimental protocol can be summarised as follows:

1. The second prototype of the robotic inflation device, whose hydraulic circuit had already been filled with saline solution, was used;

2. Five different injection flow rates (0.5, 1, 2, 4 and 8 $\frac{\text{ml}}{\text{s}}$) were taken into account for the analysis. For each injection speed five experimental free inflation p-v curves were acquired. Twenty-five tests were performed in total. During each run the balloon was placed on the table in front of the inflation device and inflated to an absolute intra-balloon pressure of 4.5 atm. A one minute wait between each experiment was imposed to minimise the impact of viscoelastic effects on the acquired p-v data;

3. Acquired data were imported into Matlab and averaged in order to obtain a unique p-v curve for each injection flow rate. The observations emerged from the visual inspection

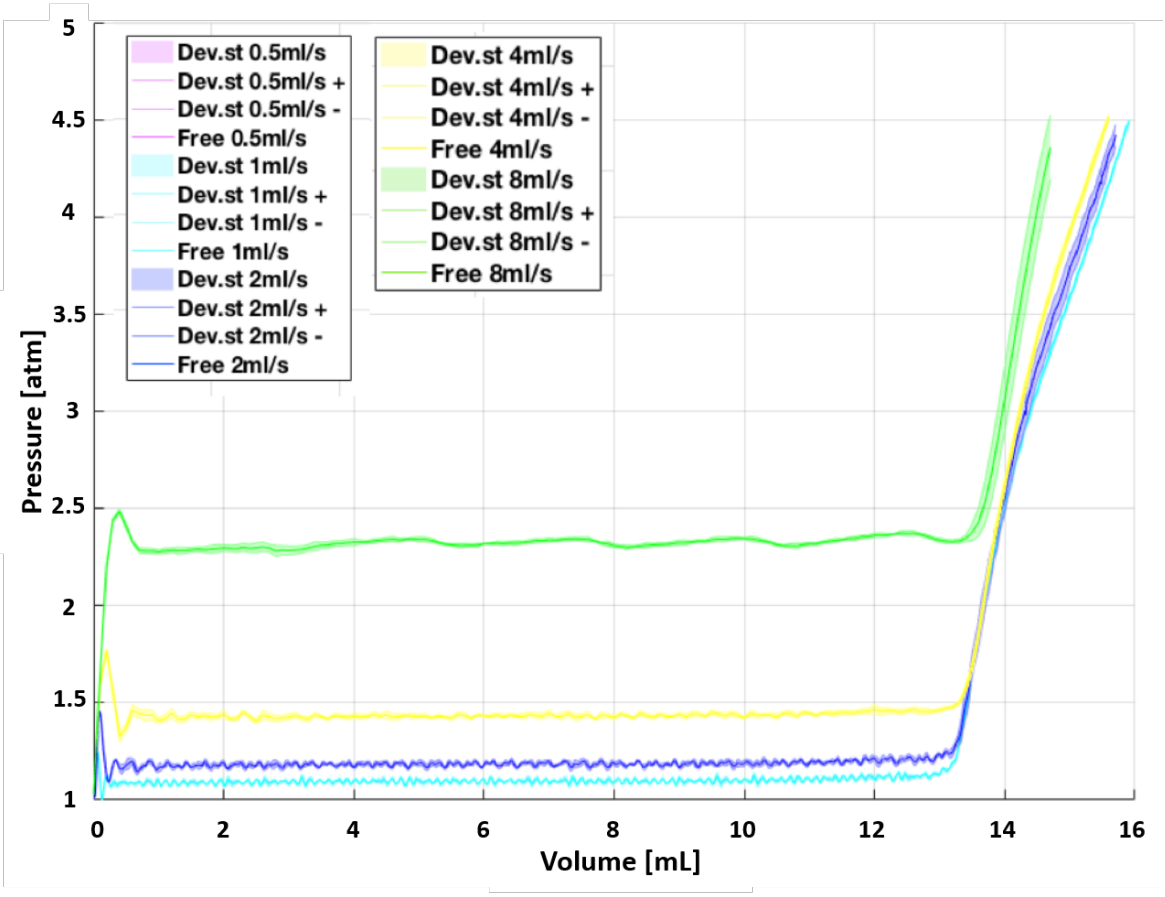

Fig. 4.11 Average free inflation p-v curves obtained by inflating the balloon catheter at different speeds using the second prototype of the robotic inflation device.

of the curves will be presented and discussed in the next subsection, together with a strategy to mathematically model the head losses of the system;

4.4.1 Results and Discussion

The average p-v curves associated with the different injection flow rates are shown in Fig. 4.11. The values of standard deviation plotted on the graph demonstrate that the repeatability of p-v curves is consistently good regardless of the injection speed. That confirms again the reliability of the second prototype of the robotic inflation device. Tab. 4.6 includes an average value of standard deviation for each injection flow rate. For each case, the value is calculated by simply averaging the standard deviation values of all the data points that belong to the average free inflation p-v curve. Such repeatability can only be achieved if a sufficiently long waiting time is applied in between test runs. Fig. 4.12 shows what happens to acquired p-v data when the balloon is repeatedly inflated and deflated without waiting the right amount of time. Due to its viscoelastic properties, the balloon membrane is unable to

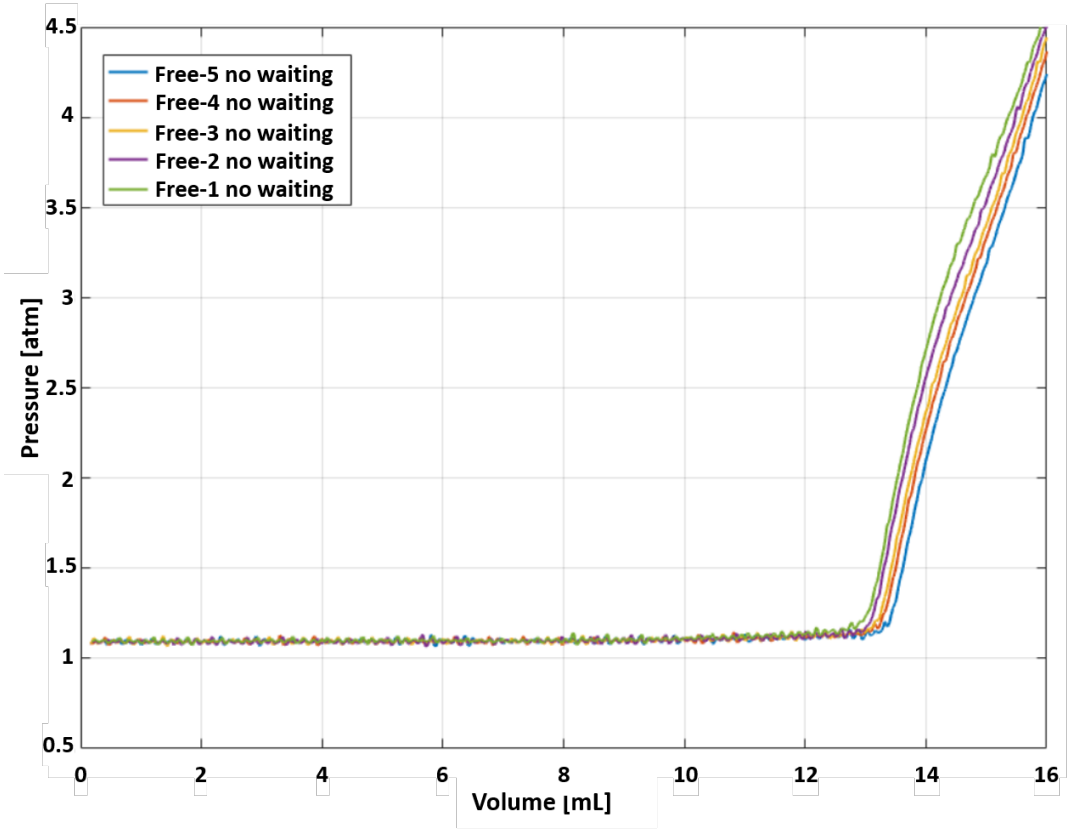

Fig. 4.12 Free inflation p-v curves consecutively acquired only waiting a few seconds between each run (1 $\frac{\text{ml}}{\text{s}}$ injection flow rate).

Injection Flow Rate [$\frac{ml}{s}$]	0.5	1	2	4	8
Average Standard Deviation [atm]	0.009	0.009	0.021	0.010	0.023

Table 4.6 Average standard deviation value extracted for each average p-v curve.

recover its initial shape at the end of each deflation. As a result, a progressive shift along the x-axis can be observed.

The average p-v curves depicted in Fig. 4.11 were manually shifted along the y-axis to minimise the impact of head losses on p-v data and appreciate potential differences in the portion of the curves where the balloon membrane is tensioned (Fig. 4.13). The values of the pressure offsets applied to the datasets are summarised in Tab. 4.7. For all the examined injection flow rates the membrane of the balloon exhibited the same mechanical response with good approximation. Nevertheless minor differences can be observed on the average

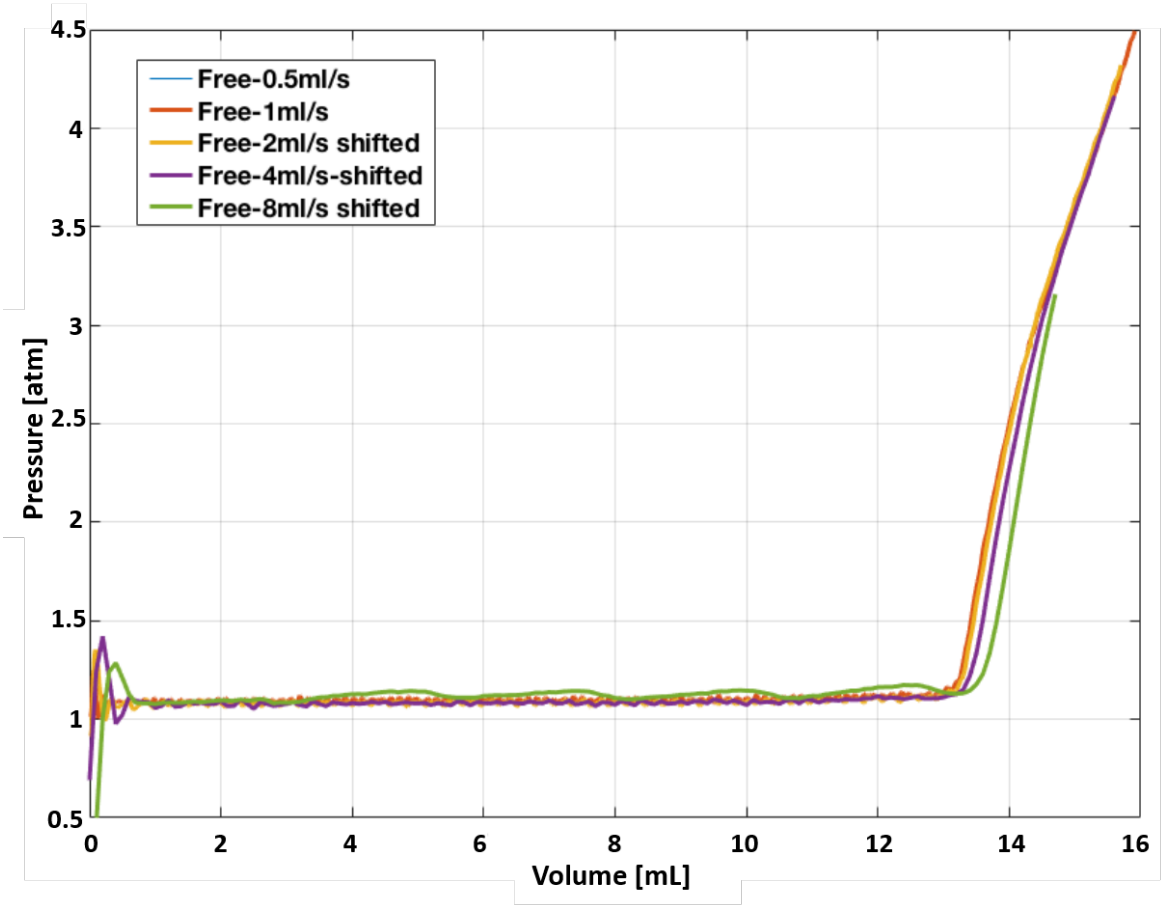

Fig. 4.13 The average free inflation p-v curves previously shown in Fig. 4.11 were manually shifted along the y-axis to make them overlap and facilitate visual inspection.

Injection Flow Rate [$\frac{\text{ml}}{\text{s}}$]	0.5	1	2	4	8
Pressure Offset [atm] ([kPa])	0 (0)	0 (0)	-0.1 (-10.1)	-0.35 (-35.5)	-1.2 (121.6)

Table 4.7 Pressure offsets applied to the p-v datasets to minimise the influence of head losses.

curve associated with a flow rate of 8 $\frac{\text{ml}}{\text{s}}$. Such curve shows a small shift along the x-axis. Furthermore, the slope of the portion where the balloon membrane is tensioned seems to be slightly steeper compared to the other cases. Although these effects could be potentially caused by the higher injection speed, further analysis is required to claim that a direct connection exists. From the graph displayed in Fig. 4.13, it can also be observed that the average curves, associated with injection speed greater than 1 $\frac{\text{ml}}{\text{s}}$, are characterised by the presence of a small pressure peak at very low volume. That could be an expression of the combined viscoelastic properties of the inflation device and the catheter. However, the fact that the height of this peak does not increase with injection speed suggests that this effect might actually be caused by electromagnetic phenomena.

At this stage, considering the results of the qualitative analysis, it can be concluded that a time-independent mathematical model is suitable to describe the mechanical behaviour of the balloon. Therefore, the injection speeds required in the real application do not represent a limit for the proposed sizing approach, provided that the head losses associated with such speeds can be precisely estimated.

Assuming that head losses are uniquely caused by the catheter shaft, the minor losses can be expressed as:

$$P_{min} = (\xi_{in} + \xi_{out})\rho\frac{V_s^2}{2} \tag{4.2}$$

where $\xi_{in} = 0.9$ and $\xi_{out} = 0.2$ are the standard coefficients associated with the inlet and the outlet of a pipe respectively, $\rho = 997$ kg/m^3 is the density of water at 25 °C, V_s is the average velocity of the fluid inside the catheter shaft. On the assumption that in standard operating conditions the flow inside the catheter is turbulent, the Darcy–Weisbach equation can be used to calculate the major losses:

$$P_{maj} = \frac{f_D\rho V_s^2 L_s}{2D_s} \tag{4.3}$$

where $f_D = 0.038$ is the Darcy friction factor extracted from the Moody diagram considering a pipe roughness $\varepsilon = 0.0025$ mm, $L_s = 1.3$ m is the length of the catheter shaft and D_s is the unknown equivalent inner diameter of the shaft. The flow inside the shaft can be considered

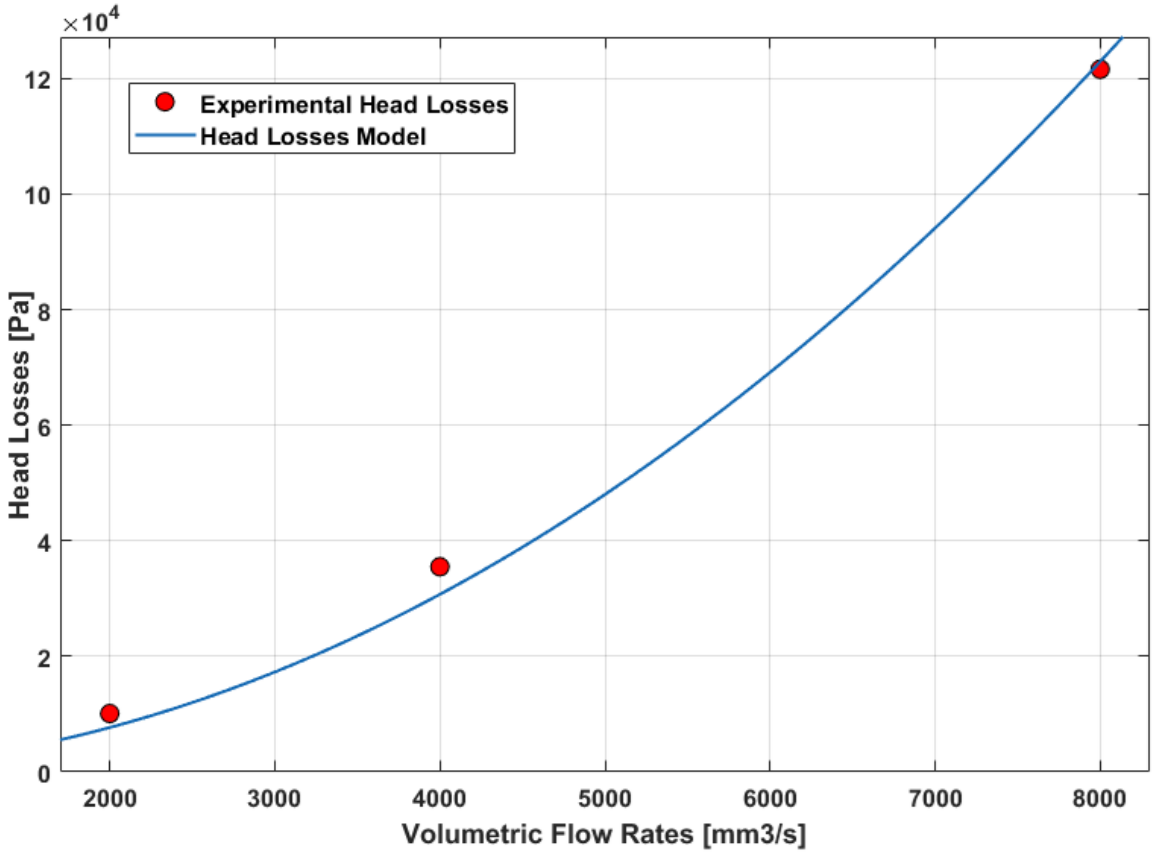

Fig. 4.14 Free inflation p-v curves consecutively acquired only waiting a few seconds between each run (1 $\frac{\text{ml}}{\text{s}}$ injection flow rate).

turbulent if its Reynolds number

$$Re = \frac{\rho V_s D_s}{\mu} > 4000 \tag{4.4}$$

where $\mu = 8.9 \cdot 10^{-4}$ *Pa s* is the dynamic viscosity of water at 25 °C.
By writing V_s as a function of the volumetric flow rate Q

$$V_s = \frac{4Q}{\pi D_s^2} \tag{4.5}$$

and putting together equations 4.2 and 4.3, the mathematical model of the head losses P_{head}, which is a function of Q and D_s, is obtained:

$$P_{head}(Q, D_s) = P_{maj} + P_{min} = (\xi_{in} + \xi_{out})\rho \frac{[(4Q)/(\pi D_s^2)]^2}{2} + \frac{f_D \rho [(4Q)/(\pi D_s^2)]^2 L_s}{2D_s} \tag{4.6}$$

Before integrating the aforementioned model with the proposed sizing approach, its dependency from the equivalent inner diameter of the shaft D_s must be removed. Since the technical specifications of the inner geometry of the shaft are not disclosed by the manufacturer, the value of D_s was determined by fitting P_{head} into experimental data from Tab. 4.7, as shown in Fig. 4.14. The resulting optimal fit, obtained for $D_s = 1.85$ mm, is characterised by a root-mean-square error $RMSE = 3895$ Pa and a coefficient of determination $R^2 = 0.99$. Such a value of D_s implies that the turbulent flow assumption holds for volumetric flow rates greater than 5.2 $\frac{\text{ml}}{\text{s}}$.

4.5 Summary

The main results and the key observations emerged from the experimental activities previously described over the course of this chapter are summarised in Tab. 4.8. All the experimental results confirm that the proposed method is capable of sizing idealised aortic annular phantoms with an error in the order of a tenth of a millimeter. Reported sizing errors associated with pre-operative imaging techniques like TTE, TEE and even MDCT are one order of magnitude larger [68]. Data collected with two different platforms and processed using two different mathematical models of the balloon free inflation demonstrated that the performance is only mildly affected by modelling inaccuracies and suboptimal control of the plunger position. On the other hand, the strategy adopted to identify the point of departure of the experimental p-v curve from the free inflation model and its parameters have an extremely significant impact on the output of the sizing algorithm.
Since the range of available TAVI prostheses is currently quite limited, the enhanced precision of the proposed method might seem redundant, as it only improves device selection in case of borderline aortic annulus. Nevertheless, in line with the trend in medicine towards more personalised treatments, the range of prosthesis sizes will increase in the future [87]. Hence, the percentage of cases where the annulus is borderline will increase as well, making better precision mandatory.

Table 4.8 Summary of results and observations emerged from the experiments.

Sec.	Experiment Description	Results and Observations
4.1	- Sizing under quasi-static conditions; - Idealised rigid annular phantoms (diameters 18, 19, 20, 21, 22 and 23 mm, annular lengths 15 and 20 mm); - First prototype of the robotic inflation device; - Analytical and numerical model of the balloon free inflation.	- It is possible to use p-v data to size idealised rigid phantoms with diameter greater than the unstretched diameter of the balloon (20.75 mm for the Edwards 9350BC23); - Results with the analytical model: max. avg. error 0.927%, max. std. dev. $\pm$0.110 mm; - Results with the numerical model: max. avg. error 1.460%, max. std. dev. $\pm$0.132 mm.
4.2	- Sizing under quasi-static conditions; - Idealised rigid annular phantoms (diameters 21 and 22 mm, annular length 20 mm); - Second prototype of the robotic inflation device; - Analytical and numerical model of the balloon free inflation.	- The second platform exhibits slightly better repeatability, but the perspex plate limits its stiffness and introduces nonlinearities in the acquired p-v curves; - Due to the nonlinearities the performance of the sizing procedure depends on the RMSE threshold of the iterative line fitting algorithm; - Results with the analytical model (RMSE 0.03 atm): max. avg. errors 0.937%, max. std. dev. $\pm$0.055 mm; - Results with the analytical model (RMSE 0.06 atm): max. avg. errors 0.276%, max. std. dev. $\pm$0.043 mm; - Results with the numerical model (RMSE 0.03 atm): max. avg. error 1.421%, max. std. dev $\pm$0.080 mm; - Results with the numerical model (RMSE 0.06 atm): max. avg. error 1.180%, max. std. dev $\pm$0.057 mm;
4.3	- Sizing under quasi-static conditions; - Idealised compliant annular phantoms (diameters 21 and 22 mm, annular length 40 mm, shore hardness 60A, 70A, 85A and 95A); - Second prototype of robotic the inflation device; - Analytical and numerical model of the balloon free inflation.	- The steepness of the portion of the p-v curve deviating from the free inflation curve increases with the stiffness of the phantom material (same impact as annular length); - For lower values of shore hardness the deviating portion of the p-v curve becomes less linear; - Intra-balloon p-v data can be used to determine the annular diameter of idealised phantoms characterised by a rigidity greater than 100 kPa/%; - Results with the analytical model (RMSE 0.06 atm): max. avg. errors 1.972%, max. std. dev. $\pm$0.263 mm; - Results with the numerical model (RMSE 0.06 atm): max. avg. error 1.570%, max. std. dev $\pm$0.115 mm;

4.4	- Balloon catheter free inflations at different injection flow rates (0.5, 1, 2, 4 and 8 $\frac{ml}{s}$); - Second prototype of the robotic inflation device; - Visual inspection of p-v data and modelling of head losses.	- Repeatability can only be guaranteed if a sufficiently long waiting time is applied in between test runs; - A time-independent mathematical model is suitable to describe the mechanical behaviour of the balloon; - Since head losses can be modelled, the injection speeds required in the real application should not limit the applicability of the proposed sizing approach.

Chapter 5

Conclusions and Future Work

In this chapter, the main research findings of the work presented so far are summarised and their impact on TAVI and other surgical procedures is discussed. Moreover, new promising directions that could be explored to potentially overcome the limitations of the proposed sizing approach are highlighted at the end of the chapter.

5.1 Conclusions

In this thesis, we presented a new approach to determine the diameter of the aortic annulus exploiting intra-balloon pressure and volume data acquired from a robotised valvuloplasty balloon catheter. The aim of the proposed solution is not to fully replace current imaging-based sizing methods. The selection of the size of the balloon catheter to be employed depends on them in the first place. Rather, it is intended as a verification tool, which could potentially refine results obtained from imprecise imaging modalities, such as TEE\TTE, and check whether the geometry of the implantation region changed as a consequence of the valvuloplasty procedure. Several steps were completed to assess the applicability of the proposed strategy.

Two robotic inflation devices, capable of collecting real-time intra-balloon pressure and volume data, were designed and interfaced with a commercially available BAV balloon catheter. The first one was manufactured to preliminary evaluate the basic idea upon which the project was initiated and highlight potential criticalities. Therefore, it was conceived to be low-cost and experimentally reproduce quasi-static inflating conditions. The second platform was built to overcome the main limitations of the first one and operate at the injection speeds required in the standard valvuloplasty procedure.

A sizing algorithm that combines a mathematical model of the balloon free inflation and an iterative linear regression method to estimate the annular diameter from acquired p-v data

was also implemented. Two mathematical models of the balloon free inflation, one analytical and one numerical, were developed and compared in this work. The former was derived by approximating the balloon as a pressurised cylindrical thin-walled vessel with hemispherical ends. The latter was obtained by performing finite element analysis on the reconstructed unstretched non-collapsed 3D geometry of the catheter.
Finally, rigid and compliant idealised annular phantoms were manufactured to test the proposed sizing method *in vitro*. The rigid set was fabricated by machining acrylic perspex plates. The compliant phantoms were 3D-printed using PolyJet technology that allows to mix two different curable liquid photopolymers in order to adjust the compliance of the final product.

The main research outcome of this work is the experimental demonstration that p-v data can be used to size idealised phantoms of the aortic annulus with good repeatability and high precision, if the annular diameter is larger than the unstretched diameter of the balloon catheter. This conclusion applies to both rigid and compliant phantoms characterised by a rigidity greater than 100 kPa/%. The fact that it is not possible to size annular diameters smaller than the unstretched diameter of the balloon does not limit the applicability of the proposed sizing approach. According to Keeble et al. [33], the size of the BAV catheter is normally selected based on the annular diameter to have a 1:1 ratio or a maximum 10% oversize. Therefore, a 23 mm BAV catheter, like the one used in this study, would never be employed for annular diameters smaller than 20.9 mm, which is still in the identified measurable range. Since typical values for the stiffness of the left ventricular outflow tract are not reported in the literature, it is difficult to understand whether the fact that it was not possible to size compliant phantoms characterised by a rigidity lower than 100 kPa/% represents a limit or not. Nevertheless, it is important to note that the rigidity value delimiting the sizeable range falls far below the maximum value of rigidity that can be considered plausible for stenotic annuli (400 kPa/%), according to Tzamtzis et al. [36].
In addition to the main outcome of this work, the following conclusions were drawn:

- **The mathematical models of the balloon free inflation** exhibited very similar performance on all the annular phantoms. That can be attributed to two main factors. Firstly, due to the impact of the inherent compliance of the robotic inflation devices on p-v data, the same linear material model was adopted for both mathematical models. Secondly, although the numerical model is built upon a more accurate reconstruction of the balloon geometry, the analytical one can compensate that advantage with its higher flexibility provided by the additional degree of freedom;

- **The conceptual design of the robotic inflation device**, of which the better implementation is embodied by the second platform, was proved to be suitable for the proposed sizing strategy. The second platform clearly demonstrated the capability of precisely and repeatably acquiring p-v data while guaranteeing high operational speed. Nevertheless, the perspex base significantly limits the overall structural stiffness of the system. That introduces an intrinsic discrepancy between the mathematical models of the balloon free inflation and experimentally acquired data. Such discrepancy should be properly compensated before considering the adoption of more accurate models taking into account the non-linearities of the balloon material;
- **The general idea behind the sizing algorithm** was also validated by the results presented in this thesis. However, the experiments shined a light on some limitations associated with the strategy employed to identify the point within the acquired p-v dataset, where the balloon starts applying pressure on the aortic annulus. The iterative line fitting algorithm can identify such point with good precision and repeatability if the portion of the p-v curve where the balloon is pushing on the annular walls is approximately linear and it is significantly steeper than the portion of the p-v curve where the balloon is being freely inflated. Unfortunately, its performance deteriorates when the two aforementioned conditions are not met. When p-v data acquired while the balloon is applying pressure are non-linear, the output of the iterative line fitting algorithm significantly depends on the selected RMSE (see Sections 4.2 and 4.3). Furthermore, it was observed that if the deviation from the free inflation p-v curve caused by the interaction with the annular walls is small, the iterative line fitting algorithm becomes more sensitive to disturbances and prone to errors (see Section 4.3);

The work presented in this thesis demonstrates how robotic and mechatronic solutions could be softly integrated into traditional clinical procedures to unlock their full potential. By simply augmenting the level of intelligence embedded in the inflation device, the proposed annulus sizing approach would allow to extract additional meaningful information from valvuloplasty, a treatment that is already part of the TAVI procedure. Such information could substantially improve TAVI device selection, potentially reducing the occurrence of aortic regurgitation and atrioventricular blocks. Since it does not require a special catheter design, this methodology could be easily transferred to other standard balloon catheters of different sizes, already used in routine clinical practice. Due to that, it is worth considering the possibility of applying a similar concept to other clinical contexts that might benefit from it. For example, in angioplasty, which is a minimally invasive procedure to widen narrowed or obstructed arteries, the proposed method could help preventing arterial rupture [93]. Similarly, in resuscitative endovascular balloon occlusion of the aorta (REBOA), which is a

technique to control bleeding in patients with injuries to the chest, abdomen or pelvis, the proposed sizing strategy could reduce the risk of damaging the vessel [94].

5.2 Limitations and Future Work

The research study presented in this thesis is characterised by the following limitations:

1. Only one balloon catheter model, the Edwards 9350BC23, was taken into account for the analysis. To make the conclusions drawn in the previous section more general, the proposed sizing approach should be experimentally validated using alternative BAV catheters with different shapes and sizes. That was not done in this project purely due to time constraints. We do not foresee any major criticalities connected with this activity. Even the integration of our sizing methodology with other standard high-pressure balloon catheters employed in different clinical procedures, like angioplasty, should be relatively straightforward. The same consideration does not necessarily apply to low-pressure balloons. Several challenges could potentially emerge from the mechanical properties of the materials they are usually made of and from the fact that they are not designed to be inflated to precise dimensions;

2. The sizing approach was tested on idealised aortic phantoms, that were designed by approximating the aortic annulus as a perfectly circular tubular structure without leaflets. The selected level of approximation seems fair, considering that the aim of this work was to conceptually validate a novel strategy. The presence of the leaflets is neglected also in current intra-operative sizing techniques used in clinical practice. Furthermore, even an elliptical elastic tubular structure becomes circular under the action of a uniform pressure applied to the inner surface. Nevertheless, experiments on more realistic patient-specific phantoms will need to be performed in the future. Replicating the complex geometry of the aortic annulus would be rather easy for modern 3D printers. Still, it would be extremely challenging to use additive manufacturing to produce geometrically realistic aortic phantom with clinically relevant mechanical properties. The possibility of 3D printing silicone, which has been widely used to mimic tissue in various applications, would probably be a game changer in this case. It is important to highlight that one of the main problems remains the lack of information about the mechanical behaviour of the left ventricular outflow tract;

3. The experimental validation of the sizing strategy was performed under quasi-static conditions instead of considering the injection speeds required in the real case scenario. Once again, the project time constraints were the main reason why additional

experiments at higher injection speeds were not carried out. The second prototype of the robotic inflation device was designed to handle realistic operating conditions. Furthermore, we laid the ground for experimentation at higher inflation velocities by qualitatively demonstrating the time-independence of the balloon mechanical behaviour and modelling the head losses associated with the flow in the catheter shaft. Considering the current status of the project, we cannot foresee any major potential issues that might impact the performance of the proposed sizing approach at higher inflation speeds;

Future work will primarily target the aforementioned limitations. In addition, the following improvements will be investigated:

- The inherent compliance of the robotic inflation device will be reduced by making its structure stiffer. Depending on the obtained results, a software-based strategy capable of compensating the impact of the inherent compliance on the sizing approach will be also implemented. That should immediately increase the sizing accuracy of the proposed approach and would also enable to exploit more accurate numerical models of the balloon free inflation;

- More objective ways of identifying the point within the acquired p-v dataset, where the balloon starts applying pressure on the aortic annulus, will be explored. That is the key to guarantee a more stable and robust sizing performance;

- An embedded computer will be integrated with the robotic inflation device to handle data acquisition and perform the computations required to determine the diameter of the aortic annulus online;

- A strategy to assess the mechanical properties of the aortic annulus from intra-balloon pressure and volume data will be implemented. This will provide the operator with supplementary helpful information for TAVI device selection, as the mechanical response of the implantation region has a critical impact on the radial forces applied by prosthetic valves.

Bibliography

[1] A. D. Lopez and T. Adair, "Is the long-term decline in cardiovascular-disease mortality in high-income countries over? evidence from national vital statistics," *International journal of epidemiology*, 2019.

[2] C. J. McAloon, L. M. Boylan, T. Hamborg, N. Stallard, F. Osman, P. B. Lim, and S. A. Hayat, "The changing face of cardiovascular disease 2000–2012: An analysis of the world health organisation global health estimates data," *International journal of cardiology*, vol. 224, pp. 256–264, 2016.

[3] B. Lacey, W. G. Herrington, D. Preiss, S. Lewington, and J. Armitage, "The role of emerging risk factors in cardiovascular outcomes," *Current atherosclerosis reports*, vol. 19, no. 6, p. 28, 2017.

[4] K. Maganti, V. H. Rigolin, M. E. Sarano, and R. O. Bonow, "Valvular heart disease: Diagnosis and management," in *Mayo Clinic Proceedings*, Elsevier, vol. 85, 2010, pp. 483–500.

[5] B. Iung, G. Baron, E. G. Butchart, F. Delahaye, C. Gohlke-Bärwolf, O. W. Levang, P. Tornos, J.-L. Vanoverschelde, F. Vermeer, E. Boersma, *et al.*, "A prospective survey of patients with valvular heart disease in europe: The euro heart survey on valvular heart disease," *European heart journal*, vol. 24, no. 13, pp. 1231–1243, 2003.

[6] R. K. Binder, M. Dweck, and B. Prendergast, "The year in cardiology: valvular heart disease: The year in cardiology 2019," *European Heart Journal*, Jan. 2020, ehz948, ISSN: 0195-668X. DOI: 10.1093/eurheartj/ehz948. eprint: http://oup.prod.sis.lan/eurheartj/advance-article-pdf/doi/10.1093/eurheartj/ehz948/31685033/ehz948.pdf. [Online]. Available: https://doi.org/10.1093/eurheartj/ehz948.

[7] K. D. Boudoulas, J. S. Borer, and H. Boudoulas, "Etiology of valvular heart disease in the 21st century," *Cardiology*, vol. 126, no. 3, pp. 139–152, 2013.

[8] A. Noble, *The Cardiovascular System Systems of the Body Series*, eng, 2nd ed., ser. Systems of the Body. London: Elsevier Health Sciences UK, 2013, ISBN: 0-7020-5082-2.

[9] G. Ampanozi, E. Krinke, P. Laberke, W. Schweitzer, M. J. Thali, and L. C. Ebert, "Comparing fist size to heart size is not a viable technique to assess cardiomegaly," *Cardiovascular Pathology*, vol. 36, pp. 1–5, 2018.

[10] A. Farley, E. McLafferty, and C. Hendry, "The cardiovascular system.," *Nursing standard (Royal College of Nursing (Great Britain) : 1987)*, vol. 27, no. 9, pp. 35–39, 2012, ISSN: 00296570.

[11] Blausen.com staff, "Medical gallery of blausen medical 2014," *WikiJournal of Medicine*, vol. 1, no. 2, 2014, ISSN: 2002-4436.

[12] C. L. VanPutte, *Seeley's essentials of anatomy & physiology / Cinnamon VanPutte, Jennifer Regan, Andy Russo.* eng, 7th ed. Boston [Mass.] ; London: McGraw-Hill, 2010, ISBN: 9780073525631.

[13] J. R. Levick, *An introduction to cardiovascular physiology*. Butterworth-Heinemann, 2013.

[14] J. G. Betts, P. DeSaix, E. Johnson, J. E. Johnson, O. Korol, D. H. Kruse, B. Poe, J. A. Wise, K. A. Young, *et al.*, *Anatomy and physiology*. OpenStax College, 2014, ISBN: 1-938168-13-5.

[15] M. J. Thubrikar, *The aortic valve*. CRC press, 1989.

[16] S. Y. Ho, "Structure and anatomy of the aortic root," *European Journal of Echocardiography*, vol. 10, no. 1, pp. i3–i10, Jan. 2009, ISSN: 1525-2167. DOI: 10.1093/ejechocard/jen243. eprint: https://academic.oup.com/ehjcimaging/article-pdf/10/1/i3/7466104/jen243.pdf. [Online]. Available: https://doi.org/10.1093/ejechocard/jen243.

[17] E. I. Charitos and H.-H. Sievers, "Anatomy of the aortic root: Implications for valve-sparing surgery," *Annals of Cardiothoracic Surgery*, vol. 2, no. 1, 2013, ISSN: 2225-319X. [Online]. Available: http://www.annalscts.com/article/view/1400.

[18] J. T. Tretter, D. E. Spicer, S. Mori, S. Chikkabyrappa, A. N. Redington, and R. H. Anderson, "The significance of the interleaflet triangles in determining the morphology of congenitally abnormal aortic valves: Implications for noninvasive imaging and surgical management," *Journal of the American Society of Echocardiography*, vol. 29, no. 12, pp. 1131–1143, 2016.

[19] A. Salica, G. Pisani, U. Morbiducci, R. Scaffa, D. Massai, A. Audenino, L. Weltert, L. Guerrieri Wolf, and R. De Paulis, "The combined role of sinuses of valsalva and flow pulsatility improves energy loss of the aortic valve," *European Journal of Cardio-thoracic Surgery*, vol. 49, no. 4, pp. 1222–1227, 2016.

[20] R. De Paulis and A. Salica, "Surgical anatomy of the aortic valve and root—implications for valve repair," *Annals of cardiothoracic surgery*, vol. 8, no. 3, p. 313, 2019.

[21] R. O. Bonow, M. B. Leon, D. Doshi, and N. Moat, "Management strategies and future challenges for aortic valve disease," *The Lancet*, vol. 387, no. 10025, pp. 1312–1323, 2016.

[22] G. A. Fishbein and M. C. Fishbein, "Pathology of the aortic valve: Aortic valve stenosis/aortic regurgitation," *Current cardiology reports*, vol. 21, no. 8, p. 81, 2019.

[23] A. Pick, *Aortic stenosis prognosis: What 6 facts should you know?* May 2019. [Online]. Available: https://www.heart-valve-surgery.com/aortic-stenosis-prognosis.php.

[24] M. J. Czarny and J. R. Resar, "Diagnosis and management of valvular aortic stenosis," *Clinical Medicine Insights: Cardiology*, vol. 8, CMC–S15716, 2014.

[25] M. B. Leon, C. R. Smith, M. Mack, D. C. Miller, J. W. Moses, L. G. Svensson, E. M. Tuzcu, J. G. Webb, G. P. Fontana, R. R. Makkar, *et al.*, "Transcatheter aortic-valve implantation for aortic stenosis in patients who cannot undergo surgery," *New England Journal of Medicine*, vol. 363, no. 17, pp. 1597–1607, 2010.

[26] R. A. Nishimura, C. M. Otto, R. O. Bonow, B. A. Carabello, J. P. Erwin, L. A. Fleisher, H. Jneid, M. J. Mack, C. J. McLeod, P. T. O'Gara, *et al.*, "2017 aha/acc focused update of the 2014 aha/acc guideline for the management of patients with valvular heart disease: A report of the american college of cardiology/american heart association task force on clinical practice guidelines," *Journal of the American College of Cardiology*, vol. 70, no. 2, pp. 252–289, 2017.

[27] H. Baumgartner, J. Hung, J. Bermejo, J. B. Chambers, A. Evangelista, B. P. Griffin, B. Iung, C. M. Otto, P. A. Pellikka, and M. Quiñones, "Echocardiographic assessment of valve stenosis: Eae/ase recommendations for clinical practice," *Journal of the American Society of Echocardiography*, vol. 22, no. 1, pp. 1–23, 2009.

[28] A. Cribier, H. Eltchaninoff, A. Bash, N. Borenstein, C. Tron, F. Bauer, G. Derumeaux, F. Anselme, F. Laborde, and M. B. Leon, "Percutaneous transcatheter implantation of an aortic valve prosthesis for calcific aortic stenosis: First human case description," *Circulation*, vol. 106, no. 24, pp. 3006–3008, 2002.

[29] R. M. Van Der Boon, B. Marcheix, D. Tchetche, A. Chieffo, N. M. Van Mieghem, N. Dumonteil, O. Vahdat, F. Maisano, P. W. Serruys, A. P. Kappetein, *et al.*, "Transapical versus transfemoral aortic valve implantation: A multicenter collaborative study," *The Annals of thoracic surgery*, vol. 97, no. 1, pp. 22–28, 2014.

[30] V. Bapat and R. Attia, "Transaortic transcatheter aortic valve implantation: Step-by-step guide," in *Seminars in thoracic and cardiovascular surgery*, Elsevier, vol. 24, 2012, pp. 206–211.

[31] A. Willson, S. Toggweiler, and J. G. Webb, "Transfemoral aortic valve replacement with the sapien xt valve: Step-by-step," in *Seminars in thoracic and cardiovascular surgery*, Elsevier, vol. 23, 2011, pp. 51–54.

[32] L. Biasco, E. Ferrari, G. Pedrazzini, F. Faletra, T. Moccetti, F. Petracca, and M. Moccetti, "Access sites for tavi: Patient selection criteria, technical aspects, and outcomes," *Frontiers in cardiovascular medicine*, vol. 5, p. 88, 2018.

[33] T. R. Keeble, A. Khokhar, M. M. Akhtar, A. Mathur, R. Weerackody, and S. Kennon, "Percutaneous balloon aortic valvuloplasty in the era of transcatheter aortic valve implantation: A narrative review," *Open Heart*, vol. 3, no. 2, e000421, 2016.

[34] P. Adamson and N. Cruden, "Emergency interventions for the treatment of decompensated aortic stenosis," *Heart*, vol. 104, no. 1, pp. 4–5, 2018, ISSN: 1355-6037. DOI: 10.1136/heartjnl-2017-311706. eprint: http://heart.bmj.com/content/104/1/4.full.pdf. [Online]. Available: http://heart.bmj.com/content/104/1/4.

[35] B. Biffi, G. M. Bosi, V. Lintas, R. Jones, S. Tzamtzis, G. Burriesci, F. Migliavacca, A. M. Taylor, S. Schievano, and G. Biglino, "Numerical model of a valvuloplasty balloon: In vitro validation in a rapid-prototyped phantom," *Biomedical Engineering online*, vol. 15, no. 1, p. 37, 2016.

[36] S. Tzamtzis, J. Viquerat, J. Yap, M. Mullen, and G. Burriesci, "Numerical analysis of the radial force produced by the medtronic-corevalve and edwards-sapien after transcatheter aortic valve implantation (tavi)," *Medical engineering & physics*, vol. 35, no. 1, pp. 125–130, 2013.

[37] S. Egron, B. Fujita, L. Gullón, D. Pott, T. Schmitz-Rode, S. Ensminger, and U. Steinseifer, "Radial force: An underestimated parameter in oversizing transcatheter aortic valve replacement prostheses: In vitro: Analysis with five commercialized valves," *ASAIO journal*, vol. 64, no. 4, pp. 536–543, 2018.

[38] M. B. Leon, C. R. Smith, M. J. Mack, R. R. Makkar, L. G. Svensson, S. K. Kodali, V. H. Thourani, E. M. Tuzcu, D. C. Miller, H. C. Herrmann, *et al.*, "Transcatheter or surgical aortic-valve replacement in intermediate-risk patients," *New England Journal of Medicine*, vol. 374, no. 17, pp. 1609–1620, 2016.

[39] U. K. Allahwala, P. S. Hansen, E. J. Danson, N. Straiton, A. Sinhal, D. L. Walters, and R. Bhindi, "Transcatheter aortic valve implantation: Current trends and future directions," *Future Cardiology*, vol. 12, no. 1, pp. 69–85, 2016.

[40] H. Möllmann, W.-K. Kim, J. Kempfert, T. Walther, and C. Hamm, "Complications of transcatheter aortic valve implantation: How to avoid and treat them," *Heart*, pp. 900–908, 2015.

[41] H. R. Figulla, J. G. Webb, A. Lauten, and T. Feldman, "The transcatheter valve technology pipeline for treatment of adult valvular heart disease," *European Heart Journal*, vol. 37, no. 28, pp. 2226–2239, 2016.

[42] A. A. Klein, N. J. Skubas, and J. Ender, "Controversies and complications in the perioperative management of transcatheter aortic valve replacement," *Anesthesia & Analgesia*, vol. 119, no. 4, pp. 784–798, 2014.

[43] C. W. Hamm, M. Arsalan, and M. J. Mack, "The future of transcatheter aortic valve implantation," *European Heart Journal*, vol. 37, no. 10, pp. 803–810, 2015.

[44] S. K. Kodali, M. R. Williams, C. R. Smith, L. G. Svensson, J. G. Webb, R. R. Makkar, G. P. Fontana, T. M. Dewey, V. H. Thourani, A. D. Pichard, *et al.*, "Two-year outcomes after transcatheter or surgical aortic-valve replacement," *New England Journal of Medicine*, vol. 366, no. 18, pp. 1686–1695, 2012.

[45] M. Scharfschwerdt, R. Meyer-Saraei, C. Schmidtke, and H.-H. Sievers, "Hemodynamics of the edwards sapien xt transcatheter heart valve in noncircular aortic annuli," *The Journal of Thoracic and Cardiovascular Surgery*, vol. 148, no. 1, pp. 126–132, 2014.

[46] Y. Maeno, Y. Abramowitz, S.-H. Yoon, H. Jilaihawi, S. Israr, M. Miyasaka, H. Kawamori, Y. Kazuno, T. Rami, N. Takahashi, *et al.*, "Transcatheter aortic valve replacement with different valve types in elliptic aortic annuli," *Circulation Journal*, vol. 81, no. 7, pp. 1036–1042, 2017.

[47] A. G. Cerillo, M. Mariani, S. Berti, and M. Glauber, "Sizing the aortic annulus," *Annals of Cardiothoracic Surgery*, vol. 1, no. 2, p. 245, 2012.

[48] D. Messika-Zeitoun, J.-M. Serfaty, E. Brochet, G. Ducrocq, L. Lepage, D. Detaint, F. Hyafil, D. Himbert, N. Pasi, J.-P. Laissy, *et al.*, "Multimodal assessment of the aortic annulus diameter: Implications for transcatheter aortic valve implantation," *Journal of the American College of Cardiology*, vol. 55, no. 3, pp. 186–194, 2010.

[49] K. Otani, M. Takeuchi, K. Kaku, L. Sugeng, H. Yoshitani, N. Haruki, T. Ota, V. Mor-Avi, R. M. Lang, and Y. Otsuji, "Assessment of the aortic root using real-time 3D transesophageal echocardiography," *Circulation Journal*, vol. 74, no. 12, pp. 2649–2657, 2010.

[50] D. Kretzschmar, A. Lauten, B. Goebel, T. Doenst, T. C. Poerner, M. Ferrari, H. R. Figulla, and A. Hamadanchi, "Optimal prosthesis sizing in transcatheter aortic valve implantation by exclusive use of three-dimensional transoesophageal echocardiography," *Clinical physiology and functional imaging*, vol. 36, no. 2, pp. 99–105, 2016.

[51] D. T. Murphy, P. Blanke, S. Alaamri, C. Naoum, R. Rubinshtein, G. Pache, B. Precious, A. Berger, R. Raju, D. Dvir, *et al.*, "Dynamism of the aortic annulus: Effect of diastolic versus systolic CT annular measurements on device selection in transcatheter aortic valve replacement (tavr)," *Journal of Cardiovascular Computed Tomography*, vol. 10, no. 1, pp. 37–43, 2016.

[52] B. Biffi and V. Lintas, "Sizing and valvuloplasty procedures: Validation of computational models and reverse engineering to infer arterial wall tissue properties," M.S. thesis, Politecnico di Milano, 2014.

[53] P. W. Serruys, N. Piazza, A. Cribier, J. Webb, J.-C. Laborde, and P. de Jaegere, *Transcatheter aortic valve implantation: tips and tricks to avoid failure*. CRC Press, 2009.

[54] V. C. Babaliaros, Z. Junagadhwalla, S. Lerakis, V. Thourani, D. Liff, E. Chen, T. Vassiliades, C. Chappell, N. Gross, A. Patel, *et al.*, "Use of balloon aortic valvuloplasty to size the aortic annulus before implantation of a balloon-expandable transcatheter heart valve," *JACC: Cardiovascular Interventions*, vol. 3, no. 1, pp. 114–118, 2010.

[55] J. A. Kisslo and P. Nihoyannopoulos, *Echocardiography*. Springer, 2009.

[56] A. Evangelista, F. A. Flachskampf, R. Erbel, F. Antonini-Canterin, C. Vlachopoulos, G. Rocchi, R. Sicari, P. Nihoyannopoulos, J. Zamorano, D. Reviewers: *et al.*, "Echocardiography in aortic diseases: Eae recommendations for clinical practice," *European Journal of Echocardiography*, vol. 11, no. 8, pp. 645–658, 2010.

[57] R. M. Lang, L. P. Badano, V. Mor-Avi, J. Afilalo, A. Armstrong, L. Ernande, F. A. Flachskampf, E. Foster, S. A. Goldstein, T. Kuznetsova, *et al.*, "Recommendations for cardiac chamber quantification by echocardiography in adults: An update from the american society of echocardiography and the european association of cardiovascular imaging," *European Heart Journal-Cardiovascular Imaging*, vol. 16, no. 3, pp. 233–271, 2015.

[58] R. R. Moss, E. Ivens, S. Pasupati, K. Humphries, C. R. Thompson, B. Munt, A. Sinhal, and J. G. Webb, "Role of echocardiography in percutaneous aortic valve implantation," *JACC: Cardiovascular Imaging*, vol. 1, no. 1, pp. 15–24, 2008.

[59] I. J. Ingimarsdóttir, L. H. Johansson, and F. A. Flachskampf, "Preoperative aortic annulus size assessment by transthoracic echocardiography compared to the size of surgically implanted aortic prostheses," *Echo research and practice*, vol. 6, no. 2, pp. 37–41, 2019.

[60] M. C. Svendsen, A. K. Sinha, Z. C. Berwick, W. Combs, S. D. Teague, T. Lefevre, V. Babaliaros, and G. Kassab, "Two-in-one aortic valve sizing and valvuloplasty conductance balloon catheter," *Catheterization and Cardiovascular Interventions*, vol. 86, no. 1, pp. 136–143, 2015.

[61] N. Quader, *Echocardiographic aortic annulus sizing for tavr*, 2017. [Online]. Available: https://citoday.com/articles/2017-mar-apr/echocardiographic-aortic-annulus-sizing-for-tavr?c4src=issue%5C%3Afeed.

[62] M. Marwan and S. Achenbach, "Role of cardiac ct before transcatheter aortic valve implantation (tavi)," *Current cardiology reports*, vol. 18, no. 2, p. 21, 2016.

[63] H. Knipe and M. M. Nadrljanski, *Computed tomography: Radiology reference article*. [Online]. Available: https://radiopaedia.org/articles/computed-tomography.

[64] S. Achenbach, V. Delgado, J. Hausleiter, P. Schoenhagen, J. K. Min, and J. A. Leipsic, "Scct expert consensus document on computed tomography imaging before transcatheter aortic valve implantation (tavi)/transcatheter aortic valve replacement (tavr)," *Journal of cardiovascular computed tomography*, vol. 6, no. 6, pp. 366–380, 2012.

[65] T. Jurencak, J. Turek, B. L. Kietselaer, C. Mihl, M. Kok, V. G. van Ommen, L. A. van Garsse, E. C. Nijssen, J. E. Wildberger, and M. Das, "Mdct evaluation of aortic root and aortic valve prior to tavi. what is the optimal imaging time point in the cardiac cycle?" *European radiology*, vol. 25, no. 7, pp. 1975–1983, 2015.

[66] A. Hamdan, V. Guetta, E. Konen, O. Goitein, A. Segev, E. Raanani, D. Spiegelstein, I. Hay, E. Di Segni, M. Eldar, *et al.*, "Deformation dynamics and mechanical properties of the aortic annulus by 4-dimensional computed tomography: Insights into the functional anatomy of the aortic valve complex and implications for transcatheter aortic valve therapy," *Journal of the American College of Cardiology*, vol. 59, no. 2, pp. 119–127, 2012.

[67] R. Gurvitch, J. G. Webb, R. Yuan, M. Johnson, C. Hague, A. B. Willson, S. Toggweiler, D. A. Wood, J. Ye, R. Moss, *et al.*, "Aortic annulus diameter determination by multidetector computed tomography: Reproducibility, applicability, and implications for transcatheter aortic valve implantation," *JACC: Cardiovascular Interventions*, vol. 4, no. 11, pp. 1235–1245, 2011.

[68] J. Kempfert, A. Van Linden, L. Lehmkuhl, A. J. Rastan, D. Holzhey, J. Blumenstein, F. W. Mohr, and T. Walther, "Aortic annulus sizing: Echocardiographic versus computed tomography derived measurements in comparison with direct surgical sizing," *European Journal of Cardio-Thoracic Surgery*, vol. 42, no. 4, pp. 627–633, 2012.

[69] H. Jilaihawi, M. Kashif, G. Fontana, A. Furugen, T. Shiota, G. Friede, R. Makhija, N. Doctor, M. B. Leon, and R. R. Makkar, "Cross-sectional computed tomographic assessment improves accuracy of aortic annular sizing for transcatheter aortic valve replacement and reduces the incidence of paravalvular aortic regurgitation," *Journal of the American College of Cardiology*, vol. 59, no. 14, pp. 1275–1286, 2012.

[70] R. K. Binder, J. G. Webb, A. B. Willson, M. Urena, N. C. Hansson, B. L. Norgaard, P. Pibarot, M. Barbanti, E. Larose, M. Freeman, *et al.*, "The impact of integration of a multidetector computed tomography annulus area sizing algorithm on outcomes of transcatheter aortic valve replacement: A prospective, multicenter, controlled trial," *Journal of the American College of Cardiology*, vol. 62, no. 5, pp. 431–438, 2013.

[71] A. Vegas, "Three-dimensional transesophageal echocardiography: Principles and clinical applications," *Annals of Cardiac Anaesthesia*, vol. 19, no. Suppl 1, S35, 2016.

[72] A. Papachristidis, M. Papitsas, D. Roper, Y. Wang, R. Dworakowski, J. Byrne, O. Wendler, P. MacCarthy, and M. J. Monaghan, "Three-dimensional measurement of aortic annulus dimensions using area or circumference for transcatheter aortic valve replacement valve sizing: Does it make a difference?" *Journal of the American Society of Echocardiography*, vol. 30, no. 9, pp. 871–878, 2017.

[73] T. Podlesnikar, E. A. Prihadi, P. J. van Rosendael, E. M. Vollema, F. van der Kley, A. de Weger, N. A. Marsan, F. Naji, Z. Fras, J. J. Bax, *et al.*, "Influence of the quantity of aortic valve calcium on the agreement between automated 3-dimensional transesophageal echocardiography and multidetector row computed tomography for aortic annulus sizing," *The American journal of cardiology*, vol. 121, no. 1, pp. 86–93, 2018.

[74] B. Vaquerizo, M. Spaziano, J. Alali, D. Mylote, P. Theriault-Lauzier, R. Alfagih, G. Martucci, J. Buithieu, and N. Piazza, "Three-dimensional echocardiography vs. computed tomography for transcatheter aortic valve replacement sizing," *European Heart Journal-Cardiovascular Imaging*, vol. 17, no. 1, pp. 15–23, 2016.

[75] H. Jilaihawi, N. Doctor, M. Kashif, T. Chakravarty, A. Rafique, M. Makar, A. Furugen, M. Nakamura, J. Mirocha, M. Gheorghiu, *et al.*, "Aortic annular sizing for transcatheter aortic valve replacement using cross-sectional 3-dimensional transesophageal echocardiography," *Journal of the American College of Cardiology*, vol. 61, no. 9, pp. 908–916, 2013.

[76] O. Husser, A. Holzamer, M. Resch, D. H. Endemann, J. Nunez, V. Bodi, C. Schmid, G. A. Riegger, H. Gössmann, O. Hamer, *et al.*, "Prosthesis sizing for transcatheter aortic valve implantation—comparison of three dimensional transesophageal echocardiography with multislice computed tomography," *International journal of cardiology*, vol. 168, no. 4, pp. 3431–3438, 2013.

[77] W. Tsang, M. G. Bateman, L. Weinert, G. Pellegrini, V. Mor-Avi, L. Sugeng, H. Yeung, A. R. Patel, A. J. Hill, P. A. Iaizzo, *et al.*, "Accuracy of aortic annular measurements obtained from three-dimensional echocardiography, ct and mri: Human in vitro and in vivo studies," *Heart*, vol. 98, no. 15, pp. 1146–1152, 2012.

[78] C. Mahon and R. Mohiaddin, "The emerging applications of cardiovascular magnetic resonance imaging in transcatheter aortic valve implantation," *Clinical Radiology*, 2019.

[79] W.-Y. I. Tseng, M.-Y. M. Su, and Y.-H. E. Tseng, "Introduction to cardiovascular magnetic resonance: Technical principles and clinical applications," *Acta Cardiologica Sinica*, vol. 32, no. 2, p. 129, 2016.

[80] R. Faletti, M. Gatti, S. Salizzoni, L. Bergamasco, R. Bonamini, D. Garabello, W. G. Marra, M. La Torre, M. Morello, S. Veglia, *et al.*, "Cardiovascular magnetic resonance as a reliable alternative to cardiovascular computed tomography and transesophageal echocardiography for aortic annulus valve sizing," *The international journal of cardiovascular imaging*, vol. 32, no. 8, pp. 1255–1263, 2016.

[81] R. Koos, E. Altiok, A. H. Mahnken, M. Neizel, G. Dohmen, N. Marx, H. Kühl, and R. Hoffmann, "Evaluation of aortic root for definition of prosthesis size by magnetic resonance imaging and cardiac computed tomography: Implications for transcatheter aortic valve implantation," *International journal of cardiology*, vol. 158, no. 3, pp. 353–358, 2012.

[82] P. Bernhardt, C. Rodewald, J. Seeger, B. Gonska, D. Buckert, M. Radermacher, V. Hombach, W. Rottbauer, and J. Wöhrle, "Non-contrast-enhanced magnetic resonance angiography is equal to contrast-enhanced multislice computed tomography for correct aortic sizing before transcatheter aortic valve implantation," *Clinical Research in Cardiology*, vol. 105, no. 3, pp. 273–278, 2016.

[83] J. Lou, N. A. Obuchowski, A. Krishnaswamy, Z. Popovic, S. D. Flamm, S. R. Kapadia, L. G. Svensson, M. A. Bolen, M. Y. Desai, S. S. Halliburton, *et al.*, "Manual, semiautomated, and fully automated measurement of the aortic annulus for planning of transcatheter aortic valve replacement (tavr/tavi): Analysis of interchangeability," *Journal of cardiovascular computed tomography*, vol. 9, no. 1, pp. 42–49, 2015.

[84] S. Queirós, C. Dubois, P. Morais, T. Adriaenssens, J. C. Fonseca, J. L. Vilaça, and J. D'hooge, "Automatic 3d aortic annulus sizing by computed tomography in the planning of transcatheter aortic valve implantation," *Journal of cardiovascular computed tomography*, vol. 11, no. 1, pp. 25–32, 2017.

[85] A. G. Cerillo, M. Mariani, M. Glauber, and S. Berti, "Sizing the annulus for transcatheter aortic valve implantation: More than a simple measure?" *European Journal of Cardio-Thoracic Surgery*, vol. 41, no. 3, pp. 717–718, 2012.

[86] V. C. Babaliaros, D. Liff, E. P. Chen, J. H. Rogers, R. A. Brown, V. H. Thourani, R. A. Guyton, S. Lerakis, A. E. Stillman, P. Raggi, *et al.*, "Can balloon aortic valvuloplasty help determine appropriate transcatheter aortic valve size?" *JACC: Cardiovascular Interventions*, vol. 1, no. 5, pp. 580–586, 2008.

[87] C. J. O'Sullivan and P. Wenaweser, "A glimpse into the future: In 2020, which patients will undergo tavi or savr?" *Interventional Cardiology Review*, vol. 12, no. 1, p. 44, 2017.

[88] L. Barilli, "Towards automated balloon valvuloplasty: Estimation of the aortic valve dimensions," M.S. thesis, 2018.

[89] M. A. Saab, "Applications of high-pressure balloons in the medical device industry," *Medical Device & Diagnostic Industry Magazine, NH, USA*, 1999.

[90] M. De Beule, P. Mortier, S. G. Carlier, B. Verhegghe, R. Van Impe, and P. Verdonck, "Realistic finite element-based stent design: The impact of balloon folding," *Journal of Biomechanics*, vol. 41, no. 2, pp. 383–389, 2008.

[91] C. J. Schultz, A. Weustink, N. Piazza, A. Otten, N. Mollet, G. Krestin, R. J. van Geuns, P. de Feyter, P. W. Serruys, and P. de Jaegere, "Geometry and degree of apposition of the corevalve revalving system with multislice computed tomography after implantation in patients with aortic stenosis," *Journal of the American College of Cardiology*, vol. 54, no. 10, pp. 911–918, 2009.

[92] P. Blanke, M. Siepe, J. Reinöhl, M. Zehender, F. Beyersdorf, C. Schlensak, M. Langer, and G. Pache, "Assessment of aortic annulus dimensions for edwards sapien transapical heart valve implantation by computed tomography: Calculating average diameter using a virtual ring method," *European Journal of Cardio-Thoracic Surgery*, vol. 38, no. 6, pp. 750–758, 2010.

[93] L. P. Broadbent, C. J. Moran, D. T. Cross, and C. P. Derdeyn, "Management of ruptures complicating angioplasty and stenting of supraaortic arteries: Report of two cases and a review of the literature," *American journal of neuroradiology*, vol. 24, no. 10, pp. 2057–2061, 2003.

[94] A. Mehta, A. Mehta, D. Velazquez-Pimentel, S. Sadek, and K. Althoefer, "Development of an adaptable, soft robot with an aortic diameter sensor to modulate blood flow in an extreme biological environment," in *2018 IEEE International Conference on Soft Robotics (RoboSoft)*, IEEE, 2018, pp. 344–349.

[95] J. E. Shigley, R. G. Budynas, and C. R. Mischke, *Mechanical engineering design*. McGraw-hill, 2004.

[96] Thomson, *Application sizing tool for pc series actuators*, Last Access: 2020-12-08. [Online]. Available: https://www.thomsonlinear.com/en/products/precision-linear-actuators/pc-series-sizing.

Appendix A

Sizing the Linear Actuators of the Robotic Inflation Devices

A.1 The First Robotic Inflation Device

Only the axial load associated with the maximum intra-balloon pressure acting on the plunger is taken into account to size the linear actuator. Under the assumption of very low inflation speed, viscous and inertial forces are neglected. Since the inner diameter of the syringe $D_i = 15.8$ mm and the maximum operating gauge pressure of the balloon $P_{max} = 4$ atm are known, the axial load F_L can be immediately calculated:

$$F_L = P_{max}\,\pi\,\frac{D_i^2}{4} = 79.48\,N$$

Based on the definition of mechanical advantage MA, the effort force F_E can be calculated from the load force F_L:

$$F_E = \frac{F_L}{MA}$$

The velocity ratio VR and the efficiency of the machine η must be determined to obtain MA. The former can be calculated from the outer diameter $D_o = 8$ mm and the lead $L = 8$ mm of the lead screw. The latter can be calculated from the thread angle of the lead screw α and the equivalent angle of friction β. Since the lead screw is made of steel and it is not lubricated, a friction coefficient of 0.3 is hypothesised [95]:

$$VR = \frac{\pi\,D_o}{L} = 3.14$$

$$\alpha = \arctan\left(\frac{L}{\pi D_o}\right) = 17.66\,^{\circ}\,;\ \beta = \arctan(0.3) = 16.70\,^{\circ}$$

$$\eta = \frac{\tan(\alpha)}{\tan(\alpha+\beta)} = 46.56\,\%$$

$$MA = \frac{VR}{\eta} = 1.46$$

At this stage it is possible to determine F_E and subsequently the torque T_E that the motor needs to apply:

$$F_E = \frac{F_L}{MA} = 54.33\ N$$

$$T_E = F_E\,\frac{D_o}{2} = 217.32\ Nmm$$

Due to the low inflation speed assumption, the maximum torque that can be considered applicable by the motor is

$$T_{max} = T_H - 2T_D = 236\ Nmm$$

where T_H is the holding torque and T_D is the detent torque of the stepper motor. Although the safety factor is extremely close to one, since $T_{max} > T_E$ the linear actuator can be regarded as potentially suitable for the application.

A.2 The Second Robotic Inflation Device

The linear actuator was identified through the sizing tool available on the Thomson website [96]. A spring compression axial load type was chosen for the analysis. According to Bernoulli's equation for real fluids, the maximum value of the load was calculated based on two contributions. The first contribution F_L is the axial load associated with the static maximum intra-balloon pressure acting on the plunger. Since the inner diameter of the syringe $D_i = 32.57$ mm and the maximum operating gauge pressure of the balloon $P_{max} = 4$ atm are known, the first contribution F_L can be immediately calculated:

$$F_L = P_{max}\,\pi\,\frac{D_i^2}{4} = 337.7\ N$$

The other contribution comes from head losses, which can be divided in major and minor losses. Assuming that they are uniquely caused by the catheter shaft, such pressure drops can only be estimated if the average velocity of the fluid inside the pipe is known. Therefore the kinematics of the system must be examined.

Since the inner diameter of the syringe is $D_i = 32.57$ mm, a displacement of the plunger of 25.2 mm is necessary to inject the 21 ml of fluid required to fully inflate the balloon catheter (see Section 3.2). Hence to travel such distance in 3 s (see Section 1.1.3), the plunger needs to move at an average speed of 8.4 mm/s. If a 1/3, 1/3, 1/3 trapezoidal velocity profile is assumed, the plunger needs to first keep a uniform acceleration of 12.6 mm/s^2 for 1 s, then move at a constant speed of 12.6 mm/s for 1 s and finally keep a uniform deceleration of -12.6 mm/s^2 for 1 s to accomplish the task. The maximum speed of the plunger $V_p = 12.6$ mm/s is considered to estimate the losses. The associated volumetric flow rate can be calculated as:

$$Q = \pi \frac{D_i^2}{4} V_p = 1.05 \cdot 10^{-5} \frac{m^3}{s}$$

Considering an inner catheter shaft diameter of $D_s = 3$ mm, the law of conservation of mass can be used to calculate the average velocity V_s of the fluid inside the catheter shaft:

$$V_s = \frac{Q}{\pi \frac{D_s^2}{4}} = 1.5 \frac{m}{s}$$

The general expression for minor losses is:

$$P = \xi \rho \frac{V^2}{2}$$

where ξ is a resistance coefficient that depends on the type of local loss, ρ is the density of the fluid and V is the average velocity of the fluid. The only two minor losses taken into account in this case are the entrance and the exit of the pipe, for which the two coefficients $\xi_{in} = 0.9$ and $\xi_{out} = 0.2$ are used respectively. Hence the total pressure drop associated with local losses is:

$$P_{min} = (\xi_{in} + \xi_{out}) \rho \frac{V_s^2}{2} = 1209\ Pa$$

where $\rho = 997$ kg/m^3 is the density of water at 25 °C. Before estimating the major losses, it must be determined whether the flow inside the catheter shaft is laminar, turbulent or transitional. That can be done by calculating the Reynolds number:

$$Re = \frac{\rho V_s D_s}{\mu} = 4991$$

where $\mu = 8.9 \cdot 10^{-4}\ Pa\ s$ is the dynamic viscosity of water at 25 °C. Because $Re > 4000$ the flow inside the catheter is turbulent. Under these circumstances the Darcy–Weisbach

equation must be used to compute major head losses:

$$P_{maj} = \frac{f_D \rho V_s^2 L_s}{2D_s} = 18105\ Pa$$

where $L_s = 1.3$ m is the length of the catheter shaft and $f_D = 0.038$ is the Darcy friction factor extracted from the Moody diagram. Since the shaft is made of plastic, a pipe roughness $\varepsilon = 0.0025$ mm was considered.
The total axial load F_T can finally be determined:

$$F_T = (P_{max} + P_{min} + P_{maj})\pi \frac{D_i^2}{4} = 353.8\ N$$

Although the maximum intra-balloon pressure and the maximum flow velocity in the shaft are technically present at different times during the motion, the impact of both was taken into account for the sake of caution.
Based on F_T and V_p, the Thomson sizing tool outputs various options for linear actuators, with associated drive torque and rotational speed. Since the speed required in this application is relatively low, the linear actuator with the minimum drive torque was chosen. To achieve the desired motion this linear actuator requires a maximum drive torque of 0.26 Nm and a maximum drive rotational speed of 252 RPM. With a rated torque of 0.74 Nm and a rated speed of 7000 RPM, the selected servomotor can easily meet the minimum requirements, leaving plenty of room for significantly higher speeds.

Appendix B

Code Snippets

B.1 The First Robotic Inflation Device

The first portion of the Processing sketch deals with the basic initialisation of the program. The relevant libraries are imported while all the variables are declared and initialised. Various objects required for communicating with the Arduino controller, acquiring data and handling the graphics are also created.

```
//----LIBRARIES----//
import g4p_controls.*;
import grafica.*;
import controlP5.*;
import org.firmata.*;
import processing.serial.*;
import cc.arduino.*;
//---- SERIAL COMMUNICATION ----//
Arduino arduino;
ControlP5 cp5;
//----INITIALISATION----//
float current_pressure_VOLT;
float current_pressure_ATM;
float pressure_min = 0;
float pressure_max = 0;
int vol;
float flow_rate = 0;
float balloon_volume_realtime;
```

```
//MOTOR SPECIFICATIONS
float rev_time = 0.6;
float voltaggio = 10;
float max_current = 0.4;
float inductance = 0.045;
//ASSIGNING PIN NUMBERS
int pwr_a = 3;
int pwr_b = 9;
int dir_a = 2;
int dir_b = 8;
int pressure_pin = 0;
//MOTOR CONTROL
boolean flag_forward_pin = 0;
int numerosteps_fw = 0;
int count_fw = 0;
boolean flag_backward_pin = 0;
int numerosteps_bw = 0;
int count_bw = 0;
int Delay;
//TO SAVE DATA IN TXT FILE
PrintWriter output;
//ACTIVATED WHEN PROCESS STARTS
boolean flag_start = 0;
//GRAPHICS
PFont f;
PFont F;
PFont l;
GPlot grafico_PV;
GPoint punto1;
String volume, speed;
Textfield VOLUME;
int SPEED = 100;
```

The setup() function is then called to generate the GUI and establish communication with the controller. Once connected, the program sends the commands to configure the pins of the Arduino. The createGUI() function contains auto-generated code that is used to manage the functionalities and the appearance of the GUI controls.

```
void setup(){

  createGUI();
  f = createFont("Arial",10,true); //axis ticks font
  F = createFont("Arial",36,true); //title font
  l = createFont("Arial",16,true); //labels and values font
  println(width,height);
  size(1000, 900);
  arduino = new Arduino(this, Arduino.list()[0], 57600);
  background(0);
  arduino.pinMode(pwr_a, Arduino.OUTPUT);
  arduino.pinMode(pwr_b, Arduino.OUTPUT);
  arduino.pinMode(dir_a, Arduino.OUTPUT);
  arduino.pinMode(dir_b, Arduino.OUTPUT);
  arduino.pinMode(pressure_pin, Arduino.INPUT);

  grafico_PV =new GPlot(this,width*0.35,height*0.25,width*0.6,height*0.4);
  grafico_PV.setAllFontProperties("Georgia", 255, 14);
  grafico_PV.getXAxis().setAxisLabelText("Volume [mL]");
  grafico_PV.getYAxis().setAxisLabelText("Pressure [atm]");
  grafico_PV.setBgColor(0);
  grafico_PV.setTitleText("BALLOON PRESSURE VS VOLUME");
  grafico_PV.drawTitle();
  grafico_PV.setYLim(0,6);
  grafico_PV.setXLim(0,30);

  cp5 = new ControlP5(this);
  VOLUME = cp5.addTextfield("VOLUME").setPosition(30, 180).setSize(200,
     40).setAutoClear(false);
  cp5.addSlider("SPEED").setPosition(30, 240).setSize(200,
     40).setRange(100,10);
  cp5.addBang("Submit").setPosition(30, 300).setSize(80, 40);
  fill(0);
  stroke(255,0,0);
  strokeWeight(6);
  rect(20,130,300,250);
  textFont(l);
  textAlign(LEFT);
```

```
   fill(255);
   text("Type Volume and choose Speed,",30,150);
   text ("then press SUBMIT",30,170);

   fill(0);
   stroke(255,0,0);
   strokeWeight(6);
   rect(20,400,300,230);
   textFont(l);
   textAlign(LEFT);
   fill(255);
   text("Once you finish, press STOP to save",30,600);
   text("data in the .txt file",30,620);

}
```

Right after the setup() function, the draw() function, which represents the functional core of the program, is called. While the code described so far is only executed once at program startup, the draw() function runs continuously. When the start button in the GUI is pressed, the automated motor control and data acquisition routine described in Algorithm 1 is executed. At this point, the program branches out into two cycles. Either one or the other is executed, depending on the selected movement direction of the plunger.

```
void draw(){
    Delay = SPEED;
    float Delay_float = Delay*0.001;
    float v_max =
        voltaggio/((2*inductance*max_current*200)+((Delay_float)*200*voltaggio));
    flow_rate = (200*v_max)/127.5;
    grafico_PV.defaultDraw();
    if (flag_start == 1){
      float count_fw = (vol*127.5);
      float count_bw = (vol*127.5);
//Injection Sequence
      if (flag_forward_pin == 1){
        if (numerosteps_fw<=count_fw){
          phase_1();
          Plot_fw();
```

```
      }
      if (numerosteps_fw<=count_fw){
        phase_2();
        Plot_fw();
      }
      if (numerosteps_fw<=count_fw){
        phase_3();
        Plot_fw();
      }
      if (numerosteps_fw<=count_fw){
        phase_4();
        Plot_fw();
      }
      if (numerosteps_fw>count_fw){
      flag_start=0;
      }
    }
//Extraction Sequence
    if (flag_backward_pin == 1){
      if (numerosteps_bw<=count_bw){
         phase_3();
         Plot_bw();
      }
      if (numerosteps_bw<=count_bw){
         phase_2();
         Plot_bw();
      }
      if (numerosteps_bw<=count_bw){
         phase_1();
         Plot_bw();
      }
      if (numerosteps_bw<=count_bw){
         phase_4();
         Plot_bw();
      }
      if (numerosteps_fw>count_fw){
      flag_start=0;
      }
    }
```

```
    }

     if (flag_start==0){
     aggiorna_caselle_testo();
     }
}
```

In both cycles the movement of the motor is regulated using the same four functions phase_1(), phase_2(), phase_3() and phase_4(). The only difference is the order in which they are executed. Every time there is a transition between two phases the motor takes one step. The rotational speed of the motor can be adjusted by modifying the Delay variable that is passed as an argument to the delay() function.

```
void phase_1(){
       arduino.digitalWrite(pwr_a,Arduino.HIGH);
       arduino.digitalWrite(pwr_b,Arduino.HIGH);
       arduino.digitalWrite(dir_a,Arduino.HIGH);
       arduino.digitalWrite(dir_b,Arduino.HIGH);
       delay(Delay);
}

void phase_2(){
       arduino.digitalWrite(pwr_a,Arduino.HIGH);
       arduino.digitalWrite(pwr_b,Arduino.HIGH);
       arduino.digitalWrite(dir_a,Arduino.HIGH);
       arduino.digitalWrite(dir_b,Arduino.LOW);
       delay(Delay);
}

void phase_3(){
       arduino.digitalWrite(pwr_a,Arduino.HIGH);
       arduino.digitalWrite(pwr_b,Arduino.HIGH);
       arduino.digitalWrite(dir_a,Arduino.LOW);
       arduino.digitalWrite(dir_b,Arduino.LOW);
       delay(Delay);
}

void phase_4(){
```

```
        arduino.digitalWrite(pwr_a,Arduino.HIGH);
        arduino.digitalWrite(pwr_b,Arduino.HIGH);
        arduino.digitalWrite(dir_a,Arduino.LOW);
        arduino.digitalWrite(dir_b,Arduino.HIGH);
        delay(Delay);
}
```

The two functions Plot_fw() and Plot_bw() are responsible for counting the steps taken by the motor and acquiring pressure data. They also progressively write pressure-volume data to a text file and plot it on the GUI. The only difference between the two is the step counting variable. The aggiorna_caselle_testo() function is called to refresh the values and the graph displayed on the GUI.

```
void Plot_fw(){
        current_pressure_VOLT = map(arduino.analogRead(0),0,1023,0,5.0);
        current_pressure_ATM =
            map(current_pressure_VOLT,0.012,6.81,0,7*0.986923);
        println(current_pressure_VOLT);
                strokeWeight(4);stroke(0,255,0);

        balloon_volume_realtime = (numerosteps_fw*0.04)/5.1;
        GPoint punto1 = new
            GPoint(balloon_volume_realtime,current_pressure_ATM);
        grafico_PV.addPoint(punto1);
        aggiorna_caselle_testo();
        output.print(current_pressure_ATM);
        output.print("       ");
        output.println(balloon_volume_realtime+10);
        grafico_PV.defaultDraw();

        if (current_pressure_ATM > 4.5){
            flag_start = 0;
        }
        numerosteps_fw++; //numerosteps_bw++ in Plot_bw()
    }

void aggiorna_caselle_testo(){
        textFont(l);
```

```
        textAlign(LEFT);
        fill(255);
        text("CURRENT PRESSURE", 460,height-750);
        text("[atm]", 525, height-730);
        stroke(255,255,255);
        rect(470, height-720,150,20);

        textFont(l);
        textAlign(LEFT);
        fill(255);
        text("CURRENT FLOW RATE", 60,height-200);
        text("[mL/s]",120,height-180);
        rect(75, height-170,150,20);

        textFont(l);
        textAlign(LEFT);
        fill(255);
        text("CURRENT VOLUME", 700,height-750);
        text("[mL]",765,height-730);
        rect(700, height-720,150,20);
        textAlign(RIGHT);
        fill(0);

        fill(0);
        text(current_pressure_ATM,555, height-705);
        text(flow_rate,160,height-155);
        text(balloon_volume_realtime,785,height-705);
        fill(0);
}
```

The automated routine stops when either the acquired pressure is greater than 4.5 atm or the number of counted steps is equal to the number of steps initially calculated, based on the volume input by the user.

B.2 The Second Robotic Inflation Device

The AKD BASIC code begins with the initialisation of a large number of device parameters, which can be also configured from the Workbench Interface tab. Since the default values were used, that portion of code is not discussed in here. Right after the initialisation of the device parameters, the constants and the global variables are declared.

```
const PI = 3.1415926535
const PLUNG_AREA = PI*(32.57/2)^2 'Plunger area in mm2'
Dim option as integer
Dim volume, lowerVolume, speed as float
```

The main program essentially consists of an infinite while loop containing two main parts. The code in the first one represents the main menu of the console application. The user is asked to input a value corresponding to one of the implemented operational modalities of the platform. The second part is a switch-case statement. Each case of the statement contains the code associated with a specific operational modality. The console application can be exited from the main menu by inputting a value that is not assigned to a modality.

```
Main
   While 1
      Main_Menu:
      DOUT1.STATEU = 0
      Cls

      Print "Please input 1 or 2 to choose one of the following options or
          any other character to exit:"
      Input "1) Perform Experiment 2) Move to home position 3) Filling
          Routine"; option
      Print "You selected "; option
      Pause(0.5)

      Select Case option
         Case 1 //Experiment routine
            Start_Experiment:
            Cls
            Input "Input the amount of fluid to be injected in millilitres";
                volume
```

```
    Print "You selected "; volume; " ml"

    If volume > 40 Then
       Print "The amount of volume you selected exceeds the limits of
           the system, please input a lower value"
       Pause(1)
       GoTo Start_Experiment
    End If
    Input "Input the injection speed in millilitres per second"; speed
    Print "You selected "; speed; " ml/s"
    REC.TRIG
    MOVE.TARGETPOS = mlToPosition(volume) //The position in
        micrometers
    MOVE.RUNSPEED = linearSpeedToRPM(speed) //The velocity in rpm
    MOVE.GOABS
    Print "Moving..."
    While MOVE.MOVING
       Print "Pressure "; voltsToPressure(AIN.VALUE); " atm"
       If voltsToPressure(AIN.VALUE) > 6.5 Then
          MOVE.ABORT
          DOUT1.STATEU = 1 //The digital output pin is activated when
              the motion is aborted, to easily identify that point
              within the exported data'
          Print "Inner absolute pressure exceeded safety limits (4.5
              atm)"
          Print "Aborting programmed motion and going back to the main
              menu..."
          Pause(1)
          GoTo Main_Menu
       End If
    Wend
    Print "Motion Complete"
    DOUT1.STATEU = 1 //The digital output pin is activated when the
        motion is completed, to easily identify that point within the
        exported data'
    Pause(1)

Case 2 //homing routine
Cls
```

```
    MOVE.RUNSPEED = linearSpeedToRPM(3)
    MOVE.GOHOME
    Print "Moving home..."
    While MOVE.MOVING

    Wend
    Print "Motion Complete"

    Pause(1)

Case 3
Filling_Routine:
    Cls
    Input "Input the upper limit of the volume of fluid in
        millilitres"; volume
    Print "You selected "; volume; " ml"
    Input "Input the lower limit of the volume of fluid in
        millilitres"; lowerVolume
    Print "You selected "; lowerVolume; " ml"
    If volume > 40 or lowerVolume > 40 Then
        Print "The amount of volume you selected exceeds the limits of
            the system, please input a lower value"
        Pause(1)
        GoTo Filling_Routine
    End If
    Input "Input the injection speed in millilitres per second"; speed
    Print "You selected "; speed; " ml/s"
    MOVE.RUNSPEED = linearSpeedToRPM(speed) //The velocity in rpm
    While 1
        MOVE.TARGETPOS = mlToPosition(volume) //The position in
            micrometers
        MOVE.GOABS
        While MOVE.MOVING
            Print "Pressure "; voltsToPressure(AIN.VALUE); " atm"
            If voltsToPressure(AIN.VALUE) > 6.5 Then
                MOVE.ABORT
                DOUT1.STATEU = 1 //The digital output pin is activated
                    when the motion is aborted, to easily identify that
                    point within the exported data'
```

```
                    Print "Inner absolute pressure exceeded safety limits
                        (4.5 atm)"
                    Print "Aborting programmed motion and going back to the
                        main menu..."
                    Pause(1)
                    GoTo Main_Menu
                End If
            Wend
            MOVE.TARGETPOS = mlToPosition(lowerVolume) //The position in
                micrometers
            MOVE.GOABS
            While MOVE.MOVING
                Print "Pressure "; voltsToPressure(AIN.VALUE); " atm"
            Wend
        Wend
    Case Else
        Exit While
  End Select
 Wend
 Cls
End Main
```

The last portion of the code includes the declaration of the functions that are called in the program to perform various conversions.

```
Function mlToPosition(ml as float) as integer
 //This function takes in the volume of fluid to be injected (in ml) and
    outputs the corresponding absolute position (in micron)
 mlToPosition = ((ml*1000)/PLUNG_AREA)*1000
End Function

Function linearSpeedToRPM(mls as float) as float
 //This function takes in the flow rate to be injected (in ml/s) and
    outputs the corresponding rotational speed (in RPM)
 linearSpeedToRPM = (((mls*1000)/PLUNG_AREA)*20)
End Function

Function voltsToPressure(volts as float) as float
```

```
   //This function takes in the voltage measured on the analog pin (in
      Volts) and outputs the corresponding pressure value (in atm)
   voltsToPressure = volts*((7*0.986923)/10)
End Function
```

B.3 The Sizing Algorithm

The sizing algorithm was implemented as two different functions in Matlab, one for the analytical model of the balloon free inflation and one for the numerical one. The code associated with the analytical model is included below.

```
function [ diameter ] = diameterFromPVCurveAnalytical( expPVCurve )
% The argument is a matrix in which every P-V curve is represented by two
    consecutive column vectors, the first one is V in ml and the second one
    is P in atm.
% The output is the calculated annular diameter in mm.

%The parameters of the analytical model are declared
D = 20.75; %mm
E = 556; %MPa
L = 35.82; %mm
c = 1661; %mm3
ts = 0.05; %mm
%c = -3802; %second robotic inflation device
%ts = 0.04831; %second robotic inflation device
v = 0.45;

tc=(((2-v)*0.4053*D^2)/((23-D)*4*E)); % constraint: diameter 23 mm at 4 atm

%The initial volumes of the model are declared
Vc = (pi*L*D^2)/4;
Vs = (pi*D^3)/6;

%Symbolic variables and p-v model function are declared
syms p vol
%p is multiplied by 0.101325 to convert atm into MPa. 0.101325 is subtracted
    to p to compensate for the absence of outer atmospheric pressure
```

```
cylinderVolume = Vc + Vc*(((p*0.101325-0.101325)*D)/(4*tc*E))*(5-4*v);
sphereVolume = Vs+Vs*((3*(p*0.101325-0.101325)*D)/(4*ts*E))*(1-v);
%The volume is multiplied by 0.001 to convert mm3 into mL
eq1 = vol == (cylinderVolume+sphereVolume+c)*0.001;

vPInverse = finverse((cylinderVolume+sphereVolume+c)*0.001);
hold on; fplot(vPInverse,[18.5 21])
%hold on; fplot(vPInverse,[12 16]) %second robotic inflation device
yLine = fitLineInExperimentalPVCurve(expPVCurve, 0.03);
eq2 = p == yLine;
%The point at which the p-v curve deviates from the free inflation curve is
    identified
pvContactPoint = vpasolve([eq1,eq2]);

scatter(pvContactPoint.vol,pvContactPoint.p, 'filled','r');
%The annular diameter is calculated
diameter = D+D*(((pvContactPoint.p*0.101325-0.101325)*D)/(4*tc*E))*(2-v);

end
```

The function associated with the numerical model is provided in the following block of code.

```
function [ diameter ] = diameterFromPVCurveNumerical( expPVCurve )
% The argument is a matrix in which every P-V curve is represented by two
    consecutive column vectors, the first one is V in ml and the second one
    is P in atm.
% The output is the calculated annular diameter in mm.
atm_pressure = 1;

%The parameters of the analytical model are declared
a = -0.093;
b = 4.549;
d = -50.11;
c = -1.743;
%c = 3.746; %second robotic inflation device

%Symbolic variables and p-v model function are declared
```

```
syms p vol
eq1 = p == a*(vol+c)^2+b*(vol+c)+d+atm_pressure;

hold on;
fplot(a*(vol+c)^2+b*(vol+c)+d+atm_pressure,[18.5 21])
%fplot(a*(vol+c)^2+b*(vol+c)+d+atm_pressure,[13 17]) this is for the new
    platform
%fplot(vPInverse,[18 21.5])
yLine = fitLineInExperimentalPVCurve(expPVCurve, 0.03);
eq2 = p == yLine;
assume(p>=0); condition to remove negative results

%The point at which the p-v curve deviates from the free inflation curve is
    identified
pvContactPoint = vpasolve([eq1,eq2]);
scatter(pvContactPoint.vol,pvContactPoint.p, 'filled','r');
%The annular diameter is calculated
diameter = 0.0528*(pvContactPoint.p-atm_pressure)^2+0.474*(pvContactPoint.p-
atm_pressure)+20.75;

end
```

Both functions rely on the *fitLineInExperimentalPVCurve* function to get a linear analytical representation of the portion of curve that deviates from the free inflation curve.

```
function [ yLine] = fitLineInExperimentalPVCurve(pVcurves, desiredRMSE)
%The compulsory argument is a matrix in which every P-V curve is represented
    by two consecutive column vectors, the first one is V in ml and the
    second one is P in atm.
%The optional argument is the RMSE threshold in atm.
%It returns a symbolic expression y=ax+b of the fitted line.
if nargin == 1
    desiredRMSE = 0.02; %dfeault RMSE value
end
syms vol;
volume = pVcurves(:,1);
pressure = pVcurves(:,2);
xGraph = volume;
```

```
yGraph = pressure;
[c,S] = polyfit(volume, pressure,1);
[y,delta] = polyval(c,volume,S);
[r2,rmse] = rsquare(pressure,y);
if(rmse>desiredRMSE)
    while(rmse>desiredRMSE)
        volume(1)=[];
        pressure(1)=[];
        [c,S] = polyfit(volume, pressure,1);
        [y,delta] = polyval(c,volume,S);
        [r2,rmse] = rsquare(pressure,y);
    end
end
linearCoefficients(:,1) = c;
yLine = linearCoefficients(1,1)*vol + linearCoefficients(2,1);
plot(xGraph, yGraph,'--');
hold on
fplot(yLine, [18 21.5]);
%fplot(yLine, [12 15]) %second robotic inflation device
title('Pressure-Volume curves');
xlabel('Volume [mL]');
ylabel('Pressure [atm]');
end
```